New Methods for Measuring CSA Tensors: Applications to Nucleotides and Nucleosides

Yanqi Wu

Thesis submitted to the University of Nottingham

for the degree of Doctor of Philosophy

March 2010

Declaration

The work in this thesis is based on research carried out at the Solid-State NMR Group, School of Chemistry, University of Nottingham, England. No part of this thesis has been submitted elsewhere for any other degree or qualification and it is all my own work unless referenced to the contrary in the text.

Yanqi Wu

New Methods for Measuring CSA Tensors: Applications to Nucleotides and Nucleosides

Yanqi Wu

Submitted for the degree of Doctor of Philosophy

March 2010

Abstract

A novel version of the CSA (Chemical Shift Anisotropy) amplification experiment which results in large amplification factors is introduced. Large x_a (up to 48) are achieved by sequences which are efficient in terms of the number of π pulses and total duration compared to a modification due to Orr *et al.* (2005), and greater flexibility in terms of the choice of amplification factor is possible than in our most recent version. Furthermore, the incorporation of XiX decoupling ensures the overall sensitivity of the experiment is optimal. This advantage has been proved by extracting the CSA tensors for a novel vinylphosphonate-linked nucleotide.

The application of CSA amplification experiment to six nucleosides is also discussed. The measured principal tensor values are compared with those calculated using the recently developed first-principles methods. Throughout this work, the NMR parameters of all nucleosides are presented.

Finally, high-resolution multi-nuclear solid-state NMR experiments are used to study some novel vinyl phosphonate-linked oligo-nucleotides.

Acknowledgements

I would like to express my sincere gratitude to my supervisor Dr. Jeremy J. Titman for his considerable help and encouragement throughout the duration of this work. Thank you for giving me the opportunity to join your group and guiding me through the world of nuclear magnetic resonance. Thanks for the time spent on me during these last years, especially during the correction of my thesis.

Many thanks go to Dr. Limin Shao for extensive help with the CSA amplification experiment. Many thanks also go to Dr. Andrew Jurd who has given me a lot of help during my Ph.D study. Thanks go to all the members of Nottingham Solid-State NMR group: Dr. Andrew Powell, Dr. Xi Yu, Daniel Lee, David Bennett and Greg Martin.

Many thanks go to Dr. Charles Crockford and Dr. Limin Shao for their contribution to the field of CSA amplification experiments. Many thanks also go to Dr. Jonathan R. Yates and Mikhail Kibalchenko to calculate CSA tensors of nucleosides.

The work was sponsored by EPSRC. I also thank the Overseas Research Students Award Scheme (ORSAS) and The University of Nottingham for financial support.

Special thanks to all my family for their endless support and love.

Contents

Chapter 1 Introduction 1

1.1 Nuclear Magnetic Resonance. 1

1.2 Solid-State NMR. 3

1.3 Measuring the Chemical Shift Anisotropy. 4

1.4 CSA Amplification. 7

Chapter 2 Theory of CSA Amplification 10

2.1 Quantum Mechanical Description of NMR. 10

2.1.1 Quantum Mechanics of an Isolated Spin. 10

2.1.2 Statistical Description of an Ensemble of Spins. 12

2.1.3 The Nuclear Spin Hamiltonian. 15

2.1.4 The NMR Experiment. 16

2.2 Chemical Shift. 18

2.2.1 Chemical Shift Hamiltonian. 18

2.2.2 Principal Axis System. 19

2.2.3 Irreducible Spherical Tensors. 21

2.3 Magic Angle Spinning. 23

2.3.1 Spinning Sidebands. 23

2.3.2 Sideband Manipulation. 30

TOSS. 30

PASS. 31

CSA Amplification. 35

Chapter 3 CSA Amplification Methodology 39

3.1 Experiments. 39

3.1.1 Pulse Sequence. 39

Cross Polarization. 40

Decoupling. 40

3.1.2 Pulse Calibration. 42

3.1.3 Phase Cycling. 42

3.1.4 Typical Experimental Parameters. 45

3.1.5 Data Processing. 46

3.2 Simulations. 48

3.2.1 Spectral Simulations. 48

3.2.2 Powder Averaging. 48

3.2.3 Measurements of CSA Tensor Parameters. 49

Chapter 4 Developments of the CSA Amplification Experiment 51

4.1 Introduction. 51

4.2 Theory. 52

4.3 Experimental Set Up. 55

4.4 Results and Discussion. 56

Demonstration on Vinyl Phosphonate Nucleotide. 56

4.5 Conclusions. 71

Chapter 5 Application of CSA Amplification Experiment to Nucleosides 72

5.1 Introduction. 72

5.2 Experimental. 73

5.2.1 Materials. 73

5.2.2 X-Ray Diffraction (XRD) 74

5.2.3 NMR Experiments and Computation. 75

5.3 Results and Discussion. 78

5.3.1 CPMAS Spectra and Carbon-13 Isotropic Shifts. 78

5.3.2 CSA Tensors of Nucleosides. 83

5.3.3 Comparison with Calculated CSA Tensors 98

5.4 Conclusions. 109

Chapter 6 Solid-State NMR studies of vinyl phosphonate-linked nucleotides 110

6.1 Introduction. 110

6.2 Experimental. 111

6.3 High-Resolution Proton-Carbon Correlation Experiment using DUMBO-1. 112

6.4 Phosphorus-31 Solid-State NMR of Vinylphosphonate-linked Nucleootides 118

Chapter 7 Summary and Outlook 126

Appendix 128

A.I Analytical Timing Solutions for the CSA Amplification Experiments of Five π Pulses. 128

A.II The X-Ray Report of 5-methyluridine. 129

A.III Studies of Reliability of Chemical Shift Tensors Fitting. 133

References 135

List of Figures

2.1 Powder pattern lineshapes for a single molecular site with CSA 20

2.2 Carbon-13 CP spectra of glycine powder. 24

2.3 Pulse sequence for the two-dimensional PASS experiment due to Féaux de Lacroix *et al*. 32

2.4 Pulse sequence for the 2D-PASS experiment due to Antzutkin *et al*. 34

2.5 The original CSA amplification pulse sequence. 38

3.1 Processing procedure for the CSA amplification experiment. 47

4.1 Modified CSA amplification pulse sequence. 52

4.2 The structure of the vinyl phosphonate modified nucleotide. 57

4.3 Carbon–13 MAS spectrum of the vinyl phosphonate modified nucleotide . . .58

4.4 Regions of two-dimensional spectra of the vinyl phosphonate modified nucleotide 60

4.5 Part of the centerband of the original CSA amplification with XiX decoupling of sample vinyl phosphonate nucleotide 61

4.6 Part of CSA amplification spectra of the vinyl phosphonate modified nucleotide 62

4.7 Sideband intensities extracted from the original CSA amplification sequence compared with those obtained from the modified sequence 65

4.8 Comparison of the chemical shift anisotropy obtained from the modified CSA amplification spectra and the original CSA amplification spectra 66

4.9 χ^2 statistic as a function of the CSA parameters ζ and η of the vinyl phosphonate modified nucleotide 67-68

4.10 Values of shift anisotropy (ζ) and asymmetry (η) extracted from CSA amplification experiments 70

5.1 The structure of 2'-deoxythymidine, adenosine, uridine, cytidine, guanosine, and 5-methyluridine with atom numbering. 73

5.2 The chemical structure of a single molecule of 5-methyluridine.determined by X-ray. 74

5.3 Part of carbon-13 CPMAS spectra of (a) 2'-deoxythymidine, (b) adenosine, (c) cytidine and (d) uridine recorded using parameters described in the text. . . . 79

5.4 Part of carbon-13 CPMAS spectra of guanosion in (a) a nonstoichiometric state of hydration and (b) the dehydrated state. 80

5.5 Part of carbon-13 MAS spectra of 5-methyluridine (a) before crystallization, and (b) after crystallization. 82

5.6 Part of CSA amplification spectrum of 2'-deoxythymidine 83

5.7 χ^2 statistic as a function of the CSA parameters ζ and η of 2'-deoxythymidine. 85

5.8 χ^2 statistic as a function of the CSA parameters ζ and η of adenosine. 86

5.9 χ^2 statistic as a function of the CSA parameters ζ and η of cytidine. 87

5.10 χ^2 statistic as a function of the CSA parameters ζ and η of guanosine. 88

5.11A χ^2 statistic as a function of the CSA parameters ζ and η of uridine. 90

5.11B χ^2 statistic as a function of the CSA parameters ζ and η of uridine. 91

5.12 χ^2 statistic as a function of the CSA parameters ζ and η of 5-methyluridine. . 92

5.13 Plots of the shift anisotropy, ζ, against the isotropic shift (circles) measured using CSA amplification and (asterisks) calculated and scaled for (a) 2'-deoxythymidine,(b) adenosine and (c) cytidine. 105

5.14 Plots of the shift anisotropy, ζ, against the isotropic shift (circles) measured using CSA amplification and (asterisks) calculated and scaled for (a) guanosine; (b) uridine and (c) 5-methyluridine. 106

5.15 Plot showing the correlation between calculated and experimental isotropic carbon-13 chemical shifts and principal values of 2'-deoxythymidine, adenosine, cytidine, guanosine, uridine and 5-methyluridine 108

6.1 Structures of the vinylphosphonate-linked nucleotides. 111

6.2 One-dimensional proton spectra of sample **1**. 112

6.3 Pulse sequence and coherence transfer pathway for the MAS-*J*-HMQC experiment. 113

6.4 Carbon–proton two-dimensional MAS-*J*-HMQC spectrum of a natural abundance sample **1**. 114

6.5 Two-dimensional MAS-*J*-HMQC spectrum of a natural abundance sample **4**. 116

6.6 Phosphorus-31 MAS spectrum of sample **1**. 119

6.7 Phosphorus-31 MAS spectrum of sample **2**. 120

6.8 Phosphorus-31 MAS and ^{31}P CSA amplification spectra of sample **3** 121

6.9 Phosphorus-31 CPMAS NMR spectra of oliginucleotides attached to a CPG solid-phase support. 123

List of Tables

4.1 CSA amplification measurements of principal components of shift tensors in the vinyl phosphonate modified nucleotide. 69

5.1 Comparison of the principal components of carbon-13 chemical shift tensors of 2'-deoxythymidine measured using CSA amplification with those measured previously. 93

5.2 Comparison of the principal components of carbon-13 chemical shift tensors of adenosine measured using CSA amplification with those measured previously. 94

5.3 Comparison of the principal components of carbon-13 chemical shift tensors of cytidine measured using CSA amplification with those measured previously. 95

5.4 Comparison of the principal components of carbon-13 chemical shift tensors of guanosine measured using CSA amplification with those measured previously. 96

5.5 Experimental principal components of carbon-13 chemical shift tensors and tensor parameters for uridine. 97

5.6 Experimental principal components of carbon-13 chemical shift tensors and tensor parameters for 5-methyluridine. 98

5.7 Comparison of experimental and calculated principal components of CSA tensors for 2'-deoxythymidine. 99

5.8 Comparison of experimental and calculated principal components of CSA tensors for adenosine. 100

5.9 Comparison of experimental and calculated principal components of CSA tensors for cytidine. 101

5.10 Comparison of experimental and calculated principal components of CSA tensors for guanosine. 102

5.11 Comparison of experimental and calculated principal components of CSA tensors for uridine. 103

5.12 Comparison of experimental and calculated principal components of CSA tensors for 5-methyluridine. 107

6.1 Phosphorus-31 chemical shft tensors of sample **1**-**3**. 122

A.1 Examples of the shortest realizable pulse timings t^p for five-pulse sequences. 129

A.2 Comparison of anisotropy (ζ) and asymmetry (η) for glycine-1-^{13}C. . 134

Chapter 1

Introduction

1.1 Nuclear Magnetic Resonance

Nuclear Magnetic Resonance (NMR) is a phenomenon in which electromagnetic radiation is absorbed by molecules containing nuclei with a magnetic moment which arises from their intrinsic spin angular momentum. NMR occurs because the degeneracy of the nuclear spin energy levels is lifted by the Zeeman interaction between the nuclear magnetic moment and an external magnetic field $\mathbf{B}_0$. As a result of the Boltzmann population difference across the Zeeman levels, the sample possesses a macroscopic magnetization aligned with the field direction.

In pulse NMR experiments a radio-frequency (rf) field is applied perpendicular to $\mathbf{B}_0$ in the form of a short pulse which tilts the magnetization into the transverse plane. After the pulse the magnetization precesses around $\mathbf{B_0}$ at the Larmor frequency which corresponds to the energy difference between the Zeeman levels. The precessing transverse magnetization induces a voltage in a receiver coil which is wrapped around the sample. The resulting oscillating signal is recorded as a function of time by the receiver and is known as the free-induction decay (FID). A Fourier transform (FT) is used to produce a frequency spectrum from the FID.

Solution-state NMR spectroscopy has become a powerful method of examining molecular structure because the internal nuclear spin Hamiltonian is a sensitive probe of the local environment. For example, the precise value of the Larmor frequency depends on the surrounding bonds, an effect known as the chemical shift. Fine structure is observed in solution which is caused by a scalar coupling interaction between nuclei connected by chemical bonds.

NMR spectroscopy is inherently insensitive because of the small Zeeman polarization. Solutions to this problem include operating at higher magnetic fields and lower temperatures. In addition a variety of magnetization transfer methods have been introduced, such as cross polarization [1, 2], dynamic nuclear magnetization [3], the nuclear Overhauser effect [4, 5] and optical pumping [6, 7]. These allow optical polarization or enhanced magnetization on electrons or other nuclei to be transferred to the spin interest.

Pulsed FT NMR paved the way for modern NMR methodology, with the internal Hamiltonian manipulated by elaborate sequences of rf pulses. For example, new time dimensions can be incorporated by the insertion of incremented evolution periods prior to the detection of the FID, so that the resulting spectrum is a function of the multiple frequency co-ordinates [8]. Multi-dimensional NMR allows the separation of difference nuclear spin interaction in order to spread out the information from crowded spectra [9] and the correlation of pairs of coupled nuclei [10]. Other possibilities include the indirect observation of forbidden multiple-quantum transitions [11] and the investigation of dynamic processes [12, 13].

1.2 Solid State NMR

Solid-state NMR has become an important alternative to diffraction techniques, particularly for solids which lack long-range translational order. In solution molecules tumble rapidly, so that the anisotropic parts of the nuclear spin interactions are averaged to zero, resulting in high-resolution NMR spectra. In solids, however, molecule motion is usually restricted and for isotropic samples this results in broad resonances with a characteristic line shape known as powder patterns. Powder patterns from different chemical sites overlap with each other and resolution is poor.

Fortunately, resolution can be improved in solid-state NMR either by physically rotating the sample in space or by performing rotations in spin space using rf pulses. Both approaches mimic the effects of molecular motion in solution which make the anisotropic interactions time dependent. In the magic angle spinning (MAS) technique [14, 15] the sample is rotated about an axis inclined at an angle of 54.74° to $\mathbf{B}_0$. In particular, this results in the averaging of the chemical shift interaction to its isotropic value. In combination with heteronuclear decoupling and cross polarization from abundant proton spins MAS has become the method of choice for obtaining high-resolution solid-state NMR spectra of dilute spins –1/2, such as carbon-13 or nitrogen-15 [16]. However, MAS is not appropriate for narrowing the homogeneous lines which arise from networks of dipolar-coupled abundant spins, such as proton. In this situation spin-space averaging using multiple-pulse sequences designed using average Hamiltonian theory is more effective. Combinations of MAS and rf pulses CRAMPS (combined Rotation and multipulse spectroscopy) can improve the resolution further [17].

1.3 Measuring the Chemical Shift Anisotropy (CSA)

The anisotropic chemical shift provides a more detailed picture of the local electronic distribution than its isotropic average [18, 19]. With the development of first- principles computation methods, such as GIPAW [20], based on density functional theory and the plane-wave pseudopotential approach, the comparison between calculated and experimental CSA tensors offers a powerful probe of molecular structure. In principle, the tensor which describes the variation of the interaction with orientation can be measured directly from the three singularities observed in the powder pattern. In practice the overlap of different powder patterns makes this approach impossible. However, in the slow MAS regime when the spinning frequency is less than the chemical shift anisotropy (CSA) the NMR spectrum contains manifolds of rotational sidebands centered at each isotropic shift. The CSA tensor can be determined more accurately from the sideband patterns [21, 22], but a slow MAS rate is required to provide sufficient sidebands for analysis. However, overlap of different sideband manifolds complicates the analysis, and in order to overcome this problem a number of two-dimensional experiments have been developed.

One class of experiments reintroduces scaled or distorted powder patterns in one dimension, while retaining the isotropic fast MAS spectrum in the other. Direct approaches include experiments which switch the spinning axis between evolution and detection [23-26] or which stop the spinning altogether during the evolution period [27]. These experiments suffer from loss of signal during the long delays required to effect such changes. To overcome this drawback the magic angle hopping experiment

[28, 29] successively hops the sample in steps of 120° around the magic angle during the evolution period, so that the average chemical shift is the isotropic value. To increase the sensitivity the discrete hopping can be replaced by continuous MAS at very slow rates in a modification known as magic angle turning (MAT) [30-32]. Another approach involves reconstructing the powder patterns from data recorded as a function of spinning angle [33]. All the experiments described so far require special apparatus. An alternative method involves the application of a rotor-synchronized multiple-pulse sequence which reintroduces a part of the MAS averaged CSA interaction and hence results in a scaled powder pattern [34-41]. These experiments suffer from sensitivity to pulse imperfections and off-resonance effects.

Experiments in the second class correlate isotropic shifts in the evolution dimension with spinning sideband manifolds in the detection dimension. Some early attempts [42, 43] demonstrated an apparent separation of anisotropic and isotropic shifts by synchronizing the evolution time with the MAS rotor. However, this approach results in a concomitant restriction in the spectral width in the evolution dimension. This problem was alleviated to some extent by the use of a multiple-pulse sequence which scales the chemical shift during evolution [44]. A direct approach in which the MAS rate is switched between the two dimensions has also been demonstrated for this class [45]. An alternative experiment [46] involves sandwiching the evolution time between a TOSS (total suppression of sidebands) sideband suppression sequence [47] and its time-reversed counterpart. MAT, mentioned above, is essentially a constant-time variant of the TOSS-reverse TOSS approach [31, 48]. All the two-dimensional experiments in this class require many increments in order to obtain sufficient resolution of the isotropic shifts in the evolution dimension.

The final group of experiments restricts the isotropic shifts to the detection dimension where good resolution can be achieved without long acquisition times. The periodic signal in the evolution dimension arises only from the anisotropic part of the chemical shift and appears at multiples of MAS rate. Therefore, a small number of increments are sufficient and the time required for the experiment is minimized. The original PASS sequence proposed by Dixon [49] used a carefully timed sequence of π pulses prior to detection. This sequence prepares the magnetization such that a phase shift of magnitude $j\Theta$ results for the sideband at a frequency of $j\omega_r$ where the angle Θ is known as "pitch" of the sequence [50]. By combining spectra recorded with different Θ, Dixon was able to obtain a series of MAS spectra containing only one sideband from each site. However, the required pulse sequences have variable durations resulting in incomplete sideband separation because of differential transverse relaxation. Later Féaux De Lacroix *et al.* proposed a two-dimensional version of PASS [51] using two identical TOSS pulse sequences separated by a evolution time in which the magnetization is stored along the z-axis. The pitch can be varied continuously by incrementing the evolution time, during which transverse relaxation does not operate, so this method overcomes the problem of differential relaxation. However, only one half of the variable signal is retained by the storage pulses. Later Antzutkin *et al.* demonstrated a new 2D-PASS experiment [52] which dispensed with the storage pulses by employing constant time PASS sequences with arbitrary pitch. Experiments which belong to this third group are described as PASS-type experiments in this thesis. PASS-type experiments are generally simpler to implement and more efficient than the alternatives and are the method of choice for measuring CSA tensor parameters.

1.4 CSA Amplification

When the CSA is small PASS-type experiments necessarily involve slow MAS rates in order to give the optimum number of sidebands for a reliable analysis. This causes rotor instability and results in perturbations from partially averaged homonuclear dipolar interactions. In these circumstances PASS-type experiments which operate at a high MAS rate but still produce a slow-spinning sideband pattern in the evolution dimension are useful. For example, Kolbert *et al.* [53] proposed a two-dimensional MAS spin-echo experiment in which the evolution time is divided evenly by N – 1 π pulses which results in amplification of the modulation due to the CSA in the evolution dimension. For N = 2 the sideband pattern along a skew projection through the resulting two-dimensional spectrum is identical to that obtained with half the actual MAS rate. However, this is not the case when N > 2. A modification, known as the extended chemical shift (XCS) experiment [54], contains 2N – 1 π pulses applied within N rotor periods. The latter qualifies as a PASS-type experiment, since the isotropic chemical shift can be eliminated in the evolution dimension using two complementary datasets and a special transform. The sideband pattern in the evolution dimension is identical to that obtained with a MAS rate of $\omega_r/2N$. Stroheimer *et al.* [55] proposed the SPEED experiment which is similar to XCS, but isotropic shifts remain in the evolution dimension which is "replicated" to reduce the number of increments required. Finally, in the ROSES experiment [56] the isotropic shift is scaled in the evolution dimension but not removed and the resulting sideband patterns are different from those expected for MAS.

Recently, we have developed the CSA amplification experiment [57-59] which retains all the advantages of PASS. The isotropic shift is removed from the evolution dimension, and a minimal number of increments are sufficient to define the resulting periodic signal. Hence, long acquisition times can be avoided without loss of resolution of different chemical sites. However, CSA amplification correlates a fast MAS spectrum in the detection dimension with a sideband pattern in the evolution dimension in which the intensities are identical to those expected for a sample spinning at some fraction $1/x_a$ of the actual rate ω_r. These sidebands effectively result from an amplification by a factor x_a of the modulation caused by the CSA. CSA amplification is useful for reliably measuring small anisotropies without the need for slow MAS rates. More recently, CSA amplification has been combined with rotor synchronization acquisition to measure orientation distributions in polymer fibers [60] and with exchange NMR to study slow molecular dynamics [61]. The theoretical background to CSA amplification experiments is described in Chapter 2 of this thesis, while the details of their experimental implementation are discussed in Chapter 3.

The original CSA amplification experiment followed the basic PASS scheme of Féaux de Lacroix *et al.* The amplification factor x_a is determined by the fixed timings of the two identical sequences of π pulses which surround the evolution time. This version allowed amplification factors as high as 12 to be realized using up to 14 π pulses in total, but two separate experiments are required to reconstruct the final two-dimensional FID and so sensitivity is reduced. More recently, it has been shown [62] that CSA amplification with x_a up to 3 can be achieved by sequences of five π pulses with variable timings, after the fashion of the later 2D-PASS approach of Antzutkin *et al*. However, obtaining higher amplification factors using this method

requires concatenation of many such sequences, resulting in long durations and large numbers of pulses. For example, an amplification factor of 11 requires 23 π pulses over 16 rotor periods. Paragraph Chapter 4 describes a modified CSA amplification experiment [59] in which x_a increases linearly with the number of π pulses. This means that very high amplification factors can be achieved without resort to prohibitively large numbers of π pulses or long sequences. Therefore, the experiment operates at fast MAS rates allowing the use of modern heteronuclear decoupling sequences to further improve resolution. In particular, the combination of high x_a and XiX [63] heteronuclear decoupling is shown to be essential for measurements of the carbon-13 CSA tensor parameters in a mixture of the two optical isomers of a vinyl phosphonate modified nucleotide. A detailed experimental and computational study of the carbon-13 CSA tensors in six nucleosides: adenosine, 2'-deoxythymidine, uridine, cytidine, guanosine and 5-methyluridine is described in Chapter 5. Finally, Chapter 6 continues this theme with a preliminary high-resolution multi-nuclear solid-state NMR study of some novel vinylphosphonate-linked oligo-nucleotides.

Chapter 2

Theory of CSA Amplification

2.1 Quantum Mechanical Description of NMR

2.1.1 Quantum Mechanics of an Isolated Spin

The Cartesian components of spin angular momentum commute according to:

$$\left[\hat{I}_\alpha, \hat{I}_\beta\right] = i\hbar\hat{I}_\gamma \qquad 2.1.1$$

where α, β, $\gamma = x, y, z$ and cyclic permutations. From this commutation relation it follows that spin angular momentum is quantized according to:

$$\hat{I}^2\left|I,m\right\rangle = \hbar^2 I\left(I+1\right)\left|I,m\right\rangle \qquad 2.1.2$$

with the spin quantum number $I = 0, 1/2, 1, \ldots$ and:

$$\hat{I}_z\left|m\right\rangle = \hbar m\left|I,m\right\rangle \qquad 2.1.3$$

with the magnetic quantum number $m = I, I - 1, I - 2, \ldots, -I$. The $2I + 1$ eigenfunctions $\left|I,m\right\rangle$ are a series of spherical harmonics. The value of I is an intrinsic property of each isotope and results from the nuclear structure. This thesis is concerned exclusively with spin-1/2 nuclei. The eigenfunctions span a Hilbert space of dimension $2I + 1$. For spin-1/2 the eigenstates can be written:

$$\left|1/2\right\rangle = \begin{bmatrix} 1 \\ 0 \end{bmatrix} \quad \left|-1/2\right\rangle = \begin{bmatrix} 0 \\ 1 \end{bmatrix} \tag{2.1.4}$$

and the matrix representations of the three components of the spin angular momentum operator are:

$$\hat{I}_z = \frac{1}{2}\begin{bmatrix} 1 & 0 \\ 0 & -1 \end{bmatrix} \quad \hat{I}_x = \frac{1}{2}\begin{bmatrix} 0 & 1 \\ 1 & 0 \end{bmatrix} \quad \hat{I}_y = \frac{1}{2i}\begin{bmatrix} 0 & 1 \\ -1 & 0 \end{bmatrix} \tag{2.1.5}$$

The nuclear spin wavefunction $\left|\psi\right\rangle$ is a superposition of the $2I + 1$ eigenfunctions of spin angular momentum:

$$\left|\psi\right\rangle = \sum_m a_m \left|m\right\rangle \tag{2.1.6}$$

where a_m is a complex amplitude and $|a_m|^2$ is the probability that the spin is in the state $\left|m\right\rangle$. Given the wavefunction the expectation value of a macroscopic observable can be calculated from:

$$\left\langle\psi\left|\hat{Q}\right|\psi\right\rangle = \sum_{m,n} a_m a_n^* \left\langle n\left|\hat{Q}\right|m\right\rangle \tag{2.1.7}$$

where $\hat{Q}$ is the corresponding operator and $\left\langle n\right|$ is the row vector corresponding to the complex conjugate of state *n*. The evolution of the wavefunction can be established from the Schrödinger equation:

$$\hat{H}\psi\left(t\right) = i\hbar\frac{\partial\psi\left(t\right)}{\partial t} \tag{2.1.8}$$

where $\hat{H}$ is the Hamiltonian or energy operator for the system which represents the relevant nuclear spin interactions.

In NMR the degenerate $2I + 1$ nuclear energy levels are separated in the external field $\boldsymbol{B}_0$ by the Zeeman interaction. The corresponding Hamiltonian is:

$$\hat{H}_Z = -\gamma \hbar B_0 \hat{I}_z \qquad 2.1.9$$

The Zeeman eigenstates are proportional to the eigenfunctions of spin angular momentum and their energies are determined by the magnetic quantum number *m*

$$E_m = -\gamma B_0 \hbar m \qquad 2.1.10$$

where the magnetogyric ratio γ is a characteristic of each isotope.

2.1.2 Statistical Description of an Ensemble of Spins

For a statistical ensemble of spins each with a different wavefunction $|\psi\rangle$ the macroscopic magnetization observed in NMR is a sum of contributions from all the individual spins. Therefore, it is convenient to introduce a new operator, known as the density operator $\hat{\rho}$ where:

$$\hat{\rho} = \sum_{\psi} p_{\psi} |\psi\rangle\langle\psi| \qquad 2.1.11$$

where p_{ψ} is the probability of finding a spin in the state $|\psi\rangle$. The density operator allows the expectation value of a macroscopic observable $\hat{\boldsymbol{Q}}$ to be conveniently evaluated for the ensemble according to:

$$\overline{\langle \hat{Q} \rangle} = Tr\left\{\hat{\rho}\hat{Q}\right\} \qquad 2.1.12$$

The physical interpretation of the density matrix can be understood by considering its matrix elements:

$$\rho_{mn} = \langle m|\hat{\rho}|n\rangle = \sum_{\psi} p_{\psi} \langle m|\psi\rangle\langle\psi|n\rangle = \overline{a_m a_n^*} \qquad 2.1.13$$

where the over bar indicates an average over the ensemble. In the eigenbase of the Zeeman Hamiltonian, the diagonal elements of the density matrix represent the populations in the eigenstates $|m\rangle$. The off-diagonal elements show a coherent superposition or "coherence" between the eigenstates $|m\rangle$ and $|n\rangle$. This implies that the phases of the wavefunctions $|\psi\rangle$ are no longer random across the ensemble. The coherence ρ_{mn} which can be associated with a transition between the connected eigenstates, and the order of the coherence, p, is defined as the difference in the magnetic quantum numbers. Coherence of order ±1 corresponds to transverse magnetization with $p = -1$ detected by the NMR spectrometer. Coherences with $p \neq \pm 1$ can only be observed indirectly via the evolution dimension of a two-dimensional NMR experiment.

At thermal equilibrium the populations of the eigenstates $|m\rangle$ obey a Boltzmann distribution:

$$\rho_{nm} = \frac{\exp\left(-E_m/kT\right)}{\sum_m \exp\left(-E_m/kT\right)} \qquad 2.1.14$$

where the denominator is the partition function for the system. Hence, the density operator for an ensemble of isolated spins-1/2 at thermal equilibrium is:

$$\hat{\rho}_{eq} = \begin{bmatrix} \frac{1}{2} + \frac{\hbar\gamma B_0}{4k_B T} & 0 \\ 0 & \frac{1}{2} - \frac{\hbar\gamma B_0}{4k_B T} \end{bmatrix} \qquad 2.1.15$$

For positive magnetogyric ratio the population in the lower energy state $|\alpha\rangle$ is slightly higher than in $|\beta\rangle$ resulting in a macroscopic magnetization. Note that at thermal

equilibrium there is no coherence. The equilibrium density matrix can be expanded in terms of spin angular momentum operators:

$$\hat{\rho}_{eq} = \frac{1}{2}\hat{\mathbf{1}} + \frac{\hbar\gamma B_0}{4k_B T}\hat{I}_z \qquad 2.1.16$$

Only the second term which corresponds to the macroscopic magnetization can be manipulated by rf pulses, and the first term is normally ignored. The resulting reduced density operator can be represented by a magnetization vector which indicates the magnitude and direction of the macroscopic magnetization. The evolution of the density matrix for an ensemble of isolated spin-1/2 nuclei corresponds to the motion of the magnetization vector in spin space. This is the basis of the vector picture of NMR which is not discussed further in this thesis.

The time-dependent Schrödinger equation leads to an expression for the time evolution of the density operator:

$$\frac{d}{dt}\hat{\rho}(t) = -i\left[\hat{H}(t), \hat{\rho}(t)\right] \qquad 2.1.17$$

which is known as the Liouville-von Neumann equation. The formal solution is:

$$\hat{\rho}(t) = \hat{U}(t,0)\,\hat{\rho}(0)\hat{U}^{-1}(t,0) \qquad 2.1.18$$

where $\hat{\rho}(0)$ is the density operator at thermal equilibrium, and $\hat{U}(t,0)$ is known as the propagator which describes the evolution during the period from 0 to *t*. In general $\hat{U}(t,0)$ is given by:

$$\hat{U}(t,0) = \hat{T}\exp\left\{-i\int_0^t \hat{H}(t')\,dt'\right\} \qquad 2.1.19$$

where $\hat{T}$ is the Dyson time-ordering operator relevant for Hamiltonians containing non-commuting components [64]. Eq. 2.1.19 is difficult to evaluate, but if the Hamiltonian is time-independent then $\hat{U}(t,0)$ is a simple exponential operator:

$$\hat{U}(t,0) = \exp\left(-i\hat{H}t\right) \qquad 2.1.20$$

Hence the integral in Eq. 2.1.19 is usually approximated by a simple time-ordered product:

$$\hat{U}(t,0) = \prod_{j=0}^{n-1} \exp\left\{-i\hat{H}(j\Delta t)\Delta t\right\} \qquad 2.1.21$$

where $\hat{H}(j\Delta t)$ is Hamiltonian for the *j*th intervals of duration Δt in which the Hamiltonian may be considered time-independent. This approach is used for numerical simulations of NMR experiments, as described in Chapter 3.

2.1.3 The Nuclear Spin Hamiltonian

The NMR Hamiltonian contains internal terms which describe the interactions of the nuclear spins with their surroundings and external terms which describe interactions with the experimental apparatus.

$$\hat{H} = \hat{H}_{ext} + \hat{H}_{\text{int}} \qquad 2.1.22$$

Following the standard convention in NMR a factor $\hbar$ will be omitted from the following discussion and the Hamiltonian written in units of angular frequency.

The main internal Hamiltonians are:

- $\hat{H}_{CS}$ - the chemical shift Hamiltonian. The interaction of the nuclear spin with magnetic fields which arise from electronic currents induced by the external magnetic field in the surrounding molecular orbitals.
- $\hat{H}_{DD}$ - the dipolar coupling Hamiltonian. The direct through-space dipole-dipole interaction between the magnetic moments of neighboring nuclear spins.
- $\hat{H}_{J}$ - the *J* or scalar coupling Hamiltonian. The indirect through-bond dipole-dipole interaction between magnetic moments of nuclear spins via the bonding electrons.
- $\hat{H}_{Q}$ - the quadrupolar interaction Hamiltonian. The interaction between the nuclear quadrupole moment of a spin with $I > 1/2$ and the surrounding electric field gradient.

2.1.4 The NMR Experiment

The Hamiltonian of the Zeeman interaction is:

$$\hat{H}_z = -\gamma \hat{I}_z \mathbf{B}_0 = \omega_0 \hat{I}_z \qquad 2.1.23$$

where $\omega_0 = -\gamma \boldsymbol{B}_0$ is the Larmor frequency which corresponds to the energy difference between the Zeeman levels. From the Liouville von-Neumann equation (Eq. 2.1.17) the effect of the Zeeman Hamiltonian on the density operator is:

$$\hat{\rho}(t) = \exp\left(-i\omega_0 \hat{I}_z t\right) \hat{\rho}(0) \exp\left(i\omega_0 \hat{I}_z t\right) \qquad 2.1.24$$

When the initial density operator corresponds to transverse magnetization this describes a precession about the $\boldsymbol{B}_0$ field at the Larmor frequency.

In pulsed NMR spectroscopy the transverse magnetization is generated by a rf field $\boldsymbol{B}_1$ which is applied perpendicular to $\boldsymbol{B}_0$. The rf field oscillates with frequency ω_{rf} which is close to resonant with the Larmor frequency and can be written:

$$\mathbf{B}_1(t) = \begin{bmatrix} 2B_1 \cos\left(\omega_{rf} t + \varphi_{rf}\right) & 0 & 0 \end{bmatrix} \qquad 2.1.25$$

where φ_{rf} is the phase of the rf pulse. It is convenient to view the oscillating rf field as a sum of two components which rotate in the xy-plane at the same frequency but in opposite directions. Only the component that rotates as the same sense as the Larmor precession affects the motion of the spins. Therefore, the rf field may be approximated as:

$$\mathbf{B}_1(t) = \begin{bmatrix} B_1 \cos\left(\omega_{rf} t + \varphi_{rf}\right) & B_1 \sin\left(\omega_{rf} t + \varphi_{rf}\right) & 0 \end{bmatrix} \qquad 2.1.26$$

and the rf Hamiltonian is:

$$\hat{H}_{rf}(t) = \omega_1 \cos\left(\omega_{rf} t + \varphi_{rf}\right)\hat{I}_x + \omega_1 \sin\left(\omega_{rf} t + \varphi_{rf}\right)\hat{I}_y \qquad 2.1.27$$

with $\omega_1 = -\gamma_1 \mathbf{B}_1$. The absolute value of ω_1 is called the nutation frequency and is a measure of the amplitude of the rf field.

$\hat{H}_{rf}$ can be made independent of time by transforming to a rotating frame which rotates about the external magnetic field at ω_{rf}. In this frame, the external Hamiltonian becomes:

$$\hat{H}_{ext} = \Omega \hat{I}_z + \omega_1 \left(\hat{I}_x \cos\varphi_{rf} + \hat{I}_y \sin\varphi_{rf}\right) \qquad 2.1.28$$

where $\Omega = \omega_0 - \omega_{rf}$ is the offset. When the rf field is close to resonance with the Larmor frequency so that $\Omega << \omega_1$ the first term can be neglected. Assuming $\varphi_{rf} = 0$ and $\rho(0) = \rho_{eq}$ the Liouville von-Neumann equation (Eq. 2.1.18) gives:

$$\hat{\rho}\left(\tau_p\right) = \exp\left(-i\beta\hat{I}_x\right)\frac{\hbar\gamma B_0}{4k_B T}\hat{I}_z \exp\left(i\beta\hat{I}_x\right) = \frac{\hbar\gamma B_0}{4k_B T}\left(\hat{I}_z\cos\beta - \hat{I}_y \sin\beta\right) \qquad 2.1.29$$

where τ_p is the duration of the pulse and β is its flip angle with:

$$\beta = \omega_1 \tau_p \qquad 2.1.30$$

When $\beta = \pi/2$ rad the effect of the pulse is to produce a coherence proportional to $\hat{I}_y$ which corresponds to transverse magnetization along the *y*-axis of the rotating frame. The NMR signal is proportional to the expectation value of the raising operator:

$$\hat{I}^+ = \hat{I}_x + i\hat{I}_y \qquad 2.1.31$$

so that the observed magnetization is:

$$M^+(t) \propto Tr\left\{\hat{I}^+ \rho(t)\right\} \qquad 2.1.32$$

with $\rho(t)$ given by Eq. 2.1.24.

2.2 Chemical Shift

2.2.1 Chemical Shift Hamiltonian

The chemical shift arises from the interaction between the nucleus and the magnetic field $\boldsymbol{B}_{induced}$ due to electronic currents in the surrounding bonds induced by $\boldsymbol{B}_0$. The nuclear spin experiences a local magnetic field $\boldsymbol{B}_{loc}$ which can be written:

$$\boldsymbol{B}_{loc} = \boldsymbol{B}_0 + \boldsymbol{B}_{induced} \qquad 2.2.1$$

$\boldsymbol{B}_{loc}$ causes the Larmor precession frequency to be slightly altered, so that a shift appears in the NMR spectrum which reflects the local electronic environment. The induced field is linearly dependent on the static magnetic field:

$$B_{induced} = \delta^{L} \cdot \boldsymbol{B}_{0} = \begin{bmatrix} \delta_{xx}^{L} & \delta_{xy}^{L} & \delta_{xz}^{L} \\ \delta_{yx}^{L} & \delta_{yy}^{L} & \delta_{yz}^{L} \\ \delta_{zx}^{L} & \delta_{zy}^{L} & \delta_{zz}^{L} \end{bmatrix} \begin{bmatrix} 0 \\ 0 \\ B_{0} \end{bmatrix} = \begin{bmatrix} \delta_{xz}^{L} B_{0} \\ \delta_{yz}^{L} B_{0} \\ \delta_{zz}^{L} B_{0} \end{bmatrix} \qquad 2.2.2$$

where $\boldsymbol{\delta}^{L}$ is a second-rank Cartesian tensor known as the chemical shift tensor in the laboratory frame, *L*. The tensor is required because the induced field is usually in a different direction to the external magnetic field. For example, the element $\delta_{xy}{}^{\mathrm{L}}$ measures the component of the field induced along the *x*-axis by an external field along *y*.

In Cartesian coordinates, the chemical shift Hamiltonian can be written as:

$$\begin{aligned} \hat{H}_{CS} &= -\gamma \hat{\boldsymbol{I}} \cdot \delta^{L} \cdot \boldsymbol{B}_{0} \\ &= -\gamma \hat{\boldsymbol{I}} \cdot \boldsymbol{B}_{induced} \\ &= -\gamma B_{0} \delta_{xz}^{L} \hat{I}_{x} - \gamma B_{0} \delta_{yz}^{L} \hat{I}_{y} - \gamma B_{0} \delta_{zz}^{L} \hat{I}_{z} \end{aligned} \qquad 2.2.3$$

In the secular approximation, when the Zeeman interaction is much stronger than the internal interactions, only the last term of the Eq. 2.2.3 is retained and the chemical shift Hamiltonian becomes:

$$\hat{H}_{CS} \cong -\gamma B_{0} \delta_{zz}^{L} \hat{I}_{z} \qquad 2.2.4$$

2.2.2 Principal Axis System

The chemical shift tensor is often specified in its principal axis system (PAS), *P*, a frame in which it is diagonal:

$$\delta^{P} = \begin{bmatrix} \delta_{xx}^{P} & 0 & 0 \\ 0 & \delta_{yy}^{P} & 0 \\ 0 & 0 & \delta_{zz}^{P} \end{bmatrix} \qquad 2.2.5$$

where the diagonal elements are called the principal components. The orientation of the PAS is determined by the chemical environment and is fixed relative to the molecular frame, *M*. According to convention [65]:

$$\left|\delta_{zz}^{P}-\delta_{iso}\right| \geq \left|\delta_{xx}^{P}-\delta_{iso}\right| \geq \left|\delta_{yy}^{P}-\delta_{iso}\right| \qquad 2.2.6$$

so that $\delta_{yy}{}^{P}$ is located between $\delta_{xx}{}^{P}$ and $\delta_{zz}{}^{P}$, but closer to $\delta_{xx}{}^{P}$. The isotropic chemical shift δ_{iso} is the trace of the chemical shift tensor:

$$\delta_{iso}=\frac{1}{3}Tr\left(\delta^{P}\right)=\frac{1}{3}\left(\delta_{xx}^{P}+\delta_{yy}^{P}+\delta_{zz}^{P}\right) \qquad 2.2.7$$

Two further parameters, the chemical shift anisotropy, ζ, and the asymmetry, η, are often used to represent the principal components. These are defined as:

$$\zeta=\left(\delta_{zz}^{P}-\delta_{iso}\right) \quad \eta=\frac{\left(\delta_{yy}^{P}-\delta_{xx}^{P}\right)}{\zeta} \qquad 2.2.8$$

The anisotropy corresponds to the largest deviation in chemical shift from the isotropic value. (see Figure 2.1)

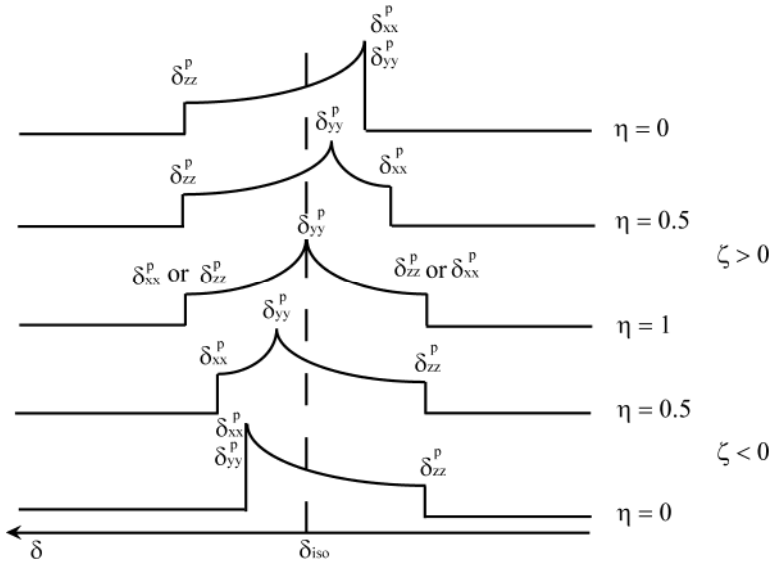

Figure 2.1: Powder pattern lineshapes for a single molecular site with CSA.

In the Herzfeld-Berger convention [22], the principal components of a tensor are described by three parameters: the isotropic value δ_{iso}, i.e., span Ω and the skew κ

$$\delta_{iso} = \frac{1}{3}\left(\delta_{xx} + \delta_{yy} + \delta_{zz}\right)$$
$$\Omega = \delta_{zz} - \delta_{xx} \qquad \kappa = \frac{\delta_{xx} + \delta_{zz} - 2\delta_{yy}}{\delta_{zz} - \delta_{xx}} \qquad 2.2.9$$

With the principal components assigned so that $\delta_{xx} < \delta_{yy} < \delta_{zz}$, span Ω is always positive, but κ varies between –1 and +1 with the extreme values corresponding to axially symmetric tensors.

2.2.3 Irreducible Spherical Tensors

In addition to expressing spin interactions in terms of Cartesian tensors, they may also be represented using irreducible spherical tensors. This is more convenient for calculating the effects of rotations between co-ordinate frames, as well as other unitary transformations. The relationship between the components of an irreducible tensor A in the two frames X and Y is:

$$A_{mq}^{Y} = \sum_{p=-m}^{+m} A_{mp}^{X} D_{pq}^{(m)}\left(\Omega_{XY}\right) \qquad 2.2.10$$

where the Wigner matrix elements [66] $D_{pq}^{(m)}\left(\Omega_{XY}\right)$ depend on the Euler angles Ω_{XY} which describe the relative orientation of the two frames.

In the spherical tensor formalism [67], Eq. 2.2.3 is:

$$\hat{H}_{CS} = \sum_{k=0}^{2} \sum_{q=-k}^{k} (-1)^q A_{kq}^L \hat{T}_{k-q}^L \qquad 2.2.11$$

where A_{kq}^L and $\hat{T}_{k-q}^L$ are irreducible spherical tensors of rank k which represent the space and spin parts of the Hamiltonian, respectively. The spin part involves a combination of the spin operators and the external magnetic field. In the secular approximation, Eq. 2.2.11 reduces to [68]:

$$\hat{H}_{CS} = \sum_{k=0}^{2} A_{k0}^L \hat{T}_{k0}^L \qquad 2.2.12$$

If $\boldsymbol{B}_0$ is parallel to the z-axis, the tensor components $\hat{T}_{k0}^L$ can be written:

$$\begin{aligned} \hat{T}_{00}^L &= -\frac{1}{\sqrt{3}} B_0 \hat{I}_z \\ \hat{T}_{10}^L &= 0 \\ \hat{T}_{20}^L &= \sqrt{\frac{2}{3}} B_0 \hat{I}_z \end{aligned} \qquad 2.2.13$$

The second-rank tensor in the Cartesian representation can be decomposed into three irreducible tensors of rank k = 0, 1 and 2, with a total of nine components. The rank 0 spatial tensor component $A_{00} = \sqrt{3}\gamma\delta_{iso}$ is the isotropic part which is invariant to frame transformations. The anti-symmetric rank 1 tensor component A_{10} has no first-order effect on the NMR spectrum, since the corresponding spin operator tensor $\hat{T}_{10}^L = 0$. The rank 2 spatial tensor component is the anisotropic part which has a large effect on the NMR spectrum in solids but vanishes in liquid-state NMR due to fast molecular tumbling. The rank 2 irreducible spherical tensor components in the PAS can be expressed as:

$$A_{20}^{P} = \sqrt{\frac{3}{2}}\gamma\left(\delta_{zz}^{P} - \delta_{iso}\right) = \sqrt{\frac{3}{2}}\gamma\zeta$$
$$A_{2\pm1}^{P} = 0 \qquad 2.2.14$$
$$A_{2\pm2}^{P} = -\frac{\eta}{\sqrt{6}}A_{20}^{P}$$

However, $\boldsymbol{B}_0$ is fixed in the laboratory frame, so it is combined into the space part of the Hamiltonian giving:

$$\hat{H}_{CS} = \omega_0\delta_{iso}\hat{I}_z + \sum_{m=-2}^{+2} A_{2m}'^{P} D_{m0}^{(2)}\left(\Omega_{PL}\right)\hat{I}_z \qquad 2.2.15$$

with:

$$A_{20}'^{P} = \gamma B_0\left(\delta_{zz}^{P} - \delta_{iso}\right) = -\omega_0\zeta$$
$$A_{2\pm1}'^{P} = 0 \qquad 2.2.16$$
$$A_{2\pm2}'^{P} = -\frac{\eta}{\sqrt{6}}A_{20}^{P}$$

2.3 Magic Angle Spinning

2.3.1 Spinning Sidebands

In solution-state NMR the anisotropic part of the chemical shift tensor is averaged because of rapid molecular tumbling. In contrast molecular motion is usually restricted in solids, so that the anisotropic information can be extracted from the NMR spectrum. In solid-state NMR powdered or amorphous samples with a uniform and continuous distribution of molecular orientations are often used. For isolated spin-1/2 nuclei the spectrum of such an isotropic sample contains a powder pattern for each chemical site. The powder pattern has a characteristic lineshape as illustrated in Figure

2.2(a) which shows the wideline carbon-13 cross polarization NMR spectrum of glycine.

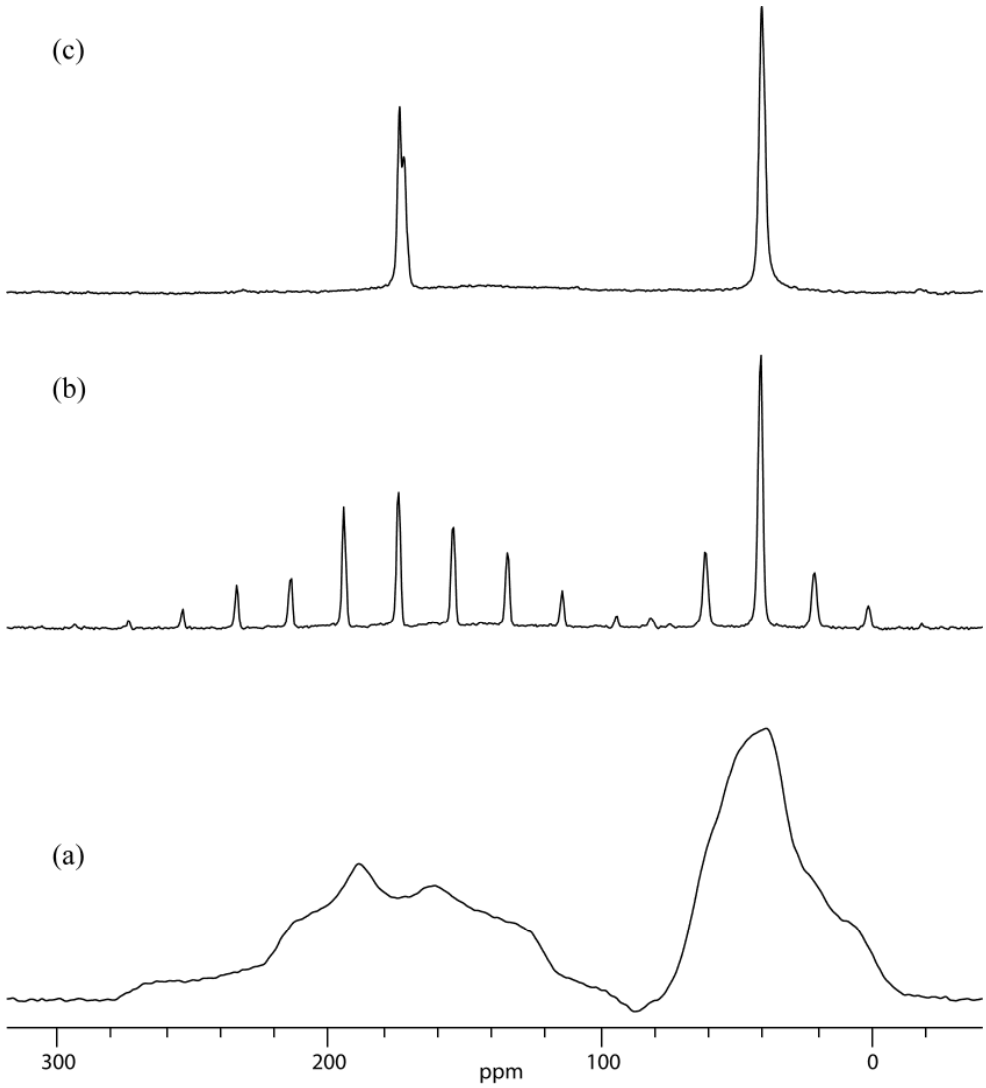

Figure 2.2: Carbon-13 CP spectra of glycine powder: (a) static; (b) CPMAS at a MAS rate of 1.25 kHz; (c) CPMAS at a MAS rate of 15 kHz. Proton decoupling with a field strength of 100 kHz was applied throughout the acquisition period.

MAS involves mechanically rotating the sample about an axis inclined at the magic angle of 54.74° to the external magnetic field. When the MAS rate is rapid compared to the chemical shift anisotropy MAS can completely average the

anisotropic part of the chemical shift interaction, resulting in solution-like spectra which contain only the isotropic shifts, as shown in Figure 2.2(c) At slower MAS rates, the spectrum contains a manifold of spinning sidebands, centered at each isotropic line and separated by the spinning frequency, as shown in Figure 2.2(b).

With MAS the chemical shift Hamiltonian and the resulting precession frequency become time-dependent. The rotor frame *R* has its *z*-axis oriented along the spinning axis at the magic angle to the external field and rotates at the MAS rate ω_r. The time-dependent Euler angles which relate the rotor frame to the laboratory frame are $\Omega_{RL} = (\omega_r t, \beta_{RL}, 0)$ where β_{RL} is the magic angle. Since only linear operators are involved in the chemical shift Hamiltonian, the vector model is sufficient to evolution of individual crystallites in the sample. Following from Eq. 2.2.15 the time-dependent precession frequency becomes:

$$\begin{aligned}\omega(\Omega_{PL}(t)) &= \omega_{iso} + \sum_{m'=-2}^{2}\sum_{m=-2}^{2} A_{2m'}^{P} D_{m'-m}^{(2)}(\Omega_{PR}) D_{-m0}^{(2)}(\Omega_{RL}(t)) \\ &= \omega_{iso} + \sum_{m'=-2}^{2}\sum_{m=-2}^{2} A_{2m'}^{P} D_{m'-m}^{(2)}(\Omega_{PR}) d_{-m0}^{(2)}(\beta_{RL}(t)) \exp(im\omega_r t)\end{aligned} \qquad 2.3.1$$

If the isotropic frequency ω_{iso} is incorporated into the summation, Eq. 2.3.1 can be written as a Fourier series:

$$\omega(t;\Omega_{PR}) = \sum_{m=-2}^{2} \omega^{(m)}(\Omega_{PR}) \exp(im\omega_r t) \qquad 2.3.2$$

with coefficients given by

$$\omega^{(m)}(\Omega_{PR}) = \sum_{m'=-2}^{2} A_{2m'}^{P} D_{m'-m}^{(2)}(\Omega_{PR}) d_{-m0}^{(2)}(\beta_{RL}) + \delta_{m0}\omega_{iso} \qquad 2.3.3$$

where δ_{m0} is 1 when m = 0, and 0 otherwise, and the isotropic shift depends on the offset from ω_{rf} :

$$\omega_{iso} = \omega_0 \left(1+\delta_{iso}\right) - \omega_{rf} \qquad 2.3.4$$

This analysis separates the time and orientation dependence of the precession frequency. Hence, we consider a "carousel" of crystallites [69] which have the same values of α_{PR} and β_{PR}, but different values of γ_{PR}. Therefore, the time-dependent precession frequency $\omega\left(t;\gamma_{PR}\right)$ of sites within a carousel may be written as:

$$\omega_c\left(t;\gamma_{PR}\right) = \sum_{m=-2}^{2} \omega_c^{(m)}\left(\gamma_{PR}\right)\exp\left(im\omega_r t\right) \qquad 2.3.5$$

where the subscript *c* indicates the carousel. The subscript *PR* will be dropped for simplicity.

The complex Fourier components $\omega_c^{(m)}\left(\gamma\right)$ have following useful symmetries:

$$\begin{aligned} \omega_c^{(m)}\left(\gamma\right) &= \left[\omega_c^{(-m)}\left(\gamma\right)\right]^* \\ \omega_c^{(m)}\left(\gamma\right) &= \omega_c^{(m)}\left(0\right)\exp\left(im\gamma\right) \end{aligned} \qquad 2.3.6$$

Note that $\omega_c^{(0)} = \omega_{iso}$ under the MAS condition.

Neglecting T_2 decay, the NMR signal component arising from a site in the carousel may be written [69] as:

$$S_c^{MAS}\left(t;\gamma\right) = \exp\left\{i\Theta_c\left(t,0;\gamma\right)\right\} \qquad 2.3.7$$

The phase angle accumulated by the transverse magnetization from 0 to *t*, $\Theta_c\left(t,0;\gamma\right)$ is defined as:

$$\begin{aligned}\Theta_c(t,0;\gamma) &= \int_0^t dt\omega_c(t;\gamma) \\ &= \omega_{iso}t + \xi_c(t;\gamma) - \xi_c(0;\gamma) + \varphi_c(0;\gamma)\end{aligned} \qquad 2.3.8$$

where:

$$\begin{aligned}\xi_c(t;\gamma) &= \sum_{m\neq 0} \frac{\omega_c^{(m)}(\gamma)\exp(im\omega_r t)}{im\omega_r} \\ &= \sum_{m\neq 0} \frac{\omega_c^{(m)}(0)\exp(im(\omega_r t+\gamma))}{im\omega_r}\end{aligned} \qquad 2.3.9$$

The difference $\xi_c(t;\gamma)-\xi_c(0;\gamma)$ is the phase angle accumulated due to evolution under the anisotropic part of the chemical shift interaction during the acquisition time, and $\varphi_c(0;\gamma)$ is the initial phase of the magnetization which is independent of orientation under normal circumstances.

In the limit of very fast spinning the ξ function vanishes and the NMR spectra show only isotropic lines as in solution. The intensities of the spinning sidebands can be extracted using the plane-wave expansion of the Kronecker δ function:

$$\begin{aligned}\exp\{i\xi_c(0;\varphi)\} &= \frac{1}{2\pi}\int_0^{2\pi} d\theta\delta(\theta-\varphi)\exp\{i\xi_c(0;\theta)\} \\ &= \sum_{j=-\infty}^{+\infty}\exp(ij\varphi)\frac{1}{2\pi}\int_0^{2\pi} d\theta\exp\{i\xi_c(0;\theta)\}\exp(-ij\theta) \\ &= \sum_{j=-\infty}^{+\infty}\exp(ij\varphi)F_j\end{aligned} \qquad 2.3.10$$

where the coefficients F_j are:

$$F_j = \frac{1}{2\pi}\int_0^{2\pi} d\theta\exp\{i\xi_c(0;\theta)\}\exp(-ij\theta) \qquad 2.3.11$$

Assuming the initial phase $\varphi_c(0;\gamma)$ is zero, Eq. 2.3.7 becomes:

$$S_c^{MAS}(t;\gamma) = \sum_{j',j=-\infty}^{\infty} F_{j'}^* F_j \exp\{i\gamma(j-j')\} \exp\{i(\omega_{iso} + j\omega_r)t\} \qquad 2.3.12$$

This equation results in a centerband at ω_{iso} with a manifold of sidebands separated by multiples of the spinning frequency. Integration over γ gives the carousel intensity of the jth sideband at $\omega_{iso} + j\omega_r$:

$$I_{j,c}^{MAS} = \sum_{j'=-\infty}^{\infty} F_{j'}^* F_j \frac{1}{2\pi} \int_0^{2\pi} \exp\{i\gamma(j-j')\} d\gamma = F_j^* F_j \qquad 2.3.13$$

If the distribution of γ values in the carousel in uniform and continuous the sideband intensities are real and positive. In order to obtain the correct sideband intensities for a powder sample, further integration over the Euler angles α and β is required:

$$I_j^{MAS} = \int_0^{2\pi} d\alpha \int_0^{\pi} \sin\beta d\beta F_j^* F_j \qquad 2.3.14$$

The spinning sideband intensities can be analyzed to extract the principal components of the chemical shift tensor, following the procedures of Maricq and Waugh [21] and Herzfeld and Berger [22]. Because of limitations in the computer resources available at the time, the former rejected explicit calculations of the sideband intensities in powdered samples as the basis of an iterative method of matching the experimental sideband envelope. Instead, they proposed a discrete of the moment analysis which relies on an accurate measurement of the intensities of all the sidebands arising from a particular site. This is often not feasible due to spectral overlap, and the outer sidebands make an increasingly large contribution to the moments, but these are of low intensity and significantly affected by the noise.

To overcome these problems Herzfeld and Berger [22] evaluated the sideband intensities by numerical integration of Eq. 2.3.14 and then plotted the ratio I_j/I_0 as a

function of two parameters. For historical reasons they chose a reduced span Ω/ω_r and the skew κ of the tensor, rather than the now standard anisotropy ζ and asymmetry η. These were used to provide a graphical determination of the CSA tensor parameters, since the contours corresponding to each of the observed values of $I_{\pm j}/I_0$ intersect at the correct values of Ω/ω_r and κ. If sideband manifolds from different sites overlap this analysis can be limited to the well-resolved sidebands, since only the intensity ratio relative to the centerband needs to be measured.

The graphical approach is rarely used these days, but it forms the basis of a number of iterative fitting procedures for obtaining the shift tensor parameters. For example, Antzutkin *et al.* [70] obtained the joint confidence limits on ζ and η from plots of the χ^2 error surface. In this approach the single crystallite FID was calculated directly in the time domain using Eq. 2.3.7 over a single rotor period. The resulting signal was Fourier transformed and the amplitude evaluated at $j\omega_r$ out to $j = \pm 11$ before powder averaging to produce the required sideband intensities. These were interpolated to provide a dense grid as a function of ζ/ω_r and η. The χ^2 between experimental and calculated intensities was then minimized for each point on the pre-calculated grid by altering only the intensity scaling factor. The resulting error surface was plotted, allowing the chemical shift tensor parameters to be identified from the minimum and their joint confidence regions to be evaluated. This procedure has been used to extract chemical shift tensor parameters and their confidence limits in the following Chapters.

2.3.2 Sideband Manipulation

Many solid-state NMR experiments have been devised which manipulate the spinning sidebands using sequences of π pulses with carefully chosen timings. These experiments achieve the desired effect by modifying the initial phase $\varphi_c(0;\gamma)$ in Eq. 2.3.8. Consider a sequence of duration T consisting of q π pulses applied along the x-axis of the rotating frame at timings given by $-T + t_p$. Assuming acquisition starts at time $t = 0$, the initial phase is given by:

$$\varphi_c(0;\gamma) = \Theta_c(0, -T + t_q; \gamma) - \Theta_c(-T + t_q, -T + t_{q-1}; \gamma) + \ldots (-1)^n \Theta_c(-T + t_1, -T; \gamma) \quad 2.3.15$$

which can be written:

$$\varphi_c(0;\gamma) = \omega_{iso}\tau_{seq} + \xi_c(0;\gamma) - (-1)^q \left\{ 2\sum_{p=1}^{q} (-1)^p \xi_c(-T + t_p; \gamma) + \xi_c(-T; \gamma) \right\} \quad 2.3.16$$

with:

$$\tau_{seq} = T - 2\sum_{p=1}^{n} (-1)^{n+p} t_p \quad 2.3.17$$

TOSS

The total suppression of spinning sidebands (TOSS) experiment was invented by Dixon [47] and is used to suppress the spinning sidebands, resulting in a solution-like spectrum of isotropic shifts. TOSS prepares the initial phases of the magnetization as:

$$\varphi_c(0;\gamma) = \xi_c(0;\gamma) + \omega_{iso}\tau_{seq} \quad 2.3.18$$

so that the carousel signal is:

$$S_c^{TOSS}(t;\gamma) = \exp\{i\xi_c(t;\gamma)\}\exp\{i\omega_{iso}(t+\tau_{seq})\} \qquad 2.3.19$$

In practice TOSS sequences also satisfy the spin-echo condition τ_{seq} = 0, so that the initial phase is independent of the isotropic shift. Using the plane-wave expansion of the Kronecker δ function:

$$S_c^{TOSS}(t;\gamma) = \sum_{j=-\infty}^{+\infty} F_j \exp(i\gamma j)\exp\{i(\omega_{iso} + j\omega_r)t\} \qquad 2.3.20$$

Integration over γ gives the carousel intensity of the TOSS sidebands. Eq. 2.3.20 shows that the sideband have complex intensities with an initial phase which depends on crystallite orientation. Hence, for an isotropic sample, the sidebands cancel in the integral over γ. However, the centerband has a complex amplitude with the same phase for all crystallites in the carousel. In order to generate the required initial phase given by Eq. 2.3.18, the π pulse timings must be such that the last term in Eq. 2.3.16 is zero. Therefore, the TOSS timings satisfy:

$$2\sum_{p=1}^{q}(-1)^p \xi_c(-T + t_p;\gamma) + \xi_c(-T;\gamma) = 0 \qquad 2.3.21$$

PASS

Dixon's phase adjusted spinning sidebands (PASS) experiment [49] can be used to generate spectra containing a single sideband from each manifold. These sequences of π pulses produce an additional phase shift $-j\Theta$ for the jth sideband where Θ is a constant for each set of timings known as the pitch. For PASS the initial phase is:

$$\varphi_c(0;\gamma) = \xi_c(0;\gamma) - \xi_c(\Theta/\omega_r;\gamma) \qquad 2.3.22$$

so that the carousel signal for $\tau_{seq} = 0$ is:

$$S_c^{PASS}(\Theta,t;\gamma) = \exp\{i\xi_c(t;\gamma) - \xi_c(\Theta/\omega_r;\gamma)\}\exp\{i\omega_{iso}t\} \qquad 2.3.23$$

Using the plane-wave expansion:

$$S_c^{PASS}(\Theta,t;\gamma) = \sum_{j,j'=-\infty}^{+\infty} F_{j'}^* F_j \exp\{i(j-j')\gamma\}\exp(-ij'\Theta)\exp\{i(\omega_{iso} + j\omega_r t)\} \qquad 2.3.24$$

so that the carousel intensity of the *j*th sideband is:

$$I_{j,c}^{PASS}(\Theta,t;\gamma) = \sum_{j'=-\infty}^{+\infty} F_{j'}^* F_j \int_0^{2\pi} \exp\{i(j-j')\gamma\}\exp(-ij'\Theta)\,d\gamma = F_{j'}^* F_j \exp(-ij\Theta) \qquad 2.3.25$$

Eq. 2.3.25 shows that the PASS sidebands have the same amplitude as for MAS but are shifted in phase by $-j\Theta$. A number of sequences with different pitches produce a series of spectra which can be summed so that all sidebands except one cancel.

Féaux de Lacroix *et al.* proposed a two-dimensional PASS experiment [51] which separates the sidebands in the ω_1 dimension. The pulse sequence shown in Figure 2.3 contains two consecutive TOSS pulse sequences separated by the evolution

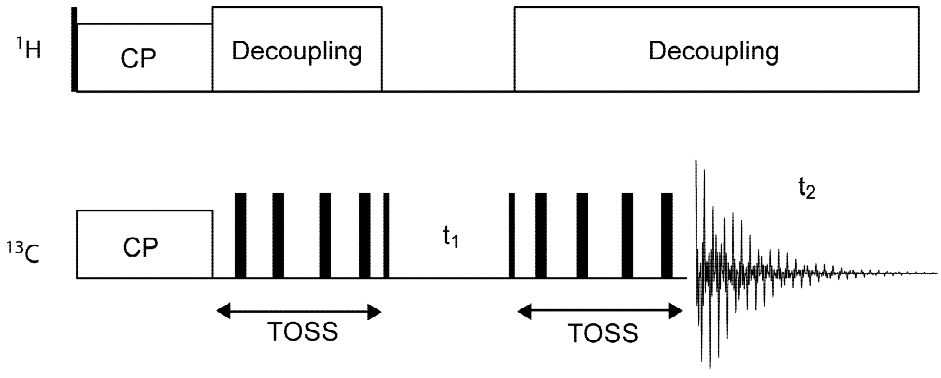

Figure 2.3: Pulse sequence for the two-dimensional PASS experiment due to Féaux de Lacroix *et al.*[51] Narrow and broad filled rectangles represent π/2- and π-pulses, respectively.

time t_1 in which the magnetization is temporarily stored along the z-axis as the sample spins. In this experiment $\Theta = \omega_r t_1$ so that the pitch can vary continuously over a full period in the evolution dimension.

The required FID is reconstructed by taking the echo combination of two experiments in which the phase of the $\pi/2$ storage pulse and the receiver phase are shifted simultaneously. The amplitude of the stored component depends on the phase accumulated during the first TOSS sequence so that the signals from the two experiments are:

$$S_c^{2D-PASS}(t_1,t_2;\gamma) = \begin{Bmatrix} \cos\{\xi_c(0;\gamma)\} \\ \sin\{\xi_c(0;\gamma)\} \end{Bmatrix} \exp\left\{i\left[\omega_{iso}t_2 + \xi_c(t_1+t_2;\gamma)\right]\right\} \qquad 2.3.26$$

The echo combination gives:

$$S_c^{2D-PASS}(t_1,t_2;\gamma) = \exp\left\{-i\left[\xi_c(0;\gamma)\right]\right\} \exp\left\{i\left[\omega_{iso}t_2 + \xi_c(t_1+t_2;\gamma)\right]\right\} \qquad 2.3.27$$

The isotropic shifts only evolve in the t_2 dimension and the signal is periodic in t_1, so that only a few t_1 increments are necessary. Using the plane-wave expansion gives:

$$S_c^{2D-PASS}(t_1,t_2;\gamma) = \sum_{j,j'=-\infty}^{+\infty} F_{j'}^* F_j \exp\{-i(j-j')\gamma\} \exp(ij\omega_r t_1) \exp\left\{i\left[(\omega_{iso} + j\omega_r)t_2\right]\right\} \qquad 2.3.28$$

Integration over γ gives the carousel intensity for the sideband at co-ordinates ($j\omega_r$, $j\omega_r$) in the two-dimensional spectrum:

$$I_c^{2D-PASS} = F_j^* F_j \qquad 2.3.29$$

which is identical to the result for MAS except that now the sidebands are separated in ω_1 according to j.

Following Féaux de Lacroix *et al.*, Antzutkin *et al.* proposed a modified 2D-PASS experiment with the pulse sequence shown in Fig. 2.3. In this experiment the storage period is not necessary, since the pitch is made to vary as required by continuously changing the timings of five π pulses over a single rotor period. The timings are solutions to Eq. 2.3.22 which also satisfy the spin-echo condition and are shown graphically in Figure 2.4.

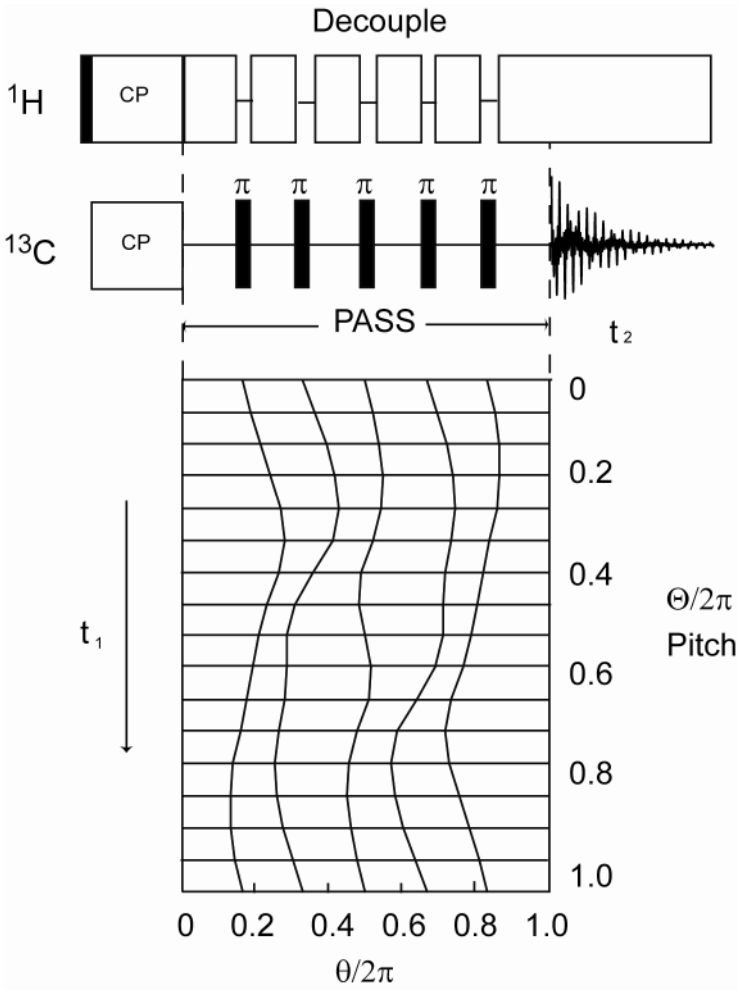

Figure 2.4: Pulse sequence for the 2D-PASS experiment due to Antzutkin *et al.* Adapted from Ref. [52].

The signal resulting from this experiment is:

$$S_c^{2D-PASS}\left(\Theta,t_2;\gamma\right)=\exp\left\{-i\left[\xi_c\left(0;\gamma\right)-\xi_c\left(\Theta/\omega_r;\gamma\right)\right]\right\}\exp\left(i\omega_{iso}t_2\right) \qquad 2.3.30$$

Using the plane-wave expansion:

$$S_c^{2D-PASS}\left(\Theta,t_2;\gamma\right)=\sum_{j,j'=-\infty}^{+\infty}F_{j'}^{*}F_j\exp\left\{-i\left(j-j'\right)\gamma\right\}\exp\left(-ij\Theta\right)\exp\left\{i\left[\left(\omega_{iso}+j\omega_r\right)t_2\right]\right\} \qquad 2.3.31$$

which is identical to Eq. 2.3.28 with $\Theta=-\omega_r t_1$. A Fourier transform with respect to the pitch results in the separation of the sideband manifolds according to j.

CSA Amplification

The CSA amplification experiment [57-59] also produces a two-dimensional spectrum in which the sidebands are separated in ω_1 according to j. However, the sideband intensities are identical to those expected for a sample spinning frequency of $1/x_a$ of the actual rate ω_r where x_a is known as the amplification factor. Note that x_a is not necessarily an integer, no greater than 1. The carousel signal necessary for CSA amplification is:

$$S_c\left(t_1,t_2;\gamma\right)=\exp\left\{ix_a\left[\xi_c\left(t_1;\gamma\right)-\xi_c\left(0;\gamma\right)\right]\right\}\exp\left\{i\left[\omega_c^{(0)}t_2+\xi_c\left(t_2;\gamma\right)-\xi_c\left(0;\gamma\right)\right]\right\} \qquad 2.3.32$$

which corresponds to the desired x_a-fold amplification of the modulation due to the anisotropic part of the chemical shift during t_1. The CSA amplification sideband intensities can be extracted using the modified expansion:

$$\exp\left(ix_a\xi_c\left(0;\phi\right)\right)=\sum_{j=-\infty}^{\infty}F_j^{'}\exp\left(ij\phi\right) \qquad 2.3.33$$

with coefficients:

$$\begin{aligned} F_j^{'} &= \frac{1}{2\pi}\int_0^{2\pi} d\theta \exp\left\{ix_a\xi_c\left(0;\theta\right)\right\}\exp\left(-ij\theta\right) \\ &= \frac{1}{2\pi}\int_0^{2\pi} \exp\left\{\sum_{m\neq 0}\frac{\omega_c^{(m)}\left(0\right)\exp\left(im\theta\right)}{m\left(\omega_r / x_a\right)}\right\}\exp\left(-ij\theta\right)d\theta \end{aligned} \qquad 2.3.34$$

which are identical to the F_j in Eq. 2.3.11 except for the replacement of ω_r by ω_r/x_a.

The original CSA amplification experiment [57] is shown in Figure 2.5 and uses two identical sequences each containing p π pulses after the fashion of the two-dimensional PASS sequence due to Féaux de Lacroix *et al.* The signal in Eq. 2.3.31 is obtained if the timings of the pulses are chosen so that the phase accumulated during one sequence is $x_a\xi_c\left(0;\gamma\right)$. The FID is reconstructed by taking the echo combination of two experiments recorded with the pulse phase φ_3 set to π/2 and π, respectively, is:

$$\begin{aligned} S_c\left(t_1,t_2;\gamma\right) &= \exp\left\{i\left[-x_a\xi_c\left(t_1;\gamma\right)+x_a\xi_c\left(0;\gamma\right)\right]\right\} \\ &\times\exp\left\{i\left[\omega_{iso}t_2+\xi_c\left(t_2;\gamma\right)-\xi_c\left(0;\gamma\right)\right]\right\} \end{aligned} \qquad 2.3.35$$

Uisng the expansions of Eqs. 2.3.10 and Eq. 2.3.35 this can be written:

$$\begin{aligned} S_c\left(t_1,t_2;\gamma\right) &= \sum_{j',j,k',k=-\infty}^{+\infty} F_{j'}'F_j'^{*}F_{k'}^{*}F_k\exp\left\{i\left(j'+k-j-k'\right)\gamma\right\} \\ &\times\exp\left(ij\omega_r t_1\right)\exp\left\{i\left(\omega_{iso}+k\omega_r\right)t_2\right\} \end{aligned} \qquad 2.3.36$$

Integration over γ gives the intensity of the sideband at co-ordinates ($j\omega_r$, $k\omega_r$) in the two-dimensional spectrum as:

$$I_{c,j,k} = \sum_{j'=-\infty}^{\infty} F_{j'}'^{*}F_j'F_{j-j'+k}^{*}F_k \qquad 2.3.37$$

since the only non-vanishing components are those which have $j - j' + k - k' = 0$.

Projecting onto ω_1 gives the intensity of the sideband at $j\omega_1$ as:

$$I_{c,j} = \sum_{k=-\infty}^{\infty} I_{c,j,k} = \sum_{j'=-\infty}^{\infty} F_j^{'} F_{j'}^{'*} \sum_{k=-\infty}^{\infty} F_{j-j'+k}^{*} F_k \qquad 2.3.38$$

From the normalization condition of $\exp\{i\xi_c(0;)\}$, the coefficients F_k satisfy

$$\begin{aligned} \sum_{k=-\infty}^{\infty} F_{n+k} F_k^{*} &= 0 \qquad n \neq 0 \\ \sum_{k=-\infty}^{\infty} F_{n+k} F_k^{*} &= 1 \qquad n = 0 \end{aligned} \qquad 2.3.39$$

so that the only non-zero component of the summation over k occurs for $j = j'$, and Eq.2.3.38 becomes:

$$I_{c,j} = F_j^{'*} F_j^{'} \qquad 2.3.40$$

The intensities of the sidebands in the ω_1 projection mimic those that would be recorded with the CSA amplified by a factor x_a or equivalently the sample spinning rate scaled by $1/x_a$. In a similar fashion, the intensities in the projection onto ω_2 are given by:

$$I_{c,k} = F_k^{*} F_k \qquad 2.3.41$$

which is identical to the MAS result.

CSA amplification can be achieved if the timings of q π pulses are chosen so that the phase accumulated during the sequences is:

$$\varphi_c(0;\gamma) = x_a \xi_c(0;\gamma) \qquad 2.3.42$$

Following Eq. 2.3.16 and assuming that the spin-echo condition is satisfied, the pulses timings must satisfy:

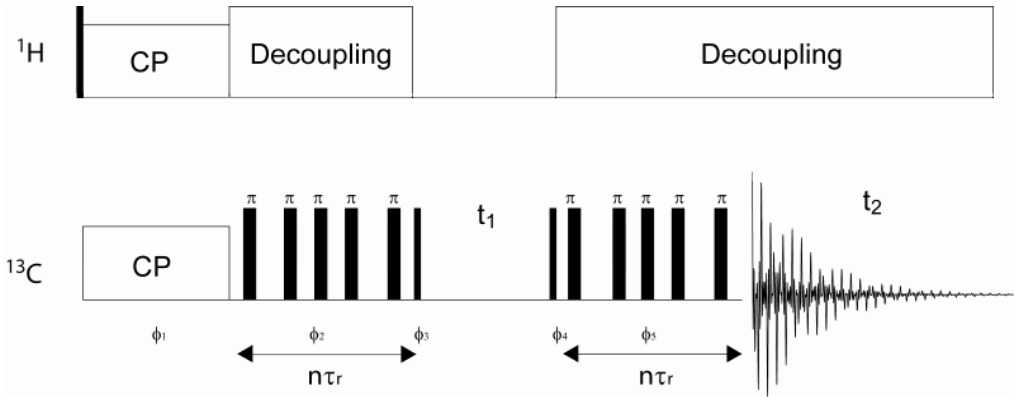

Figure 2.5: The original CSA amplification pulse sequence. Narrow and broad filled rectangles represent π/2- and π-pulses, respectively.

$$\left(x_a - 1\right)\xi_c\left(0;\gamma\right) + \left(-1\right)^q \left\{ 2\sum_{p=1}^{q}\left(-1\right)^p \xi_c\left(t_p - T;\gamma\right) + \xi_c\left(-T;\gamma\right)\right\} = 0 \qquad 2.3.43$$

Using the definition of ξ_c, this can be expanded to give four simultaneous equations for t_p:

$$x_a - 1 + \left(-1\right)^q \exp\left(-im\omega_r T\right)\left\{ 2\sum_{p=1}^{q}\left(-1\right)^p \exp\left(im\omega_r t_p\right) + 1\right\} = 0 \qquad 2.3.44$$

for $m = \pm 1$ and $m = \pm 2$. Many timings for sequences with $2 < x_a < 12$ for q = 4, 5 and 7 have been found both analytically and numerically and are given in Ref. [58].

Chapter 3

CSA Amplification Methodology

3.1 Experiments

3.1.1 Pulse Sequence

The original pulse sequence used for CSA amplification is shown in Figure 2.4. Enhanced magnetization generated by cross polarization evolves under a sequence of q π pulses applied at timings calculated from the required amplification factor x_a. Subsequently, one component of the magnetization is stored parallel to the z-axis for an evolution time t_1 which is incremented by some convenient fraction, usually 1/16 or 1/32, of the rotor period. The stored magnetization is reconverted to transverse magnetization by a $\pi/2$ pulse which evolves under an identical sequence of q π pulses before detection in t_2. In order to reconstruct the required two-dimensional FID two experiments are necessary in which the phase of the storage pulse is alternated $\pi/2$, π when using sequences with an odd number of π pulses. These can be combined in the receiver by simultaneously shifting the reference phase from 0 to $\pi/2$.

Cross Polarization

Carbon-13 has a natural abundance of 1.1 % and a magnetogyric ratio roughly one quarter that of the proton. Therefore, cross polarization [1, 2] (CP) is often used to improve the sensitivity of carbon-13 NMR spectra by transferring proton magnetization to carbon-13 spins before acquiring the signal. In the CP experiment at low MAS rates, a $\pi/2$ pulse is applied to the proton channel to generate transverse magnetization, followed by a spin-locking pulse with rf amplitude B_{1H} and a phase shifted by $\pi/2$. Simultaneously, a pulse is applied on the carbon-13 channel with the rf amplitude carefully calibrated so that the Hartmann-Hahn matching condition [1]

$$\gamma_H B_{1H} = \gamma_C B_{1C} \qquad 3.1$$

is satisfied. Under this condition the Zeeman levels of proton and carbon-13 spins in the rotating frame have the same energy separation and magnetization can be transferred between them via the heteronuclear dipolar coupling. The carbon-13 signal is enhanced by as much as γ_H/γ_C and in addition the relaxation delay is now determined by the relative rapid spin-lattice relaxation of protons. The combination of these two factors allows a significant reduction in experiment time.

Decoupling

In organic solids heteronuclear dipolar couplings to the abundant strongly-coupled proton spin system cause a broadening of the carbon-13 line. As the system is homogeneous in the definition of Maricq and Waugh [21], the broadening cannot be completely removed by MAS even at rates in excess of the magnitude of the heteronuclear dipolar coupling. Therefore, high-power proton decoupling is applied during periods of carbon-13 chemical shift evolution in the CSA amplification

experiment. Continuous wave (CW) rf irradiation on the proton channel causes the heteronuclear dipolar coupling to be averaged to zero over the NMR timescale. The efficiency of decoupling increases with rf amplitude, but decreases at higher MAS rates when the resulting rotations in sample and spin space interfere with one another.

The two-pulse phase modulation (TPPM) technique [71] reduces the linewidth more efficiently than CW decoupling at a comparable rf amplitude, especially at higher MAS rates. This method involves the application of a train of rf pulses on the proton channel with flip angles close to π rad and phases which alternate $\pm \varphi/2$ where φ is typically between 10° and 70°. The efficiency of the decoupling is sensitive to the precise setting of the flip angle and the phase modulation angle. More recently, a variant of TPPM known as XiX [63] was introduced in which φ is set to π rad and the pulse duration depends on the MAS period. Efficient decoupling is achieved whenever the pulse width exceeds one rotor period and unwanted synchronization conditions where the decoupling is compromised are avoided. The synchronization conditions are largely independent of the MAS rate and the decoupling rf amplitude. Since the phase modulation is fixed only a single parameter, the pulse width, needs to be calibrated.

Note that for CSA amplification experiments heteronuclear decoupling should be interrupted during carbon-13 π pulses in order to avoid satisfying unwanted Hartmann-Hahn conditions. CW or XiX decoupling has been used throughout this thesis.

3.1.2 Pulse Calibration

All sideband manipulation experiments require that the flip angle of the π pulses should be carefully calibrated in order to reduce sideband phase and amplitude distortions. In practice, the quality of the sideband suppression in a TOSS experiment with an identical number of π pulses is a suitable criterion by which to judge the accuracy of the calibration. The delays implemented between the π pulses must be reduced in order to take account of their finite width. If adjacent π pulses overlap, an additional delay equal in duration to the rotor period can be inserted between them without affecting the outcome of the experiment. However, in order to preserve the spin-echo condition, a further delay of equal duration must be inserted at an appropriate point in the sequence to compensate for the additional evolution of the isotropic chemical shift. For sequences with five π pulses, errors due to incorrectly calibrated pulses can be reduced by shifting the relative phases of successive pulses through the series 0°, 330°, 60°, 330°, 0°. This procedure has been used by Antzutkin *et al.*[69] to improve sideband suppression in five-pulse TOSS sequences. Further error compensation can be achieved by replacing the simple π pulses by composite pulses, such as $(\pi/2)_0\pi_{\pi/2}(\pi/2)_0$ [72] and $(\pi/2)_0\pi_{4\pi/3}(\pi/2)_0$ [73] or by using phase cycling.

3.1.3 Phase Cycling

As with all NMR methods the correct operation of the CSA amplification experiment relies on the observed signal containing only contributions which arise from a restricted set of the possible coherence transfer processes caused by each pulse.

The most common way of selecting the required contributions is by addition of signals derived from a set of experiments in which the phases of the rf pulses and the receiver are shifted in some systematic way. This is known as "phase cycling". A convenient way to describe the restriction of the final signal is by a "coherence transfer pathway" which takes the form of a diagram indicating the order of the coherence which is required to evolve during each delay in the pulse sequence. All coherence transfer pathways start with equilibrium magnetization and end with single-quantum coherence of order p = −1 corresponding to the observable operator I^+.

The basis of all phase cycling is the transformation of *p*-quantum coherence under rotation about the *z*-axis:

$$\exp\left(-i\varphi I_z\right)\sigma_p \exp\left(i\varphi I_z\right) = \sigma_p \exp\left(-ip\varphi\right) \qquad 3.2$$

where σ_p is the part of the density operator corresponding to coherence order *p*. A pulse represented by a propagator *U* can cause transfer of coherence of order *p* into all possible orders *p′* so that

$$U\sigma_p^- U^{-1} = \sum_{p'} \sigma_{p'}^+ \qquad 3.3$$

where σ^+ and σ^- are the density operators before and after the pulse. The effect of phase shifting the pulse is seen by applying Eq. (3.1)

$$U\left(\varphi\right)\sigma_p U\left(\varphi\right)^{-1} = \sum_{p'} \sigma_{p'}^+ \exp\left(-i\Delta p\varphi\right) \qquad 3.4$$

with $\Delta p = p - p'$. Therefore, the phase shift imposed on the coherence by the pulse $U(\varphi)$ depends on the change in coherence order Δp produced. This property allows the

separation of different coherence orders, since the phase shifts imposed this way are carried over into the detected signal.

Phase cycling involves the repetition of the pulse sequence N_i times with the addition of the resulting signals while incrementing the phase of the *i*th pulse by an angle

$$\varphi_i = 2\pi n_i / N_i \qquad 3.5$$

where $n_i = 0, 1, \ldots N_i - 1$. Each of the N_i observed signals arises from all possible coherence transfer pathways, but their sum can be restricted to contributions from pathways involving a given change in coherence order by acquisition of the signal with a corresponding phase shift in the receiver reference signal

$$\varphi_{ref} = -\Delta p_i \varphi_i \qquad 3.6$$

Note that the change in coherence order selected by the appropriate receiver phase shift is not unique, and a set of pathways is selected

$$\Delta p_i = \Delta p_i^{required} \pm kN_i \qquad 3.7$$

with k an integer. The full coherence transfer pathway can be selected by independently phase cycling each pulse according to the desired change in coherence order.

For the CSA amplification experiment undesirable signals arise from incomplete refocusing by the q π pulses resulting from resonance offset effects or B_1 field inhomogeneity. These can be removed and the desired signal retained by selecting $\Delta p = \pm 2$ for each pulse independently, but this results in a phase cycle with at least 3^q steps and unacceptably long experiment times. However, the “Cogwheel”

procedure [73, 74] for designing more efficient phase cycles was introduced recently. For example, Cogwheel cycling allows the full coherence transfer pathway for excitation followed by a five-pulse TOSS sequence to be selected by a minimal 11-step phase cycle. In general for a sequence with q π pulses, $2q + 1$ steps are required. All odd π pulses are cycled through an identical set of phases given by

$$\varphi_n = -\frac{2\pi qn}{2q+1} \qquad 3.8$$

while the excitation pulse and all even π pulses are cycled through

$$\varphi_n = -\frac{2\pi\left(q+1\right)n}{2q+1} \qquad 3.9$$

Cogwheel phase cycling is used to remove signal resulting from incomplete refocusing by π pulses in the modified CSA amplification experiments described in Chapter 4.

3.1.4 Typical Experimental Parameters

All of the experiments described in this Thesis were performed on a Varian InfinityPlus dual-channel spectrometer, operating at a proton frequency of 300.07 MHz. Two double-resonance MAS probes were used. These take 4 mm and 7 mm outside diameter rotors and allow maximum rf field amplitudes of approximately 100 kHz and 62.5 kHz, respectively. Further experimental details for individual experiments are given in the figure captions.

3.1.5 Data Processing

In the CSA amplification experiment the periodic nature of the evolution in the t_1 dimension means that there is no linewidth in ω_1. As a result, there is no need for the data processing methods [75] normally applied to obtain pure absorption lineshapes in two-dimensional NMR spectra. Reconstruction of the FID in the receiver as described in Section 3.1.1 allows the two-dimensional spectrum to be obtained by a straightforward complex Fourier transform with respect to both t_1 and t_2 after weighting and zero filling as normal in the detection dimension. However, to preserve the periodicity of the signal in t_1 it is important that no weighting functions are applied in the indirect dimension. Because the signal is phase modulated in t_1 the two-dimensional peaks which result have mixed phase "phase-twist" [75] lineshapes. Fortunately, the vanishing ω_1 linewidth ensures that there is no detrimental effect on the resolution in the spectrum. Phase corrections in ω_2 can be made by inspection of the $\omega_1 = 0$ slice. However, a further ω_1-dependent phase correction is usually required because of the finite widths of the $\pi/2$ storage pulses. The processing procedure [58] for the CSA amplification experiment is illustrated in Figure 3.1. The t_1 interferograms produced by a complex Fourier transform with respect to t_2 are shown in (a), while the spectrum resulting from a further complex Fourier transform with respect to t_1 is shown in (b). Phase correction in ω_2 gives a purely absorptive $\omega_1 = 0$ slice as in (c), but a small ω_1-dependent phase error remains. Finally, (d) shows the result of applying a frequency-dependent phase correction in ω_1. Because of the mixed phase nature of the lineshapes, any phase correction in ω_1 affects the appearance of the spectrum in the ω_2 dimension.

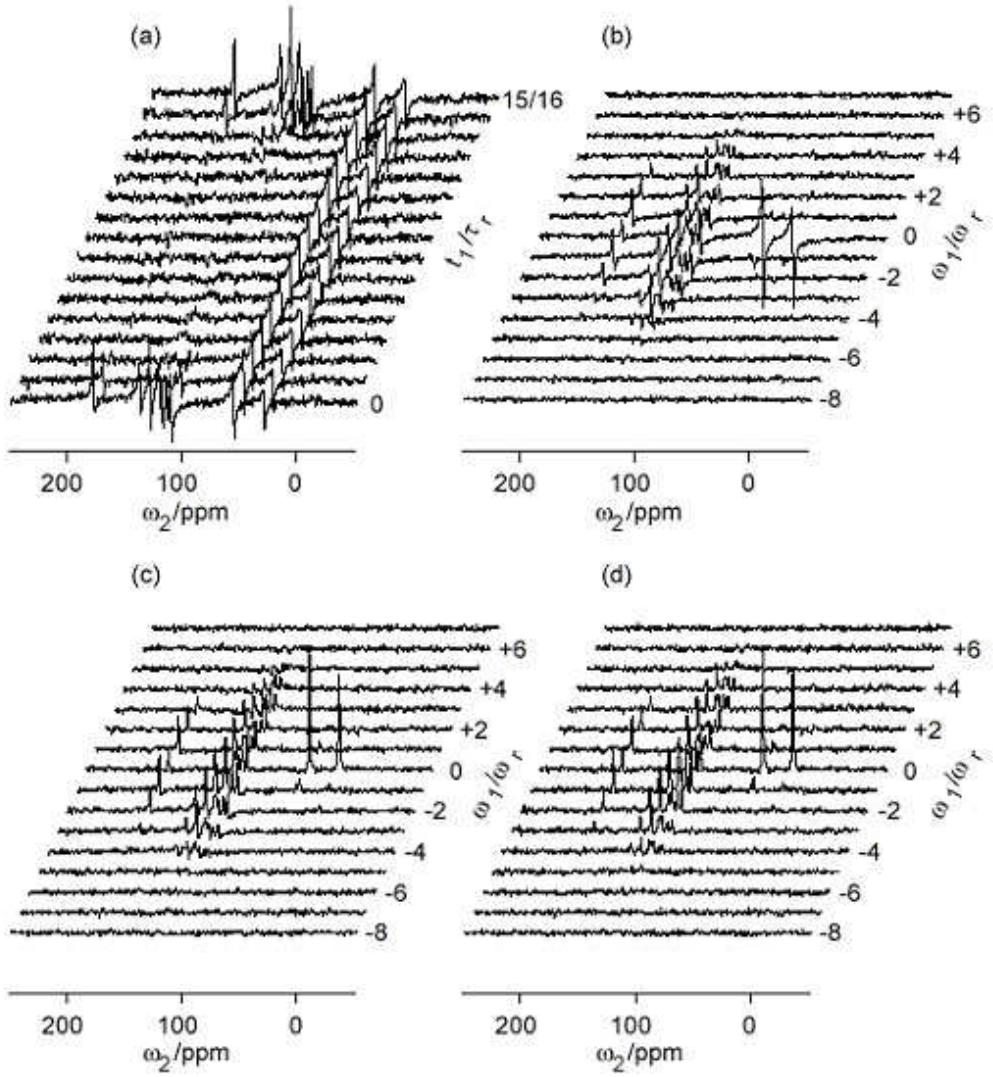

Figure 3.1: Processing procedure for the CSA amplification experiment. (a) Interferograms produced after weighting in t_2, followed by complex Fourier transformation with respect to t_2. (b) Spectrum resulting from a subsequent Fourier transformation with respect to t_1. (c) Spectrum after phase correction in the ω_2 dimension in which the ω_1 = 0 slice is purely absorptive, while a small ω_1-dependent phase error is apparent across the rest of the spectrum. (d) Spectrum after application of a frequency-dependent phase correction in the ω_1 dimension. Adapted from Ref. [58].

3.2 Simulations

3.2.1 Spectral Simulations

Simulation of MAS spectra requires numerical evaluation of the Liouville-von-Neumann equation Eq. 2.1.17 which allows the powder FID to be calculated directly during each iteration. In simulations the propagator U which describes the spin dynamics is usually approximated by the product in Eq. 2.1.21. Since the propagators are generated by diagonalizing the matrix representation of H, optimized linear algebra algorithms can be used to speed up the calculations [76]. Further efficiency gains can be made by exploiting symmetry, such as the time-translation relationship between the MAS rotor phase $\omega_r t$ and the Euler angle γ [77]. The symmetry of the problem with respect to the Euler angles α and β is such that the powder average need only be evaluated over one octant of the unit sphere [77]. Several software packages are available which combine efficient simulations with least-squares fitting in order to extract the CSA parameters and evaluate the associated errors from a statistical analysis. SIMPSON [78] is a powerful software package for simulation solid-state NMR experiments and is designed to work as a “computer spectrometer”. The program has been optimized for fast calculation of complicated NMR experiments on rotating powder samples and can be used to verify of experiment design and check experimental imperfections.

3.2.2 Powder Averaging

Calculated lineshapes are easily generated by summing a number of single crystallite contributions to the overall powder lineshape

$$S(t) = \frac{1}{8\pi^2} \int_0^{2\pi} d\alpha \int_0^{2\pi} d\beta \sin\beta \int_0^{2\pi} d\gamma S(t;\Omega_{PL}) \qquad 3.2.1$$

a procedure often described as "powder averaging". As mentioned above for the MAS case the orientations of the crystallites can be limited to a single octant of the unit sphere because of symmetry considerations. As there is no analytical solution to the integrals in the above equation, the powder averaging is approximated as a weighted summation of single-crystal spectra representing a large set of crystalline orientations uniformly distributed over the unit sphere:

$$S(t) = \sum_{k=1}^{N} \sum_{l-1}^{M} S(t;\, \alpha^k, \beta^k, \gamma^l) \frac{\omega_k}{M} \qquad 3.2.2$$

where the averaging is split into M γ^l angles with contributions from N pairs of α^k and β^k powder angles with normalized weightings ω_κ. If the crystallite orientations chosen for the summation are selected at random or fall on a uniform grid, then a dense mesh is required to reliably reproduce the experimental pattern, resulting in long computation times. For an iterative fitting procedure it is important that the calculations are as efficient as possible, so much effort has been expended on designing powder averaging schemes which allow a sparse sampling of the orientations without compromising the accuracy of the results. Recent examples are based on integration by a Gaussian spherical quadrature [77] or involve generating sets of orientations which are uniformly distributed over the unit sphere by minimizing a fictional repulsive potential between them [79].

3.2.3 Measurements of CSA Tensor Parameters

The capabilities of SIMPSON for iterative fitting of experimental spectra have been enhanced by its interface with the MINUIT optimization package [80] which allows the combination of different minimization procedures, as well as error estimation.

CSA parameters were measured from sideband intensities by simulating spectra using SIMPSON and minimising the root mean square difference between the experimental and simulated data. The simulated spectra were obtained using 31 (α, β) crystallite orientations distributed according to the Lebedev scheme [77]. 40 γ angles were used according to the gcompute method in SIMPSON. Error analysis was carried out using the CERN MINUIT optimization package. The confidence regions on the two CSA parameters ζ and η are bounded by the contours $\chi^2 = \chi^2_{\min} + 2.3$ (68.3% confidence limit) and $\chi^2 = \chi^2_{\min} + 6.17$ (95.4 confidence limit) [70].

Chapter 4

Developments of CSA amplification Experiment

4.1 Introduction

In this chapter, an alternative CSA amplification experiment is described which results in large amplification factors up to 48 using the pulse sequence shown in Figure 4.1. In addition, the two separate experiments required to reconstruct the final two-dimensional FID in the original version are no longer required, so sensitivity is increased. With large x_a the experiment can operate at higher MAS rates which allows the incorporation of state-of-art heteronuclear XiX decoupling schemes and it is this aspect which is demonstrated in particular here.

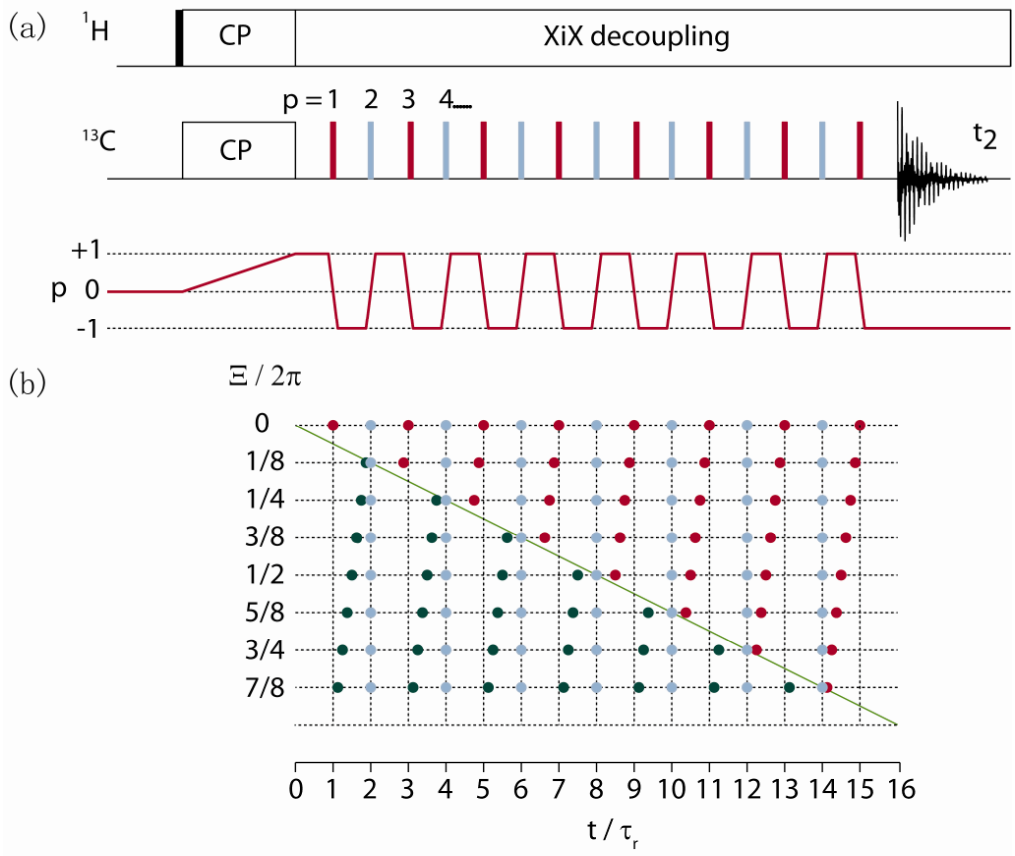

Figure 4.1: Modified CSA amplification pulse sequence [59]. Ξ performs a role similar to that of the pitch in 2D-PASS. The sequence corresponding to Ξ = 0 is shown in (a), in which red and blue rectangles represent odd and even carbon-13 π-pulses, respectively. Even-numbered π-pulses coincide with a rotor echo; odd-numbered ones occur $\Xi\tau_r/2\pi$ prior to a rotor echo. Odd-numbered pulses below the line are delayed by an additional rotor period to ensure that the end of the sequence coincides with a spin echo. The timings for the π-pulses required for CSA amplification factor of 16 are indicated in (b), along with the corresponding values of Ξ.

4.2 Theory

As described in Section 2.3 the two-dimensional FID resulting from a CSA amplification experiment is:

$$S_c(t_1,t_2;\gamma) = exp\{i[x_a(\xi_c(t_1;\gamma)-\xi_c(0;\gamma))]\} \times exp\{i[\omega_c^{(0)}t_2+\xi_c(t_2;\gamma)-\xi_c(0;\gamma)]\} \quad 4.2.1$$

In the alternative CSA amplification experiment described here, each "t_1 increment" is generated by a different sequence of q π pulses. Each sequence prepares the magnetization with a different phase at the start of acquisition according to

$$\phi_c(0;\gamma) = x_a\xi_c(0;\gamma) - x_a\xi_c(0;\gamma+\Xi) \quad 4.2.2$$

where the angle Ξ is a function of π-pulse timings, but independent of crystallite orientation. Note that Ξ performs a role similar to that of the pitch in 2D-PASS. Therefore, the FID resulting from the alternative experiment can be expressed as

$$S_c(\Xi,t_2;\gamma) = exp\{i[x_a(\xi_c(\Xi;\gamma)-\xi_c(0;\gamma))]\} \times exp\{i[\omega_c^{(0)}t_2+\xi_c(t_2;\gamma)-\xi_c(0;\gamma)]\} \quad 4.2.3$$

Following the treatment in Section 2.3 by expanding the ξ_c function and intergrating over γ gives

$$S_c(\Xi,t_2;\gamma) = \sum_{j,j',k=-\infty}^{\infty} F_j'^{*}F_{j'}'F_{j'-j+k}F_k \exp(-ij\Xi)\exp\left\{i\left(\omega_c^{(0)}+k\omega_r\right)t_2\right\} \quad 4.2.4$$

Projecting onto the ω_1 dimension the intensity of the sideband at $j\omega_r$ is

$$I_{j,c} = F_j'^{*}F_j' \quad 4.2.5$$

which is identical to the original CSA amplification experiment. For a powder sample, integration over the Euler angles α and β is required to obtain the correct sideband intensities.

For the modified experiment, the required initial phase in Eq.4.2.1 must be equal to the phase accumulated during the sequence of π pulses given by Eq. 2.3.16. Setting $\tau = 0$, this gives

$$0 = (x_a - 1)\xi_c(0;\gamma) - x_a\xi_c(0;\gamma + \Xi) + (-1)^q \left\{ 2\sum_{p=1}^{q} (-1)^p \xi_c\left(t^{(p)} - T;\gamma\right) + \xi_c(-T;\gamma) \right\} \quad 4.2.6$$

For simplicity, T is assumed to be an integer number of rotor periods and q is assumed to be odd. In this situation Eq. 4.2.6 becomes

$$0 = (x_a - 2)\xi_c(0;\gamma) - x_a\xi_c(0;\gamma + \Xi) - \left\{ 2\sum_{p=1}^{q} (-1)^p \xi_c\left(t^{(p)};\gamma\right) \right\} \quad 4.2.7$$

Using the definition and the symmetry of ξ_c, Eq. 4.2.7 can be expanded to give

$$0 = x_a - 2 - x_a \exp(\mathrm{i}m\Xi) - \left\{ 2\sum_{p=1}^{q} (-1)^p \exp\left(\mathrm{i}m\omega_r t^{(p)}\right) \right\} \quad 4.2.8$$

with $m = \pm 1$ and $m = \pm 2$. Therefore, high amplification factors x_a can be achieved by constraining π-pulses with p even to coincide with a rotor echo. Setting $q = x_a - 1$ resulting in timings for π pulses of the form

$$t^{(p)} = \begin{cases} \left(k^{(p)} - \frac{\Xi}{2\pi}\right)\tau_r & p \in \text{odd} \\ k^{(p)}\tau_r & p \in \text{even} \end{cases} \quad 4.2.9$$

For realizable sequences, $t^{(p)} < T$ and $t^{(p)} < t^{(p+1)}$ for all p, and τ_{seq} = 0, so that the end of the sequence coincides with a spin echo and phase shifts for different sites are avoided. In addition, the sequences must have T independent of Ξ, otherwise differential transverse relaxation will cause distortions of the ω_1 sideband amplitudes. Considering these requirements, it is not easy to find timings which can be varied to provide a continuous variation of Ξ.

Pulse sequences have been considered with timings defined by

$$k^{(p)} = \begin{cases} p+1 & p \in \text{odd} \ \text{ and } \frac{p}{q+1} < \frac{\Xi}{2\pi} \\ p & \text{otherwise} \end{cases} \quad 4.2.10$$

For given q only a restricted set of Ξ values give sequences which have τ_{seq} = 0. In turn, only a small number of subsets have constant duration T, and so fulfill all the conditions required for useful CSA amplification sequences. One subset gives $(q+1)/2$ values of Ξ equally spaced between 0 to $2\pi(q-1)/(q+1)$ with a spin echo at a constant time $T=(q+1)\tau_r$ and an amplification factor $x_a = q+1$. The timings for the 8 sequences of 15 π pulses which result in 8 values of Ξ/2π between 0 and 7/8 and an amplification factor of 16 are shown in Figure 4.1.

4.3 Experimental Set Up

The pulse sequence of Figure 4.1 was used to obtain carbon-13 CSA amplification spectra with q = 23 or 47, resulting in amplification factors x_a = 24 or 48, respectively. Comparing to our recently version [59], modifications were made to this experiment which have considerably improved its applicability. Enhanced carbon-13 transverse magnetization generated by cross-polarization evolves under a sequence of q π-pulses, before the FID is recorded as a function of t_2. The timings of the π pulses are varied and result in an amplification factor of $x_a = q+1$. Sensitivity is maximized by eliminating the need to store the magnetization along the z-axis for t_1. Since the total number of π-pulses is only $q = x_a - 1$, the sequences are more efficient in terms of number of π-pulses and the total duration comparable to a modification due to Orr *et al*. [62].

All pulses on the carbon-13 channel, including the contact pulse, were phase cycled using the Cogwheel procedure. For experiments with q = 23 a 47-step cycle is required which can be written COG47(-24,-23,-24,-23,-24,-23,-24,-23,-24,-23,-24,-

23,-24,-23,-24,-23,-24,-23,-24,-23,-24,-23,-24,-23;0,0) in the notation of Ref. Combination with a conventional phase alternation of the initial proton $\pi/2$-pulse concurrently with the receiver results in a manageable $2(2q + 1)$-step overall phase cycle.

In common with original CSA amplification experiments, the two-dimensional spectrum is obtained by a straightforward double complex Fourier transformation with respect to Ξ and t_2, after weighting in the detection dimension only. The processing procedure and further details of can be found in Chapter 3.

4.4 Results and Discussion

Demonstration on Vinyl phosphonate Nucleotide

The interactions of proteins and small molecules with nucleic acids have long been a subject of extensive study. In light of the biological importance of nucleic acids, a wide array of biochemical, biophysical and spectroscopic techniques have been used to pursue an atomic level understanding of molecular recognition, binding and structural alterations associated with complex formation. Solid-state NMR is widely used to study the structure of biomolecules that are not easily crystallized or dissolved, and thus cannot be conveniently studied by X-ray crystallography and solution-state NMR, respectively [81-86]. Recently, there has been a marked increase in the number of structural studies of proteins using solid-state NMR, but so far similar measurements on DNA and RNA have proved problematic. In the main this is because of relative lack of shift resolution in the carbon-13 magic angle spinning (MAS)

spectra of the component nucleotides which mean that structural features are difficult to analyze using solid-state NMR.

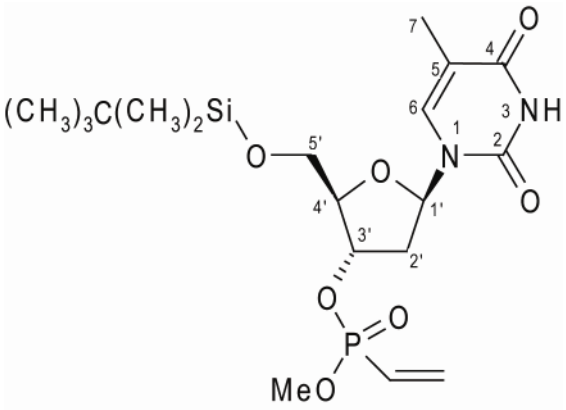

Figure 4.2: The structure of the vinyl phosphonate modified nucleotide.

In this chapter we demonstrate the effectiveness of the CSA amplification experiment in a study of the vinyl phosphonate modified nucleotide shown in Figure 4.2. The carbon–13 CPMAS spectra of the vinyl phosphonate nucleotide with a MAS rate of 10 kHz together with a comparison between XiX decoupling and CW decoupling is shown in Figure 4.3. For comparison, the two experiments were recorded at the same spinning speed and same proton decoupling power. Other experimental parameters are given in the figure caption. It is apparent that XiX decoupling gives higher peak height and a corresponding narrower linewidth compared with CW decoupling. Note that the resolution for the carbonyl groups (i.e. C2 and C4) become more pronounced than that for CH and CH_2 groups of the vinyl phosphonate modified nucleotide.

Using XiX decoupling the majority of the carbon–13 resonances are resolved and the peak assignments are based on a comparison with solution NMR spectra [87]. For the *t*-butyl group the isotropic chemical shifts are the same due to the fast rotation. The sugar carbons exhibit relatively narrow lines, except for C2' and C5'. The wider

peaks observed for these two CH_2 resonances can most likely be attributed to insufficient proton decoupling. The carbon atom C2', C4', MeO and CH= exhibits two lines due to the phosphorus coupling. The resonances of C2, C4 and C5 are doublets, indicating that there are two optical isomers in a unit cell as expected due to the chiral centres in the molecule.

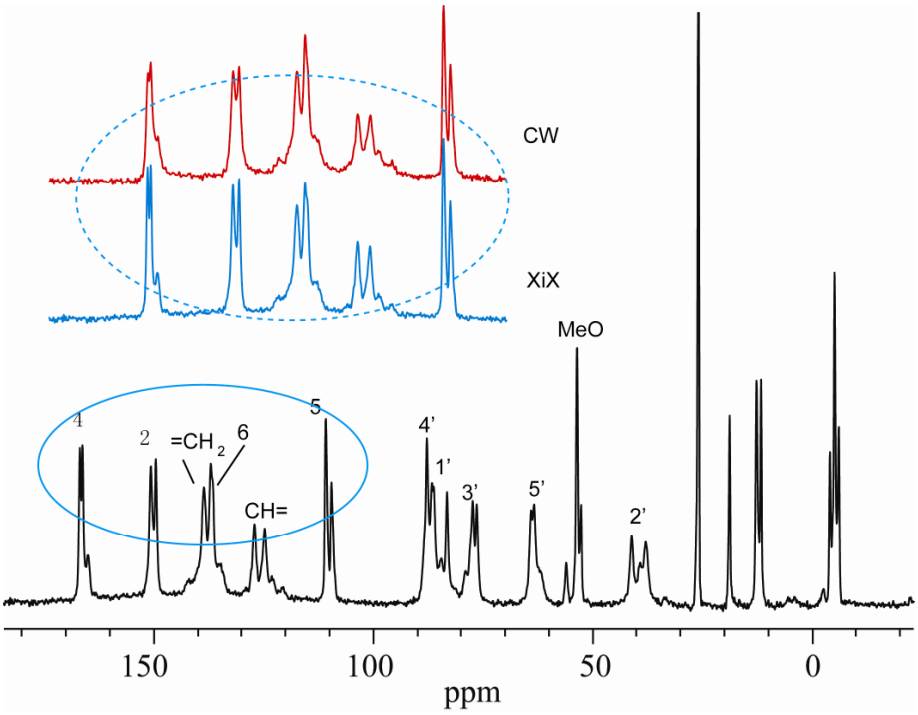

Figure 4.3: Carbon–13 MAS spectrum of the vinyl phosphonate modified nucleotide recorded at a rate of 10 kHz using a 4mm MAS probe and a standard cross-polarization pulse sequence with a contact time of 3 ms. The MAS rate was stabilized to ±5 Hz. Proton decoupling with a field strength of 100 kHz was applied throughout the acquisition period. The spectral width was 50 kHz and 3200 scans were acquired. The various carbon resonances are assigned according to the literature [87].

Efficient heteronuclear decoupling during the sequences of π pulses is essential to optimize the sensitivity of the CSA amplification experiment. Therefore, a

number of different decoupling schemes were tested using original CSA amplification experiment:

- CW decoupling was applied during the sequences of π pulses and during detection, but decoupling was interrupted during carbon-13 pulses.(Figure 4.4a)
- XiX decoupling was applied during sequences of π pulses and during detection period, but decoupling was interrupted during the carbon-13 pulses.(Figure 4.4b)
- XiX decoupling is continuously applied during the pulse sequences and the detection period. (Figure 4.4c)

Figure 4.4 shows the two-dimensional spectrum of the vinyl phosphonate modified nucleotide using the original CSA amplification experiment with (a) CW decoupling and (b, c) XiX decoupling (the second and third scheme). For XiX decoupling, $t_p = 2.85\ t_r$ was used. Further experimental details are given in the figure caption. Most of the peak intensities are higher at XiX decoupling compared with CW decoupling. The intensities of the carbon C2, C4 and C5 increased over 20% at XiX decoupling compared with CW decoupling. Furthermore, the signal-to-noise was improved as well. The third scheme is simpler to implement and so this was chosen for the CSA amplification experiments described here. In this thesis, XiX decoupling was used in CSA amplification when MAS rates no less than 10 kHz. The length of π-pulse was also tested in the following way.

Figure 4.5 shows the part of the centerband of the spectra of the vinyl phosphonate modified nucleotide recorded using the original CSA experiment with XiX decoupling at a MAS rate of 10 kHz and reduction factor of 8. The π-pulse was (a)

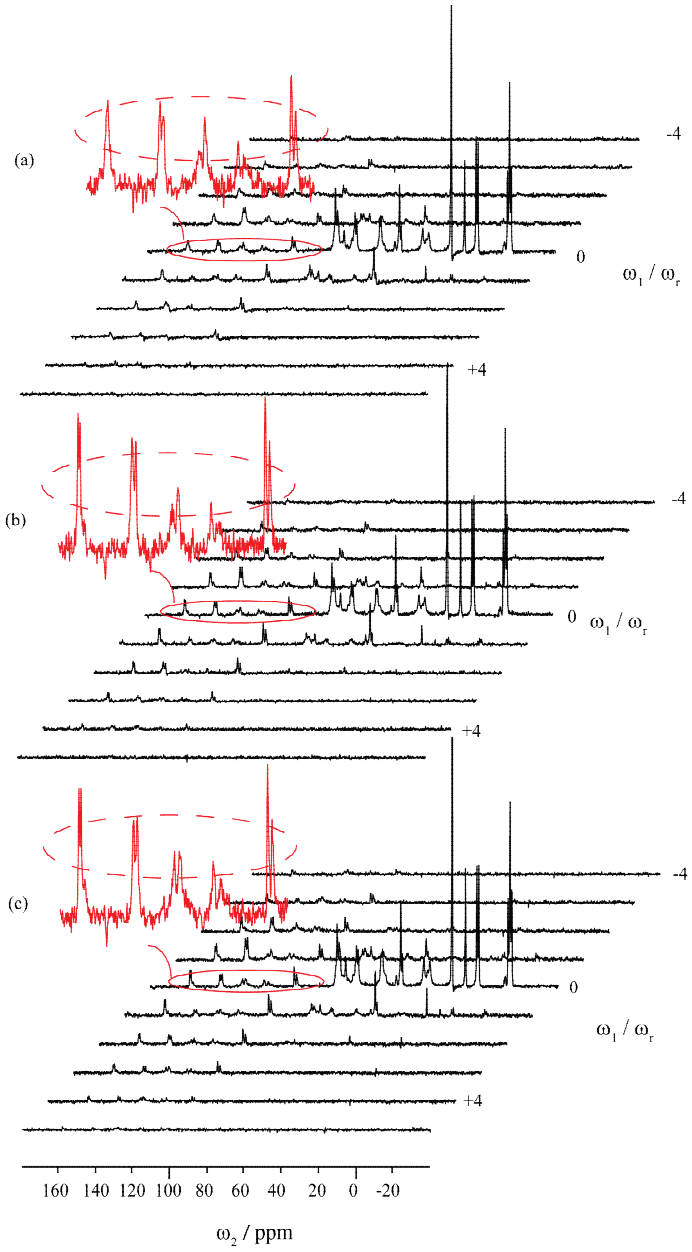

Figure 4.4: Regions of two-dimensional spectra of the vinyl phosphonate modified nucleotide recorded using the original CSA amplification experiment with different decoupling schemes (see in text) at a rate of 10 kHz using a 4mm MAS probe and a standard cross-polarization pulse sequence with a contact time of 3 ms. The MAS rate was stabilized to ±5 Hz. Proton decoupling with a field strength of 100 kHz was applied throughout the acquisition period. The spectral width was 50 kHz and 1408 scans were acquired. The amplification factor was 8, resulting in an effective MAS rate of 1250 Hz.

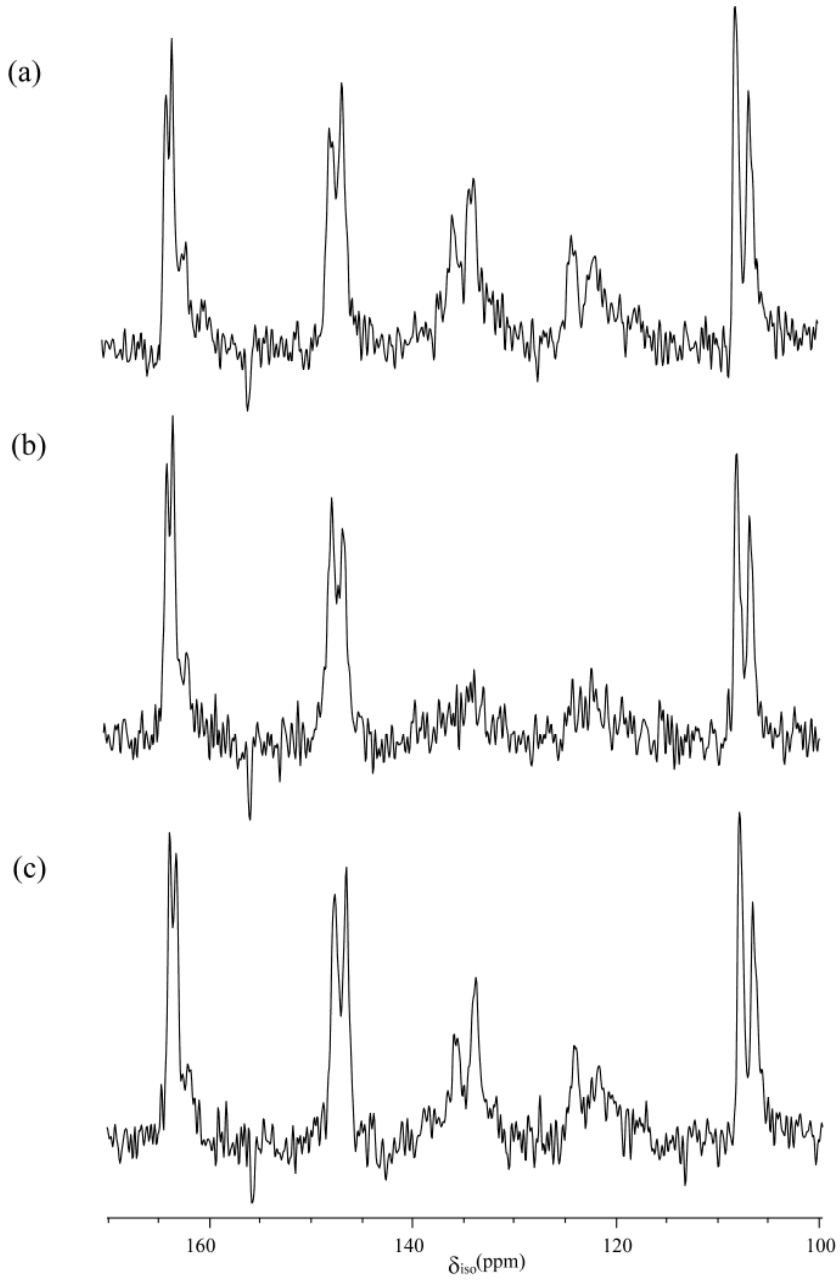

Figure 4.5: Part of the centerband of the original CSA amplification with XiX decoupling of sample vinyl phosphonate nucleotide recorded at a rate of 10 kHz using 4mm MAS probe and a standard cross polarization pulse sequence with a contact time 3 ms. Proton decoupling was with a field of 83.3 kHz and 1408 scans were acquired. The carbon-13 π-pulse lengths were (a) 11 μs, (b) 5 μs and (c) 3.22 μs.

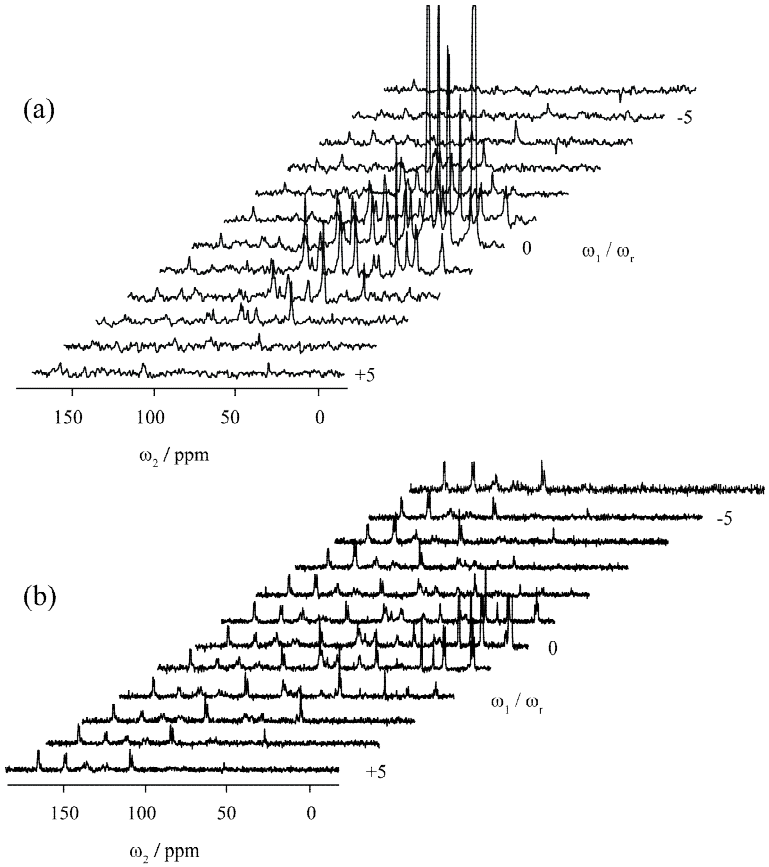

Figure 4.6: Part of CSA amplification spectra of the vinyl phosphonate modified nucleotide recorded using (a) the original pulse sequence (CW decoupling) with an amplification factor 8 and an MAS rate of 4 kHz, resulting in an effective MAS rate in ω_1 of 500 Hz. The carbon-13 Larmor frequency was 75.46 MHz and the contact time was 3ms. There were 32 t_1 values in total with an increment of 7.81 μs, according to 1/32 of the MAS period. Only the central 12 lines are shown. (b) the modified sequence with an amplification factor 24 and a MAS rate of 12 kHz, resulting in an effective MAS rate in ω_1 of 500 Hz. The MAS rate was stabilized to ±5 Hz, and the contact time was 3 ms. The proton decoupling field was approximately 85 kHz, and carbon-13 π-pulses were 3.24 μs in duration. The spectral width in ω_2 was 50 kHz and the acquisition time was 40.9 ms. The relaxation delay was 5 s, and there were 1316 scans for each of the 12 sequences required. For XiX decoupling, $t_p = 2.85\ t_r$ was used.

11μs, (b) 5μs and (c) 3.22 μs. For XiX decoupling, t_p was carefully adjusted as $1.9 \times t_r$. Other experimental parameters are given in the figure caption. In order to avoid the unwanted Hartmann-Hahn conditions where the decoupling is compromised (Figure 4.5b), shorter π-pulses were used to obtain the modified CSA amplification experiments.

Figure 4.6(a) shows the two-dimensional spectrum of the vinyl phosphonate modified nucleotide using the original CSA amplification experiment with an effective MAS rate of 500 Hz in the ω_1 dimension. Figure 4.6(b) shows the carbon-13 CSA amplification spectrum of the vinyl phosphonate modified nucleotide with an amplification factor of 24 recorded at Larmor frequency of 75.47 MHz and a MAS rate of 12 kHz. For XiX decoupling, $t_p = 2.85\ t_r$ was used. Further experimental details are given in the figure caption. The two-dimensional spectrum is obtained using MatNMR [88] for Spinsight which is limited to a Fourier transform data size of 2^N. Only isotropic shifts remain in the ω_2 dimension due to the relatively high MAS rates used here. Problems arising from overlap of ω_2 sidebands from different chemical sites are minimized. The sideband intensities extracted from these two experiments are compared in Figure 4.6. Note that at the spinning rate of 12 kHz, the original sequence produces a spectrum (data not shown) which contains the optimum number of sidebands for analysis for the sp^2 hybridized carbon sites. However, the modified sequence results in an effective MAS rate in ω_1 which is low enough that sufficient sidebands from sp^3 hybridized carbon sites are observed (Figure 4.6b).

Experimental application of the modified sequence to achieve an amplification factor of 48 is demonstrated for the vinyl phosphonate modified nucleotide. The spinning rate of 12 kHz and effective spinning rate of $\omega_r / x_a = 250$ Hz was used to

measure the chemical shift anisotropy of the carbon sites with small anisotropy values. The sideband intensities extracted from this experiment are compared with those obtained from the original CSA amplification (in Figure 4.7). The good agreement between the sideband intensities demonstrates that the modified CSA amplification experiment functions correctly even up to an amplification factor of $x_a = 48$.

As a further demonstration, Figure 4.8 shows the values of the chemical shift anisotropy of five sites extracted from the original and modified CSA amplification experiment. To accurately estimate CSA parameters from sideband intensities, simulated spectra calculated using the SIMPSON program were performed by minimising the root mean square difference between the experimental and simulated data. The values quoted here were obtained using 31 (α, β) crystallite orientations distributed according to the Lebedev scheme [77]. 40 γ angles were used according to the gcompute method in SIMPSON. The values of shift anisotropy obtained from the original and the modified CSA amplification experiments are in good agreement. Therefore, this modified sequence provides a new way to measure small shift anisotropies without using slow MAS rates.

Figures 4.9 shows contour plots of χ^2, as a function of the anisotropy and asymmetry parameters for all resolved carbon sites of the vinyl phosphonate modified nucleotide. Error analysis was carried out using SIMPSON combined with MINUIT optimization package. The contours were plotted using MATLAB software. The boundaries of the 68.3% joint confidence region (blue lines) and 95.4% joint confidence region (brown lines) for the two parameters are shown. The largest joint confidence region was obtained for sites which are bonded to double bond (C6, CH=

and CH_2=). The 68.3% confidence limits on the individual parameters ζ and η for all the carbon sites are within ±3ppm and ±0.17, respectively.

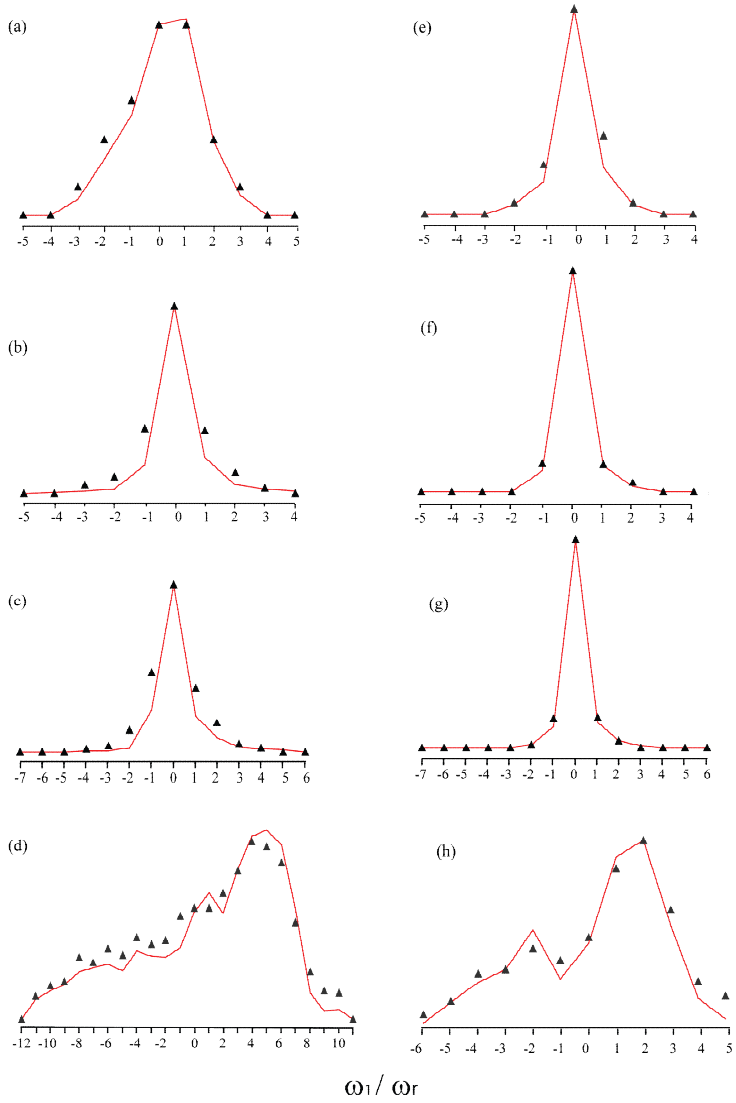

Figure 4.7: Sideband intensities (red line) extracted from the original CSA amplification sequence with an effective MAS of (a, b, c, d) 250 Hz and (e, f, g, h) 500 Hz, compared with those obtained from the modified sequence with an amplification factor of 48 (a, b, c, d) and 24 (e, f, g, h) and a MAS rate of 12 kHz, resulting in effective MAS rate in ω_1 of 250 Hz (triangle) in right hand column and 500 Hz in left hand column. Each row represents the same carbon site (from the top: base-CH_3, TBS-C, TBS-$(CH_3)_3$ and OCH_3.)

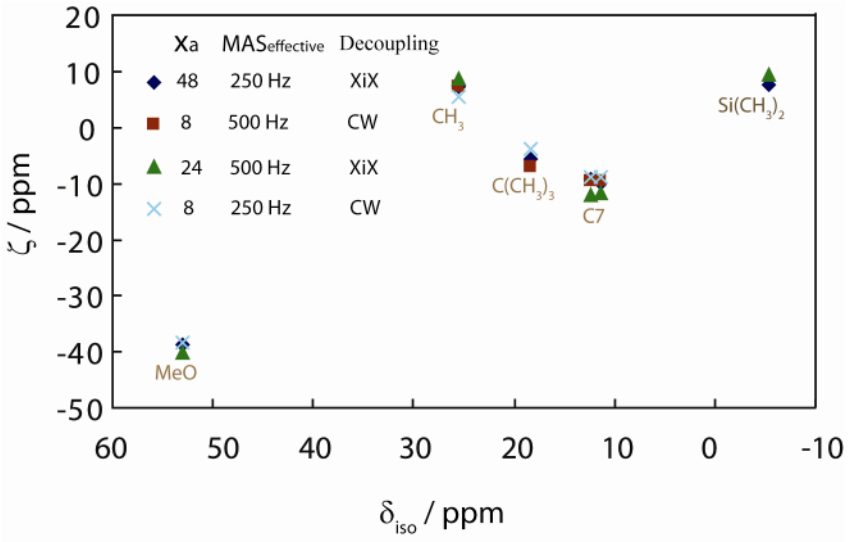

Figure 4.8: Comparison of the chemical shift anisotropy obtained from: the modified CSA amplification spectra recorded at a MAS rate of 12 kHz with the amplification factor 48 (diamond) and 24 (triangle); and the original CSA amplification spectra recorded with an amplification factor 8 and MAS rate 2 kHz (cross) and 4 kHz (square).

The principal components are shown in Table 4.1 calculated from the mean values (based on the 68.3% confidence limit) of anisotropy and asymmetry parameters.

Using a combination of the original and modified CSA amplification experiments with a range of MAS rates and amplification factors all the CSA tensors of the vinyl phosphonate modified nucleotide have been measured. The principal components of each shift tensor are given in Table 4.1. The values of shift anisotropy and asymmetry from CSA amplification experiments are shown in Figure 4.10. Many of the chemical shift anisotropies are quite close for the two optical isomers. For carbon sites C2', C4' and OMe, the shift anisotropy and asymmetry are different for the two optical isomers. Note that the lines have not been assigned to the individual isomers.

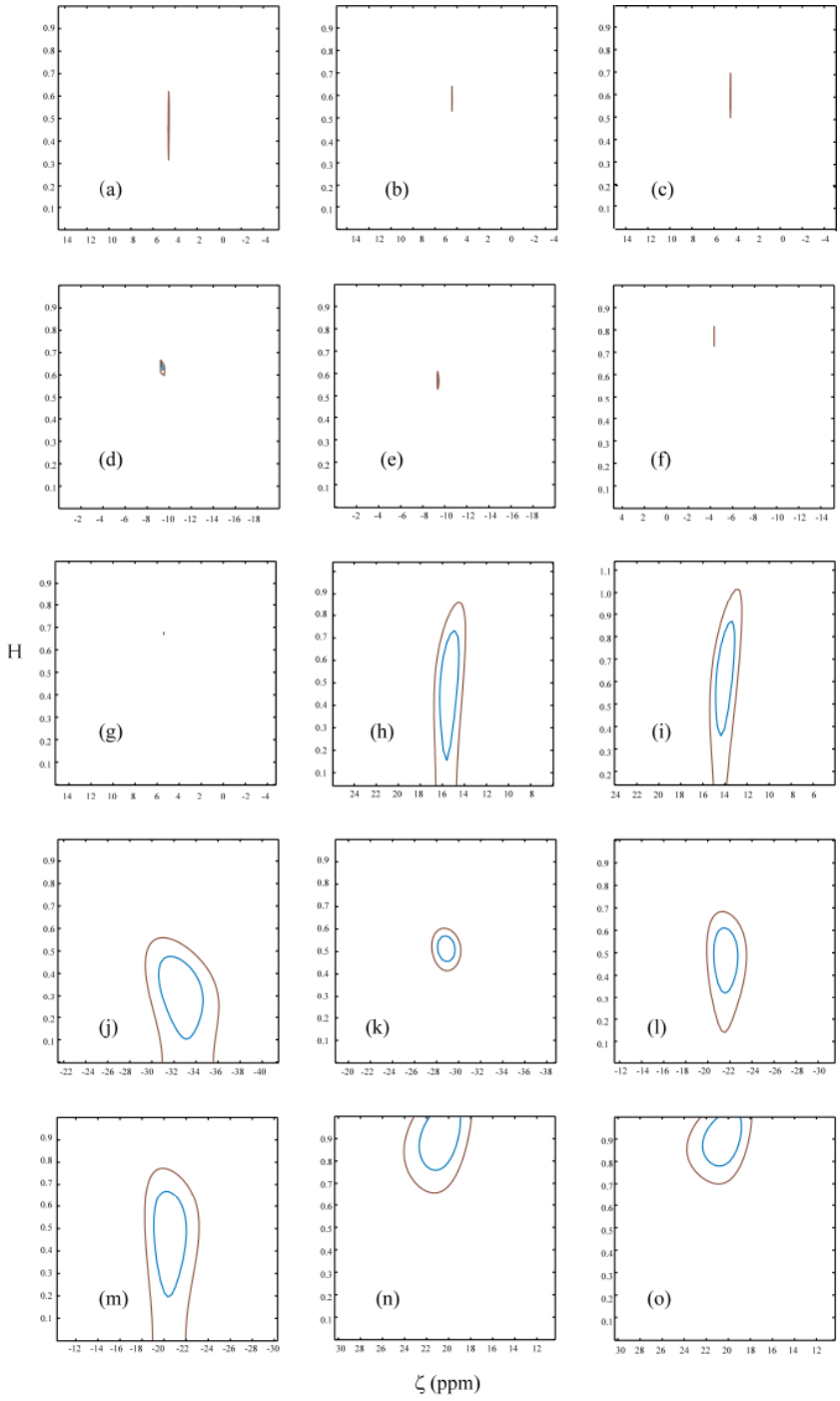

Figure 4.9A: χ^2 statistic as a function of the CSA parameters ζ and η of the vinyl phosphonate modified nucleotide . Graphs for the carbon sites are presented: (a-c) TBS-Si-CH_3, (d, e) Base-CH_3, (f) TBS-C, (g) TBS-CH_3(3), (h, i) C2', and (j, k) OCH_3, (l, m) C5', (n, o) C3'. The 68.3% joint confidence limit (blue) and 95.4% joint confidence limit (brown) for the two CSA parameters are shown.

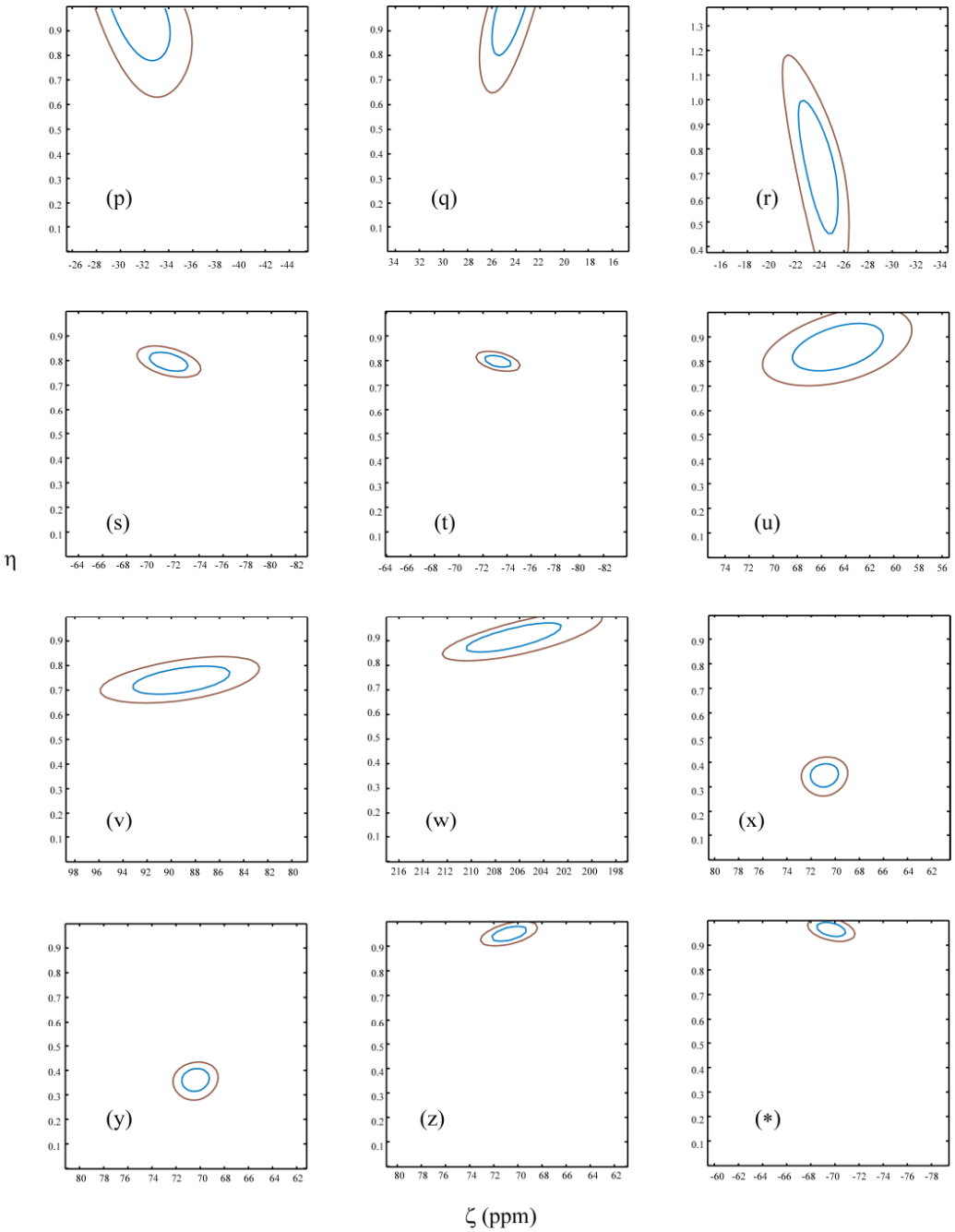

Figure 4.9B: χ^2 statistic as a function of the CSA parameters ζ and η of the vinyl phosphonate modified nucleotide . Graphs for the carbon sites are presented: (p) C1', (q, r) C4', (s, t) C5, (u) CH=, (v) C6, and (w) CH_2=, (x, y) C2, (z,*) C4. The 68.3% joint confidence limit (blue) and 95.4% joint confidence limit (brown) for the two CSA parameters are shown

Table 4.1 CSA amplification measurements of principal components of shift tensors in the vinyl phosphonate modified nucleotide

Carbon[a]	δ_{iso}(ppm)	δ_{xx}[b](ppm)	δ_{yy} (ppm)	δ_{zz} (ppm)
TBS-Si-	–5.8	–9.1	–7	–1.3
CH_3(2)	–4.9	–7.8	–5.8	–1.1
	–3.8	–7.2	–4.8	0.6
Base-CH_3	11.9	19.4	13.7	2.6
	12.9	20.2	15.0	3.5
TBS-C	19.0	22.7	19.5	14.8
TBS-CH_3(3)	26.1	21.0	26.1	31.2
C2'	38.2	26.6	34.4	53.6
	41.3	30.7	37.9	55.3
OCH_3	52.9	74.6	63.8	20.3
	53.8	74.0	62.5	24.9
C5'	63.5	79.8	68.8	41.9
	64.3	79.7	69.4	43.8
C3'	76.6	97.3	76.6	55.9
	77.4	97.9	77.4	56.9
C1'	83.3	114.6	83.3	52.0
C4'	86.8	110.9	86.4	63.1
	87.9	108.8	91.0	63.9
C5	109.6	173.5	117.1	38.2
	110.9	176.4	118.6	37.7
CH=	124.9	65.1	120.1	189.5
C6	137.0	60.8	124.1	226.1
CH_2=	138.7	345.4	134.6	–63.9
C2	149.5	101.6	126.5	220.4
	150.7	102.5	128.5	221.1
C4	166.4	236.6	166.4	96.2
	166.9	235.2	168.3	97.2

a. sites are assigned according to Ref. [87].

b. assigned according to $|\delta_{yy} - \delta_{iso}| < |\delta_{xx} - \delta_{iso}| < |\delta_{zz} - \delta_{iso}|$.

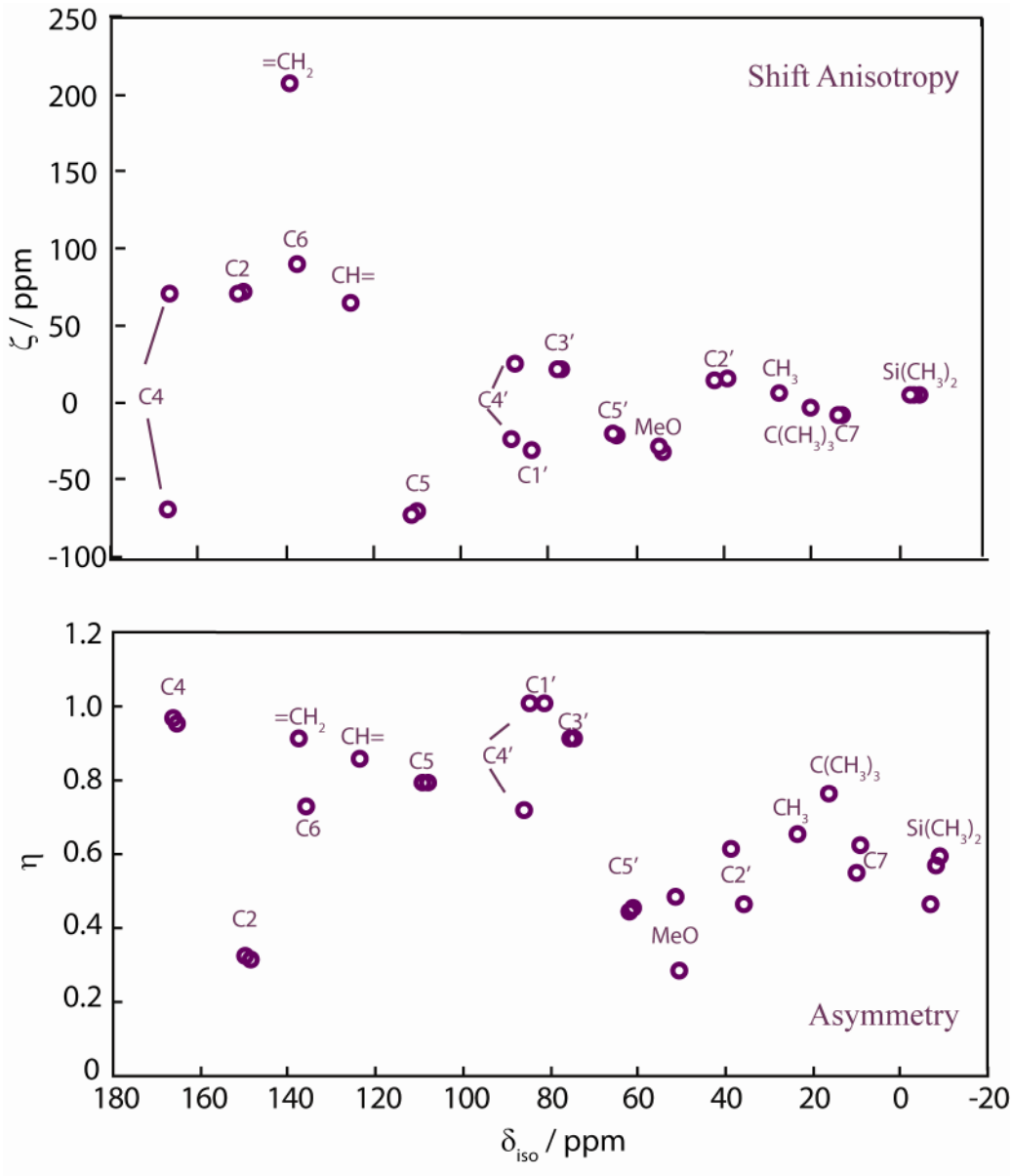

Figure 4.10: Values of shift anisotropy (ζ) and asymmetry (η) of the vinyl phosphonate modified nucleotide extracted from the original and modified CSA amplification experiments.

4.5 Conclusions

In summary, first, the original CSA amplification experiment was improved by using XiX decoupling schemes at modern MAS rates. Second, the modified CSA amplification experiment which results in large amplification factors up to 48 was demonstrated on the the vinyl phosphonate modified nucleotide. High resolution of isotropic shifts resulting from the use of XiX decoupling in ω_2 ensures that both the resolution of different stereoisomers and the overall sensitivity of the experiment are optimal. For most sites (small) differences between the CSA tensors for each stereoisomer have been observed.

Chapter 5

Applications of CSA Amplification Experiment to Nucleosides

5.1 Introduction

Nucleosides are glycosylamines consisting of a nucleobase (often referred to simply as a *base*) bound to a ribose or deoxyribose sugar. Nucleosides can be phosphorylated by specific kinases in the cell on the sugar's primary alcohol group (-CH_2OH), producing nucleotides, which are the molecular building blocks of DNA and RNA. Solid-state NMR is a valuable tool for structural studies of nucleosides, since it allows acquisition of spectra corresponding to a single molecular conformation in contrast to the average observed with solution-state NMR. The CSA tensor has the potential to provide a more detailed picture of the local environment and hence the molecular conformation than the isotropic shift alone. Ying and co-workers [89] have measured carbon-13 CSA tensors for double-helical RNA and DNA oligomers. Grant and co-workers [90] have measured carbon-13 CSA tensors for some nucleosides and compared these with calculations. In this work the carbon-13 chemical shift tensors for adenosine, 2'-deoxythymidine, uridine, cytidine, guanosine and 5-methyluridine

(see Figure 5.1) were measured using the CSA amplification experiment and compared with first-principles calculations.

5.2 Experimental

5.2.1 Materials

Adenosine (≥99%), 2'-deoxythymidine (>99%), uridine (≥99%), cytidine (≥99%), guanosine (≥98%) and 5-methyluridine (97%) were purchased from

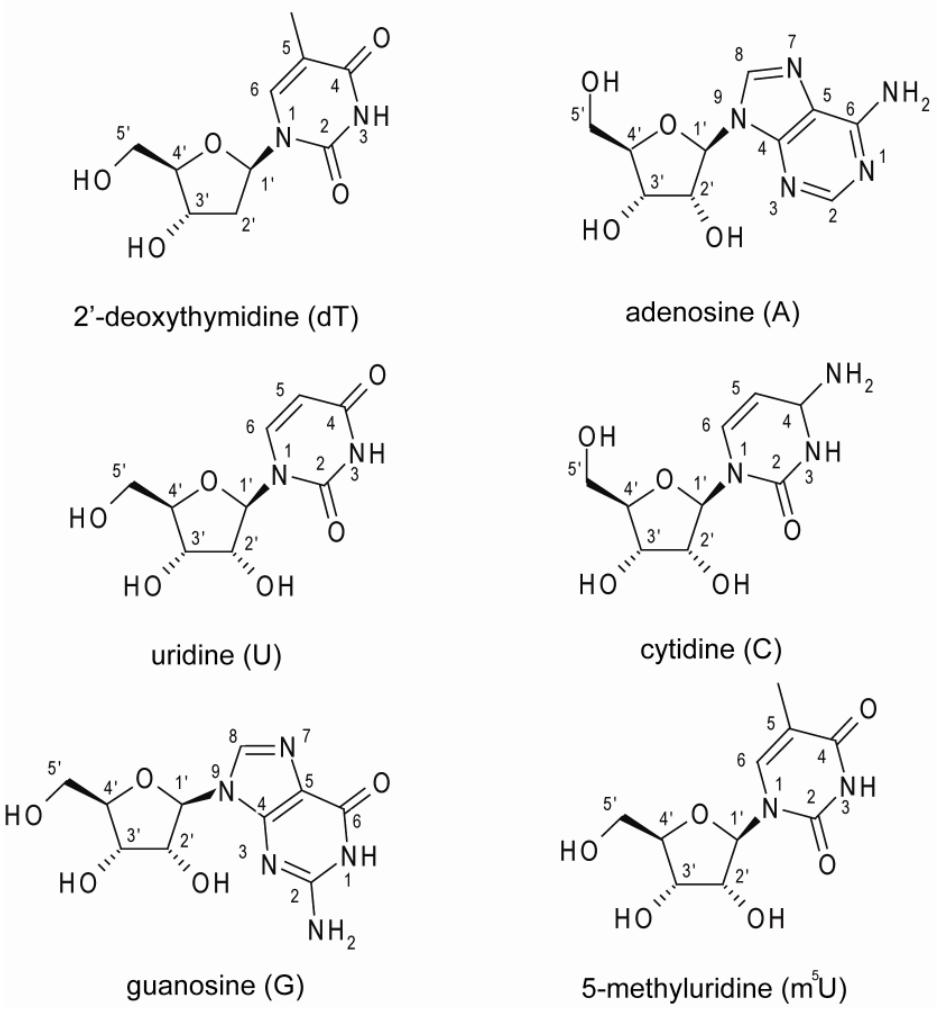

Figure 5.1: The structures of 2'-deoxythymidine, adenosine, uridine, cytidine, guanosine, and 5-methyluridine with atom numbering.

Sigma-Aldrich. Their chemical structures are shown in Figure 5.1. Samples of adenosine, 2'-deoxythymidine, cytidine, and uridine were used in NMR experiments without further purification. Guanosine was prepared by keeping the sample in a desiccator for three months, immersed in a saturated water vapor atmosphere [90]. 5-methyluridine was recrystallized from aqueous ethanol [91] and the crystal structure was determined by X-ray diffraction.

5.2.2 X-ray diffraction (XRD)

The crystal structure of 5-methyluridine (see Figure 5.2) was confirmed by single-crystal X-ray diffraction. The XPD pattern was collected using a Bruker SMART1000 CCD area detector diffractometer. The structure was solved by direct methods, and full-matrix least-squares refinements on F^2 were carried out. Other parameters and the data can be found in Appendix II.

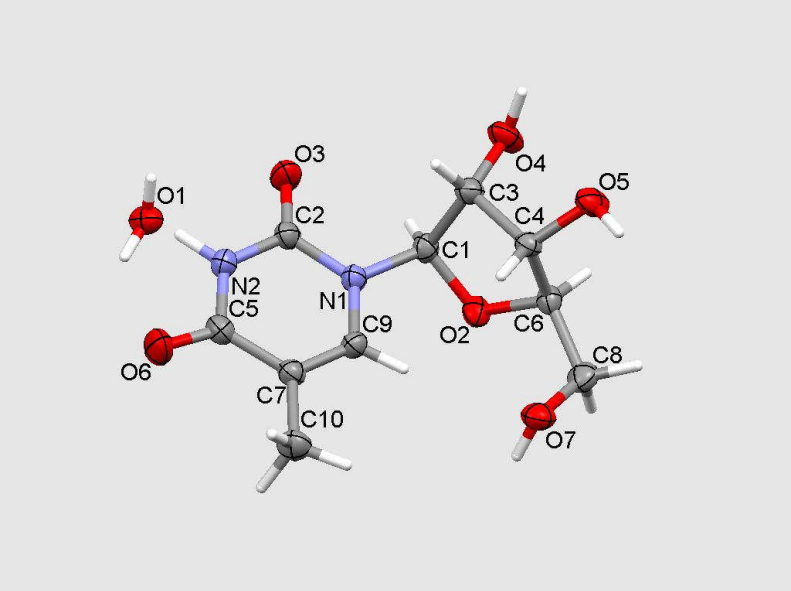

Figure 5.2: The chemical structure of a single molecule of 5-methyluridine determined by X-ray. In the crystalline form there is one molecule per unit cell.

5.2.3 NMR Experiments and Computation

Carbon-13 NMR spectra were recorded at a Larmor frequency of 75.46 MHz on samples of 2'-deoxythymidine, adenosine, cytidine, guanosine and uridine packed into 4 mm rotors spinning in a double resonance MAS probe. CPMAS spectra were recorded by co-adding between 8 and 64 scans with a spectral width of 50 kHz. The MAS rate was 10 kHz, stabilized to ± 5 Hz. Proton decoupling (XiX) with a field strength of 85 kHz was applied during the acquisition time. For 5-methyluridine, the CPMAS spectrum was recorded at a MAS rate of 6 kHz using a 7 mm rotor spinning in a double-resonance MAS probe. The contact time and the relaxation delay were optimized for each sample and ranged between 2 and 4 ms and 3 to 180 s, respectively. All carbon-13 chemical shifts were externally referenced indirectly to TMS via the high-frequency carbon-13 line was assigned a shift of 37.8 ppm. The carbon-13 chemical shift tensors were extracted from the spinning sideband intensities measured from CSA amplification spectra or one-dimensional spectra recorded with a low MAS rate. The spin-lattice relaxation times were long for all the nucleosides except guanosine and uridine. Nonetheless, good signal-to-noise could be obtained within reasonable acquisition times.

Dr. Jonathan Yates and Mikhail Kibalchenko calculated CSA tensors of these six nucleosides based on crystal structures [91-96] as shown in Tables 5.7 to 5.12. Calculations were carried out using the planewave-pseudopotential formalism of density functional theory, as implemented in the CASTEP code [97]. Magnetic shielding tensors were calculated for each nucleoside structure using the recently developed GIPAW [98] approach. All calculations used ultrasoft pseudopotentials [99]

and a maximum plane-wave energy of 800 eV. The Brillouin zone was sampled using a Monkhorst-Pack [100] grid with a maximum spacing of 0.055 $Å^{-1}$. These calculation parameters were chosen to converge the isotropic chemical shifts to within 0.1 ppm. Except where explicitly stated all calculations used the PBE [101] exchange-correlation functional.

For accurate calculation of NMR parameters the quality of the input crystal structure is paramount. Starting crystal structures for the nucleosides [91-96] were taken from the Chemical Database Service [102]. The structure for adenosine was [103] was obtained by neutron diffraction. For this structure the calculated average force over all atoms was 0.3 eV / Å, with a maximum force on a hydrogen atom of 0.7 eV /Å. For this reason the NMR parameters were computed using diffraction structure without further optimization. The structure of 2'-deoxythymidine [104], uridine [105], cytidine [106], guanosine [107], and 5-methymidine [108] had been determined by X-ray diffraction. Structures obtained by X-ray diffraction are usually less accurate than neutron derived structures; in particular the positions of hydrogen atoms are poorly defined. It is not surprising that using the experimental structures for these systems lead to forces in the order of 10 eV / Å on the hydrogen atoms. However, after a partial geometry optimization the maximum force in four of five structures was below 1 eV / Å, and so these partially relaxed structures were used to compute the NMR parameters. The exception was 5-methyluridine in which after partial optimization had forces which exceeded 3 eV / Å. For this reason the NMR parameters for 5-methyluridine were computed using a structure in which all atomic positions had been optimized. Note that all geometry optimizations keep the unit cell parameters fixed to

their experimental values. Checks were carried out to make sure that full geometry optimization did not change any site assignments when compared to the experiment.

Electronic structure calculations report the magnetic shielding tensor σ which is defined as the ratio of the induced $\mathbf{B}_{in}$ and applied $\mathbf{B}_0$ magnetic fields,

$$\sigma = -\frac{\mathbf{B}_{in}}{\mathbf{B}_0} \qquad 5.3.1$$

For each crystal structure the isotropic shielding σ_{iso} was calculated as in Eq. 5.3.2 where σ_{ii} are the components from the diagonalized symmetric part of the magnetic shielding tensor.

$$\sigma_{iso} = \frac{1}{3}\left(\sigma_{xx} + \sigma_{yy} + \sigma_{zz}\right) \qquad 5.3.2$$

The isotropic chemical shift δ_{iso} is defined relative to a reference shielding σ_{ref} such that

$$\delta_{iso} = -(\sigma_{iso} - \sigma_{ref}) \qquad 5.3.3$$

The principal components of the chemical shift tensor were calculated from those of the shielding tensor in a similar fashion.

For carbon-13 we optimized σ_{ref} to each nucleoside to provide best comparison with experiment. The value for σ_{ref} ranged from 167.1 to 170.5 ppm. In a previous combined experiment and computational study of the NMR chemical shift tensors in disaccharides it was found that the magnitude of the computed anisotropy was consistently too large. It was noted that simply scaling the calculated tensor width facilitiated the comparison to experiment. The tensor width, or span Ω, is defined as

$$\Omega = \delta_{zz} - \delta_{xx} = \zeta + \frac{\zeta\left(1+\eta\right)}{2} \qquad 5.3.4$$

The values of the isotropic shift and the asymmetry were not adjusted during this scaling procedure.

5.3 Results and Discussion

5.3.1 CPMAS Spectra and Carbon-13 Isotropic Shifts

Figure 5.3 shows the carbon-13 CPMAS spectrum of (a) 2'-deoxythymidine, (b) adenosine, (c) cytidine and (d) uridine. The isotropic chemical shifts for sites in the sugar rings and in the nucleic acid bases are generally well separated from one another. Most of the peak positions are in excellent agreement with those observed by Stueber *et al*. [90]. The Stueber *et al.* study found a difference of 0.4 ppm between carbon atoms C6 and C2 in adenosine, but these peaks are not resolved in this work. For uridine, the spectrum in Figure 3(d) shows twice the expected number of peaks, indicating that there are two molecules per asymmetric cell. The resonances were assigned by comparison with calculated values (see below).

The carbon-13 CPMAS spectrum of the as purchased guanosine sample is shown in Figure 5.4(a).The broad peaks and the fine structure indicate an anhydrous state [109]. Figure 5.4(b) shows the spectrum of guanosine dihydrate prepared as described above in which the lines are substantially less broad. The peaks of carbon sites (C5, C8, C2’ and C3’) exhibit a small splitting, suggesting the presence of two molecules in an asymmetric unit cell. For guanosine dihydrate, Stueber *et al*. assignedthe resonance at 151.4 ppm to the C2 site and the resonance at 152.1 to the C4 site. These assignments are based on a comparison with calculated values obtained

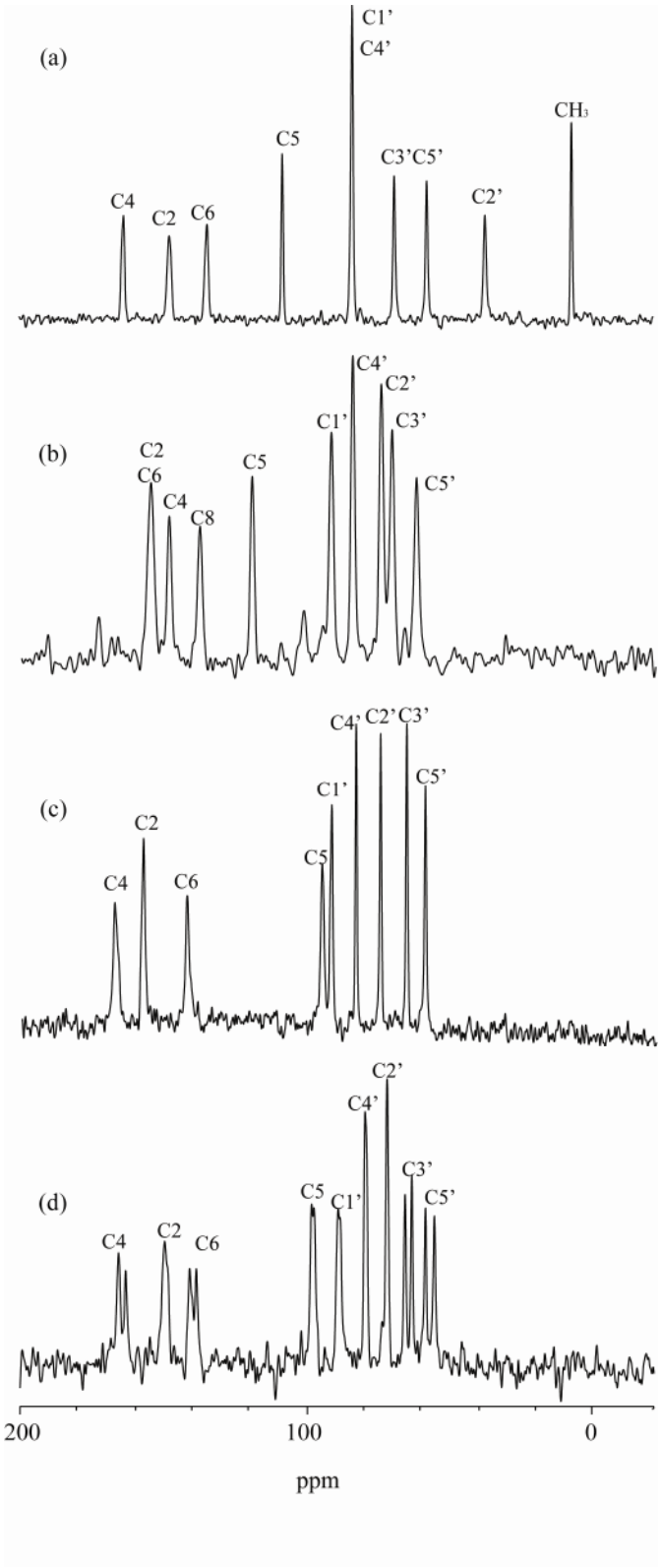

Figure 5.3: Part of carbon-13 CPMAS spectra of (a) 2'-deoxythymidine, (b) adenosine, (c) cytidine and (d) uridine recorded using parameters described in the text.

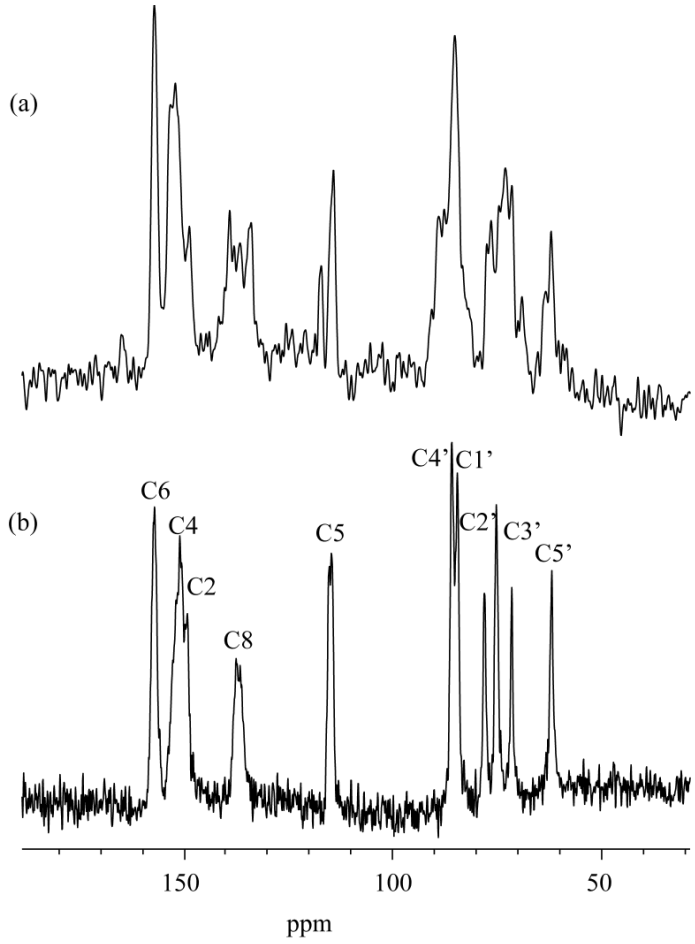

Figure 5.4: Part of carbon-13 CPMAS spectra of guanosine in (a) a nonstoichiometric state of hydration and (b) the dehydrated state. The spectra were recorded at a MAS rate of 10 kHz using proton decoupling with a field of 100 kHz. The spectral width was 50 kHz. The relaxation delay was 5 s and 128 (a) and 1024 (b) scans were acquired.

using EIM and reported by Sugawara *et al*. [109]. However, some of these assignments maybe challenged, since the shift differences are small. The calculated CSA values in Table 5.10 are consistent with a reversed assignment of C2 and C4 in the case of guanosine dihydrate.

Figure 5.5(a) shows the carbon-13 CPMAS spectrum of as purchased 5-methyluridine recorded at a MAS rate of 6 kHz. In this case the majority of the lines split into two components, suggesting that there are two inequivalent molecules in the unit cell. However, the crystal structure of 5-methyluridine hemihydrate [91] predicts one molecule per asymmetric unit cell. Therefore, we carried out powder X-ray diffraction analysis. The result (Appendix II) indicated that the as purchased 5-methyluridine is not the hemi-hydrate, but may be some other hydrate or solvate. The appearance of the carbon-13 spectrum of 5-methyluridine changes considerably after recrystallization to give the the hemi-hydrated form, as shown in Figure 5.5(b). Other experimental details are given in the caption. Some spinning sidebands appeared due to the relatively slow MAS rate of 6 kHz. The peaks were assigned based on the calculated values (see below).

In summary, the carbon sites of nucleosides can be divided into three different groups according to their isotropic chemical shifts. The carbon sites of nucleic acid bases are least shielded. The carbon atoms of sugar rings appear at relatively high field. The CH_3 groups appear at high field. The linewidths of the carbon sites which are directly bonded to nitrogen are slightly broader than those of the sugar rings due to the ^{13}C-^{14}N dipole interaction.

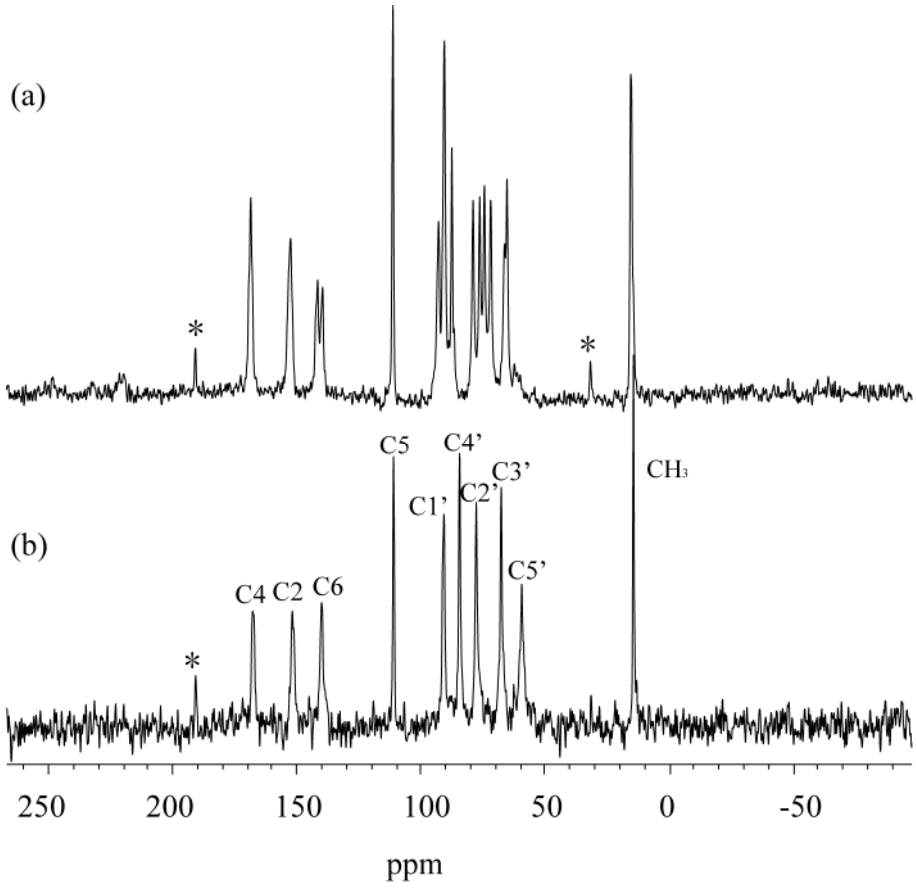

Figure 5.5: Part of carbon-13 MAS spectra of 5-methyluridine (a) before crystallization, and (b) after crystallization recorded at a MAS rate of 6 kHz using a 7 mm MAS probe and standard polarization pulse sequence with a contact time of 2 ms and a relaxation delay of 30 s. Proton decoupling with a field of 55.6 kHz was applied throughout the acquisition period which lasted 40.96 ms. The spectral width was 50 kHz and 8 scans were acquired. The spinning sidebands are indicated with asterisks.

5.3.2 CSA Tensors of Nucleosides

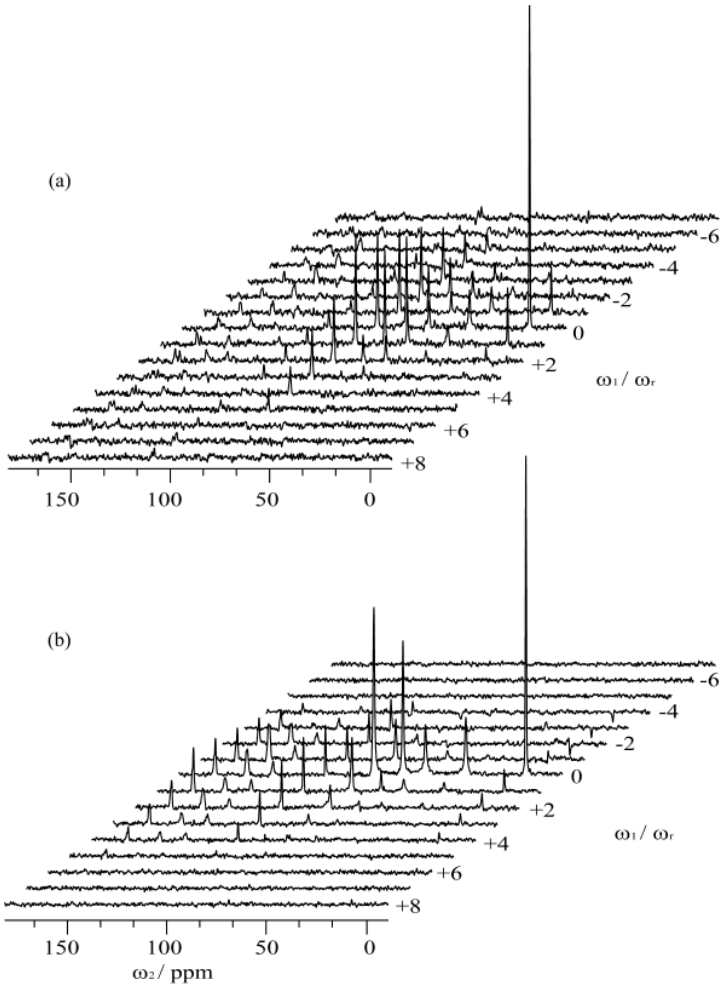

Figure 5.6: (a) Part of original CSA amplification spectrum of 2'-deoxythymidine recorded at a MAS rate of 4 kHz with a decoupling field of 85 kHz. The amplification factor is 8, resulting in an effective MAS rate in ω_1 of 500 Hz. There were 16 t_1 values in total with an increment of 15.6 μs, corresponding to 1/16 of the MAS period. The full spectral width was 50 kHz and the acquisition time was 40.96 ms. The relaxation delay was 60 s, and there were 192 scans for each of the 16 sequences. (b) As (a), except that the MAS rate was 10 kHz with a XiX heteronuclear decoupling field of 85 kHz.

Figure 5.6 shows CSA amplification spectra of 2'-deoxythymidine recorded at MAS rates of (a) 4 kHz and (b) 10 kHz with a constant amplification factor of 8. Further experimental parameters are given in the caption. At these MAS rates, no spinning sidebands appear in the ω_2 dimension so that the carbon-13 sites can be resolved by the isotropic chemical shifts, as in the standard CPMAS spectrum of Figure 5.3(a). Problems arising from overlap of ω_2 sidebands from different chemical sites are minimized. Carbon sites directly bonded to nitrogen suffer low signal-to-noise ratio due to the ^{13}C-^{14}N dipolar coupling and their larger chemical shift anisotropies. Similar CSA amplification experiments were carried out on the other nucleosides. For cytidine, a one-dimensional spectrum was also acquired at slower MAS rates.

Figures 5.7 to 5.12 show the results for all the carbon sites of six nucleosides. The mean values (based on the 68.3% confidence limit) for the principal components are shown in Tables 5.1 to 5.6 with δ_{xx}, $\delta_{yy,}$ and $\delta_{zz,}$ ordered such that $| \delta_{zz} - \delta_{iso} | \geq | \delta_{xx} - \delta_{iso} | \geq | \delta_{yy} - \delta_{iso} |$. The anisotropy and the asymmetry parameters were calculated according to the definitions $\zeta = \delta_{zz} - \delta_{iso}$ and $\eta = (\delta_{yy} - \delta_{xx})/ \zeta$. For comparison purposes, Tables 5.1 to 5.6 also show the previously measured isotropic chemical shift values and principal components of the chemical shift tensor, according to Stueber *et al*.

Figures 5.7 to 5.12 shows contour plots of χ^2, as a function of the anisotropy and asymmetry parameters for all resolved carbon sites of the six nucleosides. Error analysis was carried out using SIMPSON combined with MINUIT optimization package. The contours were plotted using MATLAB software. The boundaries of the

68.3% joint confidence region (blue lines) and 95.4% joint confidence region (brown lines) for the two parameters are shown.

For 2'-deoxythymidine (Figure 5.7) the joint confidence region for site C2 (c) is much larger than for the others due to the low signal-to-noise of the corresponding sidebands. This is the result of the ^{13}C-^{14}N dipolar coupling and the larger chemical

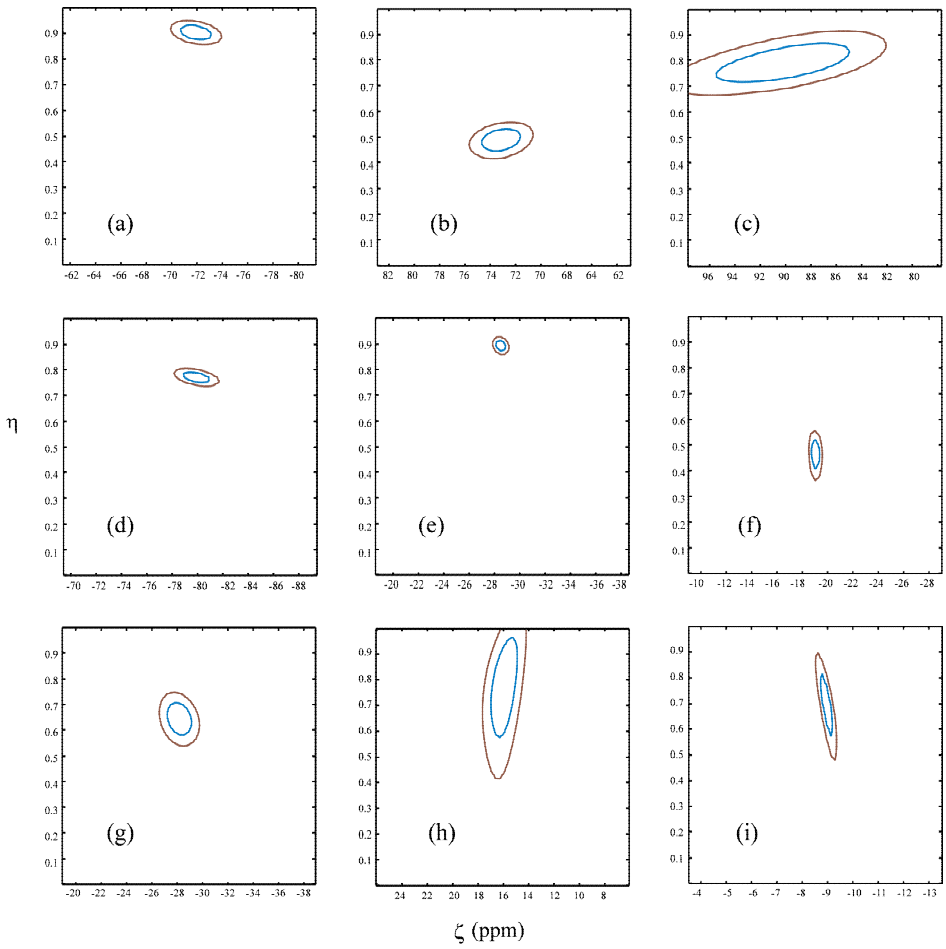

Figure 5.7: χ^2 statistic as a function of the CSA parameters ζ and η of 2'-deoxythymidine. Graphs for the carbon sites are presented: (a) C4, (b) C6, (c) C2, (d) C5, (e) C1' and C4', (f) C3', (g) C5', (h) C2', and (i) CH_3. The 68.3% joint confidence limit (blue) and 95.4% joint confidence limit (brown) for the two CSA parameters are shown.

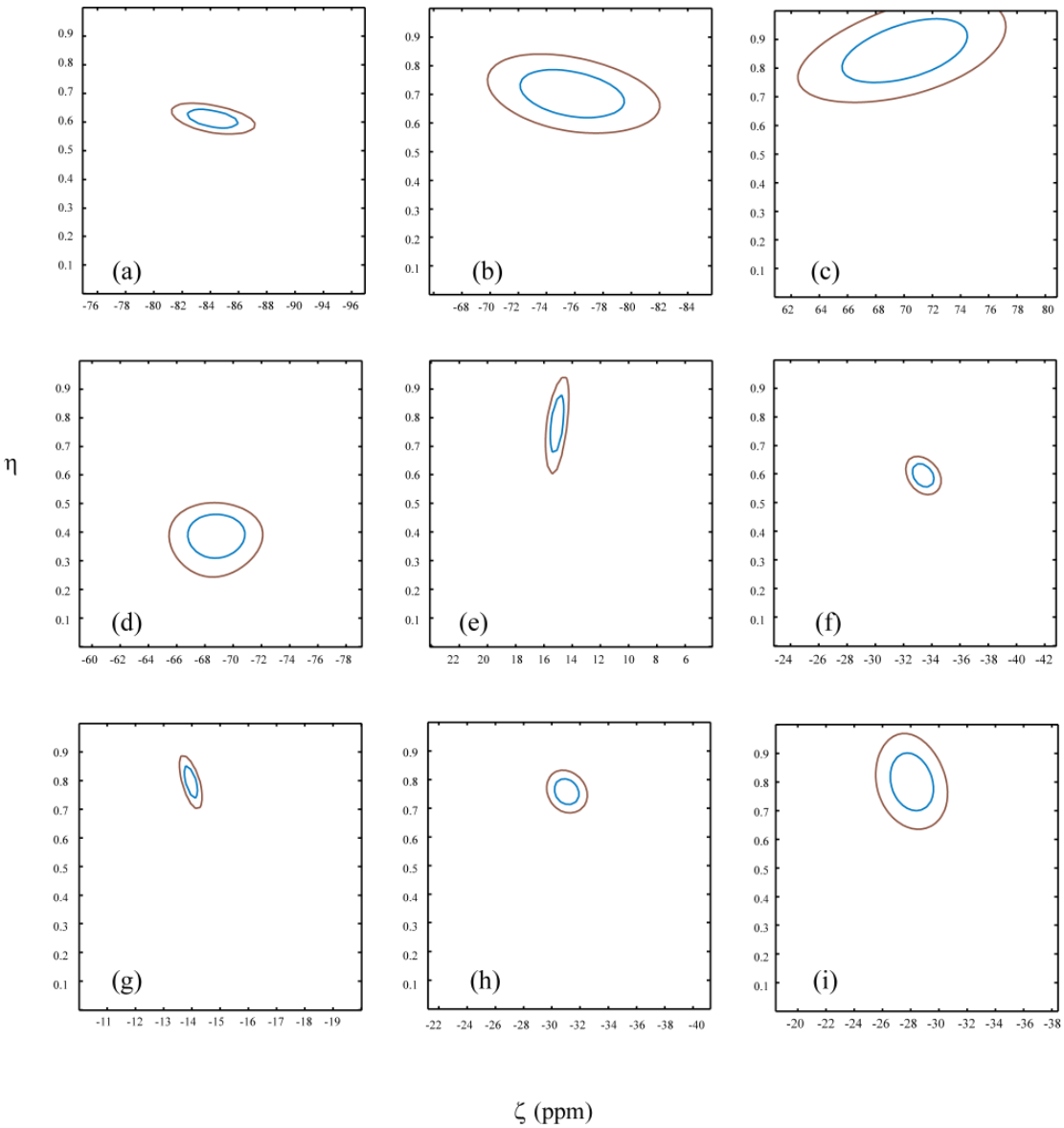

Figure 5.8: χ^2 statistic as a function of the CSA parameters ζ and η of adenosine. Graphs for the carbon sites are presented: (a) C2 and C6, (b) C4, (c) C8, (d) C5, (e) C1', (f) C4', (g) C3', (h) C2', and (i) C5' . The 68.3% joint confidence limit (blue) and 95.4% joint confidence limit (brown) for the two CSA parameters are shown.

shift anisotropy for this site. For C2' (h) and CH_3 (i), the 68.3 % confidence limit for η extends to ± 0.2 due to the limited number of spinning sidebands observed (5 and 6 spinning sidebands respectively). With the exception of C2, the 68.3 % confidence

limit on ζ is within ± 2 ppm, while if C2' and CH_3 are excluded the corresponding limit for η is ± 0.07.

For adenosine (Figure 5.8) the largest joint confidence region was again obtained for sites which are directly bonded to nitrogen (C4 (b) and C8 (c)). The sugar sites have smaller joint confidence regions due to the relatively high signal-to-noise ratio. The 68.3% confidence limits on the individual parameters ζ and η for all the sugar sites are within ± 3ppm and ± 0.07, respectively.

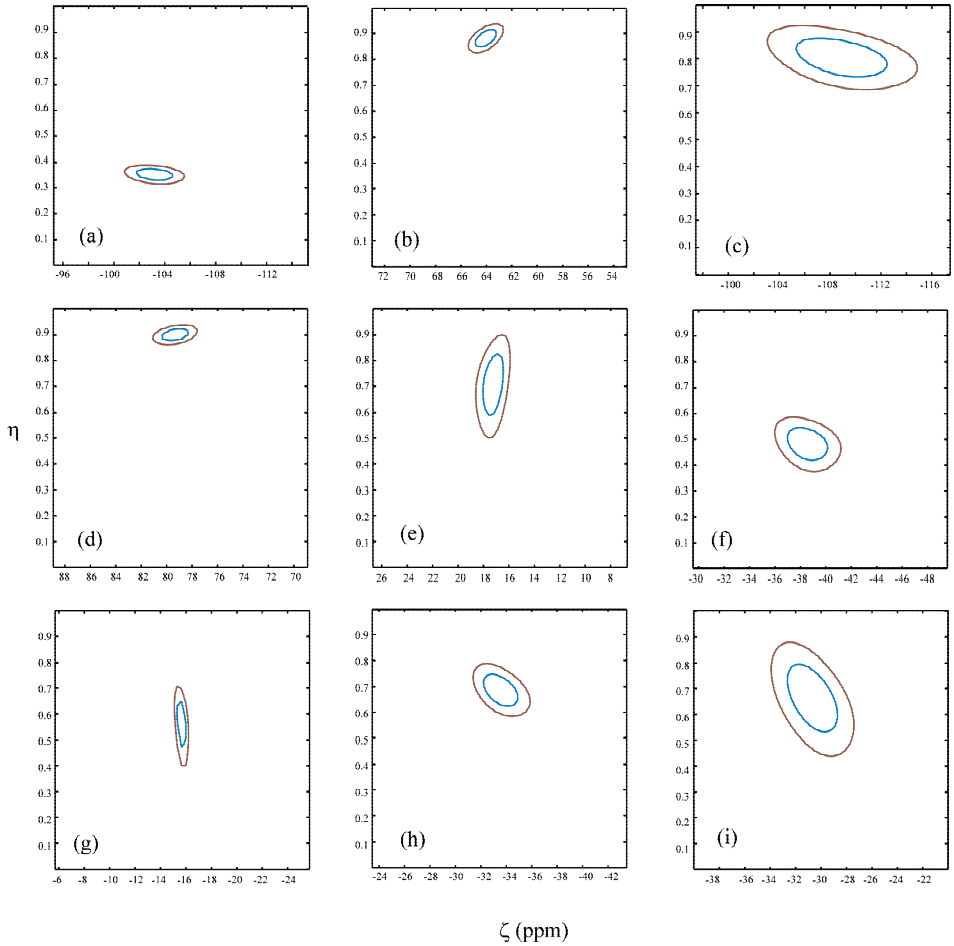

Figure 5.9: χ^2 statistic as a function of the CSA parameters ζ and η of cytidine. Graphs for the carbon sites are presented: (a) C4, (b) C2, (c) C6, (d) C5, (e) C1', (f) C4', (g) C2', (h) C3', and (i) C5' . The 68.3% joint confidence limit (blue) and 95.4% joint confidence limit (brown) for the two CSA parameters are shown.

For cytidine (Figure 5.9), a one-dimensional CPMAS spectrum was sufficiently well resolved to allow measurement of the CSA parameters for sites C2 (b) and C5 (d) with high signal-to-noise ratio. Hence, these sites show particularly small 68.3 % joint confidence regions with the corresponding limits on ζ and η around ± 1 ppm and 0.05, respectively.

For guanosine (Figure 5.10) large confidence limits were obtained for carbon C8 (d, e). This is explained by the fact that there are two crystallographically inequivalent molecules in the unit cell which are not well resolved due to the ^{13}C-^{14}N dipolar coupling. Once again the 68.3 % confidence limit on ζ is within ±3 ppm for most of the remaining sites.

Uridine (Figure 5.11) is a challenging sample since to there are two crystallographically inequivalent molecules in the unit cell. As with the other nucleosides, carbon sites directly bonded to nitrogen suffer low signal-to-noise ratio. These factors reflected in the larger joint confidence regions for sites such as C6 (Figure 5.11A e, f). However, excluding this site, the 68.3 % confidence limit on ζ is always within ±5 ppm.

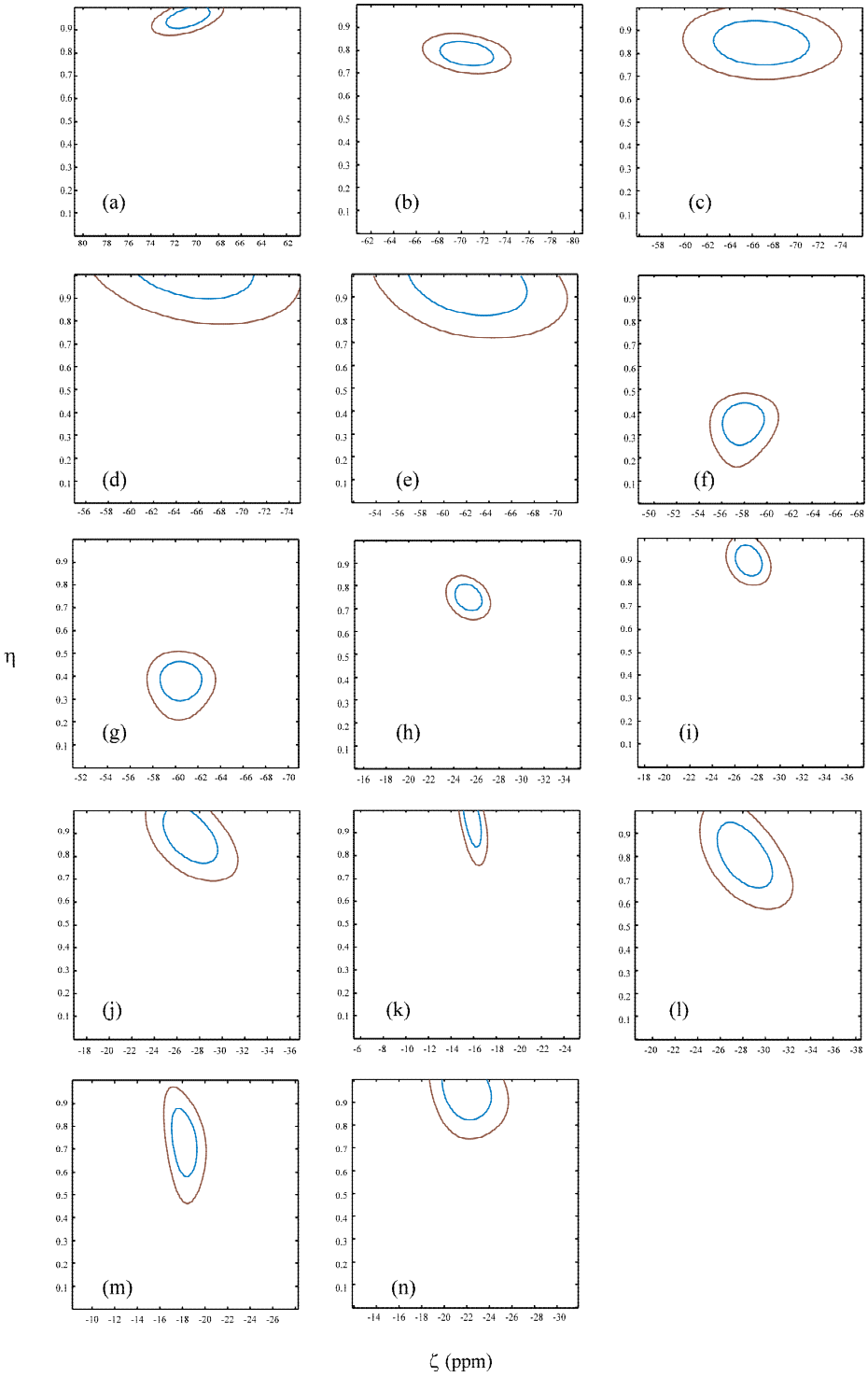

Figure 5.10: χ^2 statistic as a function of the CSA parameters ζ and η of guanosine. Graphs for the carbon sites are presented: (a) C6, (b) C4, (c) C2, (d, e) C8, (f, g) C5, (h) C4', (i) C1', (j, k) C2', (l, m) C3', and (n) C5'. The 68.3% joint confidence limit (blue) and 95.4% joint confidence limit (brown) for the two CSA parameters are shown.

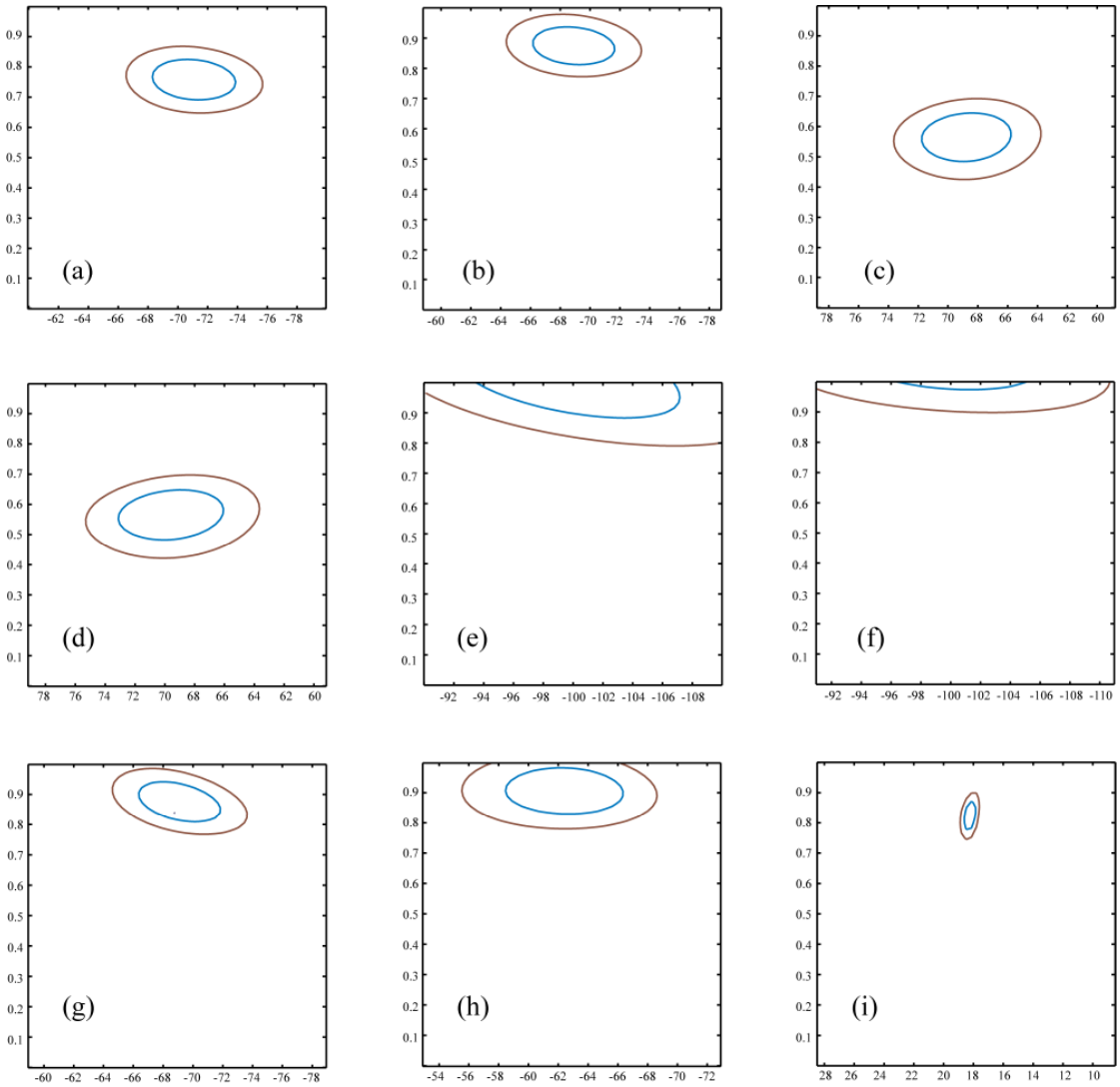

Figure 5.11A: χ^2 statistic as a function of the CSA parameters ζ and η of uridine. Graphs for the carbon sites are presented: (a, b) C4, (c, d) C2, (e, f) C6, (g, h) C5, (i) C1'. The 68.3% joint confidence limit (blue) and 95.4% joint confidence limit (brown) for the two CSA parameters are shown.

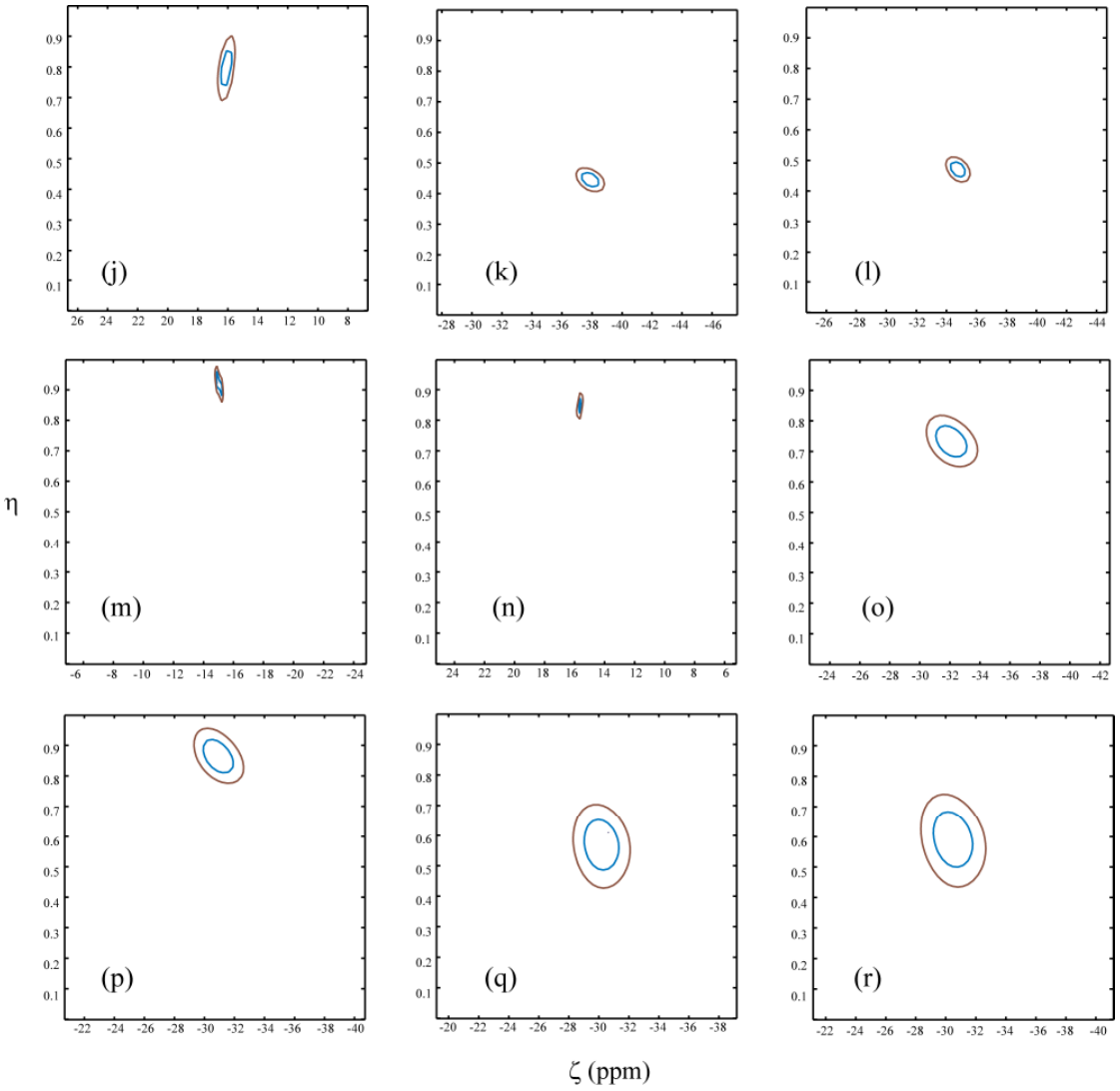

Figure 5.11B: χ^2 statistic as a function of the CSA parameters ζ and η of uridine. Graphs for the carbon sites are presented: (j) C1', (k, l) C4', (m, n) C2', (o, p) C3', (q r) C5'. The 68.3% joint confidence limit (blue) and 95.4% joint confidence limit (brown) for the two CSA parameters are shown.

For 5-methyluridine (Figure 5.12) the CSA amplification spectra have relatively high signal-to-noise ratio, which results in smaller joint confidence regions.

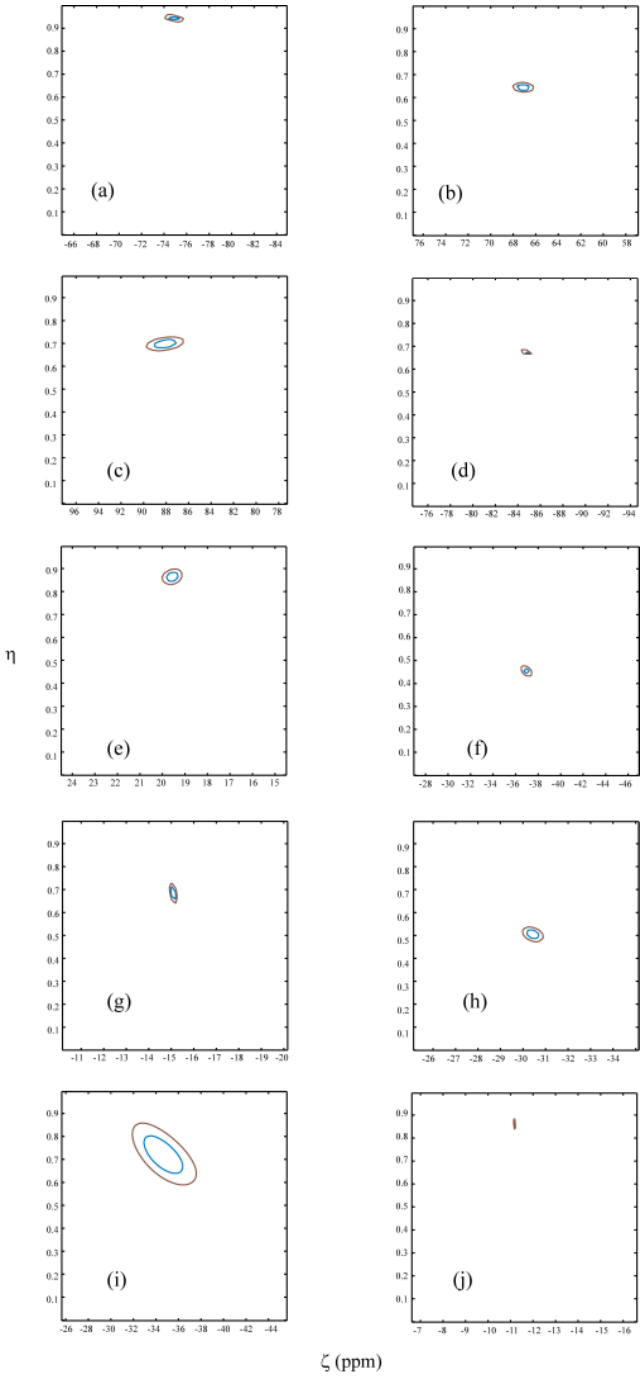

Figure 5.12: χ^2 statistic as a function of the CSA parameters ζ and η of 5-methyluridine. Graphs for the carbon sites are presented: (a) C4, (b) C2, (c) C6, (d) C5, (e) C1', (f) C4', (g) C2', (h) C3', (i) C5' and (j) CH_3. The 68.3% joint confidence limit (blue) and 95.4% joint confidence limit (brown) for the two CSA parameters are shown.

Table 5.1: Comparison of the principal components of carbon-13 chemical shift tensors[a] of 2'-deoxythymidine measured using CSA amplification with those measured previously.

Carbon site[b]	This work				Stueber *et al*.[90]			
	δ_{xx}	δ_{yy}	δ_{zz}	δ_{iso}	δ_{xx}	δ_{yy}	δ_{zz}	δ_{iso}
C2	94.3	130.1	222.0	148.8	96	124	226	148.6
C4	232.8	168.0	92.4	164.4	243	166	85	164.6
C5	180.2	118.6	29.4	109.4	187	117	24	109.7
C6	54.9	126.1	225.5	135.5	42	128	238	135.6
C1'[c]					122	88	47	85.2
C4'[c]	112.1	86.8	56.7	85.2	112	87	57	85.2
C2'	25.1	37.4	55.1	39.2	20	39	59	39.1
C3'	84.6	75.6	51.6	70.6	86	77	50	70.6
C5'	82.4	64.4	31.1	59.3	82	65	31	59.3
CH_3	16.8	10.5	0.0	9.1	17	10	1	9.1

[a] in ppm.
[b] Sites are assigned according with Ref. [90].
[c] These sites cannot be resolved in this work.

Tables 5.1 to 5.4 show a comparison between the principal components of the carbon-13 chemical shift tensors obtained in this work using CSA amplification and those reported in Ref. [90] of 2'-deoxythymidine, adenosine, cytidine, and guanosine respectively. Note that the principal components from Stueber *et al*. were quoted to the nearest ppm except for cytidine.

Table 5.2: Comparison of the principal components of carbon-13 chemical shift tensors[a] of adenosine measured using CSA amplification with those measured previously.

Carbon site[b]	This work				Stueber *et al*.[90]			
	δ_{xx}	δ_{yy}	δ_{zz}	δ_{iso}	δ_{xx}	δ_{yy}	δ_{zz}	δ_{iso}
C4	212.6	159.6	72.4	148.2	221	166	58	148.5
C5	167.3	140.5	50.7	119.5	167	145	47	119.7
C8	70.7	132.6	209.5	137.6	61	136	216	137.8
C2[c]					239	158	66	154.8
C6[c]	222.0	170.7	70.2	154.3	222	191	52	155.2
C1’	78.7	90.4	107.2	92.1	76	92	109	92.2
C2’	98.2	75.0	40.1	71.1	100	75	38	71.2
C3’	87.4	76.4	60.9	74.9	88	78	59	75
C4’	111.3	91.5	51.3	84.7	113	93	48	84.9
C5’	88.0	65.5	34.6	62.7	86	68	34	62.7

[a] in ppm.
[b] Sites are assigned according with Ref. [90].
[c] These sites cannot be resolved in this work.

The anisotropies measured in this work are generally less than the measurements from Stueber *et al*.

The rmsd between this work and Stueber *et al*. is 5.8 ppm for 2'-deoxythymidine which can be separated into contributions of 7.9 ppm for sites in the base and 2.1 ppm for the sugar ring. For adenosine, the rmsd between the results obtained in this work and those of Stueber *et al*. is 6.0 ppm for all the carbon sites and 2.1 ppm for the sugar ring. For cytidine the principal components from CSA amplification and those from Ref. [90] are in good agreement except for C4 of cytidine.

Table 5.3: Comparison of the principal components of carbon-13 chemical shift tensors[a] of cytidine measured using CSA amplification with those measured previously.

Carbon site[b]	This work				Stueber *et al*.[90]			
	δ_{xx}	δ_{yy}	δ_{zz}	δ_{iso}	δ_{xx}	δ_{yy}	δ_{zz}	δ_{iso}
C2	97.5	153.9	221.7	157.7	93.2	157.0	222.8	157.7
C4	237.8	200.6	64.4	167.6	248.2	204.2	49.0	167.3
C5	20.5	91.8	175.1	95.8	16.9	94.6	175.9	95.8
C6	240.5	153.4	33.6	142.5	240.7	151.5	34.8	142.2
C1’	77.8	90.0	109.7	92.5	76.0	90.0	111.8	92.7
C2’	87.8	79.1	59.9	75.6	89.2	78.2	59.4	75.6
C3’	94.6	71.9	33.0	66.5	96.9	72.4	30.3	66.5
C4’	112.6	94.1	45.6	84.1	113.8	93.3	44.4	84
C5’	84.9	64.7	30.7	60.1	85.1	65.4	29.8	60.1

[a] in ppm.
[b] Sites are assigned according with Ref. [90].
[c] These sites cannot be resolved in this work.

The corresponding two chemical shift tensors differ by 10.4, 3.6, and 15.4 ppm in the δ_{xx}, δ_{yy}, and δ_{zz} principal values, respectively. The rmsd is 5.1 ppm for all the carbon sites and 1.6 ppm for the sugar ring. For guanosine, the rmsd between the results obtained in this work and those of Stueber *et al*. is 9.5 ppm for all the carbon sites and 2.9 ppm for the sugar ring. These rmsd values indicate that the principal components measurements of sugar ring are in much better agreement than the carbon sites of base acid.

The experimental carbon-13 chemical shift tensor principal components and isotropic chemical shifts obtained using CSA amplification for uridine and 5-methyl

Table 5.4: Comparison of the principal components of carbon-13 chemical shift tensors[a] of guanosine measured using CSA amplification with those measured previously.

Carbon site[b]	This work				Stueber *et.al.*[90]			
	δ_{xx}	δ_{yy}	δ_{zz}	δ_{iso}	δ_{xx}	δ_{yy}	δ_{zz}	δ_{iso}
C2	211.5	154.7	82.9	149.7	223	165	66	152.1
					223	165	66	152.1
C4	214.1	159.2	80.9	151.4	223	165	66	151.4
					223	165	66	150.0
C5[c]	156.9	134.0	54.7	115.2	159	138	49	115.2
	155.1	134.2	57.8	115.7	160	140	49	115.9
C6	88.3	156.2	228.3	157.6	82	154	237	157.7
					82	154	237	157.7
C8[c]	198.5	137.7	75.1	137.1	211	134	66	136.9
	202.8	137.9	73.0	137.9	214	141	59	138.2
C1’	111.0	86.6	58.0	85.2	112	89	54	85.2
					112	89	54	85.2
C2’[c]	100.8	78.1	47.3	75.4	105	77	45	75.8
	104.3	80.2	51.6	78.7	103	79	55	78.9
C3’[c]	87.8	74.5	54.0	72.1	89	75	53	72.2
	91.7	76.3	60.3	76.1	86	80	62	76.2
C4’	108.5	89.6	61.1	86.4	108	92	60	86.6
					108	92	60	86.6
C5’	84.1	63.2	40.8	62.7	84	65	39	62.7
					84	65	39	62.7

[a] in ppm.
[b] Sites are assigned according to Ref. [90].
[c] assignment of resonances to the two distinct molecules per asymmetric unit cell.

Table 5.5 Experimental principal components of carbon-13 chemical shift tensors and tensor parameters[a] for uridine

Carbon site[b]	δ_{xx}	δ_{yy}	δ_{zz}	δ_{iso}
C2	95.9	134.9	219.8	150.2
	96.1	135.7	220.3	150.7
C4	228.4	168.5	95.1	164.0
	228.9	174.9	95.4	166.4
C5	163.0	102.9	29.3	98.4
	159.0	102.1	36.8	99.3
C6	238.6	139.4	40.2	139.4
	240.8	141.5	42.1	141.5
C1’	74.9	87.8	105.5	89.4
	73.2	88.4	108.1	89.9
C2’	56.8	71.9	88.6	73.1
	87.9	73.8	58.2	73.3
C3’	93.2	66.7	33.6	64.5
	94.6	71.1	24.7	66.8
C4’	105.9	89.5	45.5	80.3
	108.0	91.3	42.6	80.7
C5’	80.8	62.9	26.1	56.6
	83.4	66.2	29.5	59.7

[a] in ppm.
[b] Sites are assigned in this work by comparison with calculations.

-uridine are shown in Tables 5.5 and Table 5.6, respectively. To our knowledge, there are no previous reports of the chemical shift tensors of these two nucleosides. Assignments have been made by a comparison with calculated values, as described below.

Table 5.6: Experimental principal components of carbon-13 chemical shift tensors and tensor parameters[a] for 5-methyluridine

Carbon site[b]	δ_{xx}	δ_{yy}	δ_{zz}	δ_{iso}
C2	96.7	140.4	219.2	152.1
C4	240.7	170.2	93.1	168.0
C5	182.5	125.0	27.0	111.5
C6	65.5	127.1	228.3	140.3
C1’	73.2	90.0	111.0	91.4
C2’	91.2	80.7	63.3	78.4
C3’	91.4	75.8	38.0	68.4
C4’	111.8	95.2	48.0	85.0
C5’	89.9	64.9	25.5	60.1
CH_3	25.1	15.9	4.3	15.1

[a] in ppm.
[b] Sites are assigned in this work by comparison with calculations.

5.3.3 Comparison with Calculated CSA Tensors

Much of the advancement in NMR today comes from the aid provided by numerical calculations. A combined experimental and theoretical calculation was used to explore molecular configuration as well as their NMR properties such as chemical shifts, spin-spin coupling constants, shieldings (such as ^{1}H, ^{13}C, and ^{15}N), etc. [110-112]. Calculated carbon-13 chemical shift tensors of 2'-deoxythymidine, adenosine, cytidine, guanosine, uridine and 5-methyluridine, are shown in Tables 5.7-5.12. The agreement between experimental and calculated isotropic chemical shifts is in very good (see Figure 5.15), with the rmsd ranging from 1.3 ppm for adenosine to 3.3 ppm

Table 5.7: Comparison experimental and calculated principal components[a] of CSA tensors for 2'-deoxythymidine.

Carbon site	Experiment			Calculation		
	δ_{iso}	ζ	η	δ_{iso}[b]	ζ[c]	η
C2	148.8	73.2	0.49	146.3	68.3	0.23
C4	164.4	–72.0	0.90	162.3	67.4	0.96
C5	109.4	–80.0	0.77	112.1	–79.7	0.67
C6	135.5	90.0	0.79	136.9	87.0	0.98
C1’				88.1	–35.4	0.87
C4’	85.2	–28.5	0.89	86.7	–29.5	0.82
C2’	39.2	15.9	0.77	36.4	19.1	0.98
C3’	70.6	–19.0	0.47	73.3	–20.5	0.51
C5’	59.3	–28.2	0.64	58.8	–30.0	0.51
CH_3	9.1	–9.1	0.70	5.7	8.9	0.82

[a] δ_{iso} and ζ in ppm.
[b] σ_{ref} = 167.1 ppm.
[c] anisotropy scaling factor = 0.86.

for uridine. However, the anisotropy parameters are systematically overestimated due to an underestimation of the paramagnetic contribution to the shielding by the currently used PBE exchange-correlation functionals as discussed in Ref. [113]. This in turn results in a over- and under-estimation of the maximum and minimum principal components, respectively. For this reason a linear scaling of the tensor span δ_{zz} - δ_{xx} is required before comparison with the experimental results. Note that a single scaling factor sufficies for all sites in a given molecule and that the factor is consistent across the range of nucleosides studied, varying between 0.84 and 0.90.

Table 5.8: Comparison experimental and calculated principal components[a] of CSA tensors for adenosine.

Carbon site	Experiment			Calculation		
	δ_{iso}	ζ	η	δ_{iso}[c]	ζ[d]	η
C4	148.2	–75.8	0.70	146.8	–80.8	0.61
C5	119.5	–68.8	0.39	120.6	–66.3	0.07
C8	137.6	71.9	0.86	136.2	69.3	0.95
C2[b]	154.3	–84.1	0.61	154.8	–85.4	0.76
C6[b]				151.5	–89.7	0.04
C1’	92.1	15.1	0.77	94.4	–17.9	0.66
C3’*	71.1	–31.0	0.75	71.6	–34.6	0.83
C2’*	74.9	–14.0	0.78	75.8	–15.6	0.65
C4’	84.7	–33.4	0.59	85.8	–36.8	0.44
C5’	62.7	–28.1	0.80	61.9	–28.8	0.73

[a] δ_{iso} and ζ in ppm.
[b] these sites cannot be resolved in this work.
[c] σ_{ref} = 168.4 ppm.
[d] anisotropy scaling factor = 0.89.
* corrected assignment based on our calculation when compared to Ref. [90].

For 2'-deoxythymidine, scaling the calculated values by 0.86 results in a rmsd of 2.9 ppm from the values measured by CSA amplification experiment, whereas a scaling factor of 0.95 gave a rmsd of 3.6 ppm from the data of Stueber *et al*. [90]. Figure 5.13a shows a correlation between the chemical isotropic shifts and the anisotropies obtained from CSA amplification experiments and the scaled values from calculations. The agreement is very good. For carbon sites of C4 and CH_3, the calculated anisotropy is of opposite sign to the CSA amplification value and those reported by Stueber *et al*. However, these sites have η close to unity where the sign of anisotropy is poorly defined.

Table 5.9: Comparison experimental and calculated principal components[a] of CSA tensors for cytidine.

Carbon site	Experiment			Calculation		
	δ_{iso}	ζ	η	δ_{iso}[b]	ζ[c]	η
C2	157.7	64.0	0.88	154.8	60.6	0.85
C4	167.6	–103.2	0.36	161.7	–98.5	0.30
C5	95.8	79.3	0.90	95.6	–78.9	0.93
C6	142.5	–108.9	0.80	141.9	–109.0	0.73
C1’	92.5	17.2	0.71	95.4	–19.7	0.68
C2’	75.6	–15.7	0.56	77.9	–16.7	0.75
C3’	66.5	–33.5	0.68	67.1	–37.3	0.65
C4’	84.1	–38.5	0.48	87.2	–40.4	0.44
C5’	60.1	–29.4	0.69	60.9	–31.8	0.73

[a] δ_{iso} and ζ in ppm.
[b] σ_{ref} = 170.5 ppm.
[c] anisotropy scaling factor = 0.90.

Scaling factors of 0.89 and 0.99 were required for experimental results of adenosine from CSA amplification experiments and those from Stueber *et al*, respectively, giving an rmsd of 2.9 ppm from the CSA amplification measurements and an rmsd 3.6 ppm from that reported by the latter. In solution, C6 possesses a higher shift than C2 and the two carbons are separated by approximately 4 ppm [114] ,whereas in the CPMAS spectrum reported here there is only 0.6 ppm difference. On the other hand, the calculations predict a reversed order assignment and 3.3 ppm separation for these two carbon atoms. Since C2 and C6 cannot be resolved in the CSA amplification experiments, the comparison described above is based on the result omitting these carbon sites. Earlier results of Stuerber *et al*. assign the isotropic shift

Table 5.10: Comparison experimental and calculated principal components[a] of CSA tensors for guanosine.

Carbon site	Experiment			Calculation		
	δ_{iso}	ζ	η	δ_{iso}[c]	ζ[d]	η
C2	149.7	–66.8	0.85	147.6	–66.3	0.56
				149.3	–70.1	0.55
C4	151.4	–70.5	0.78	148.5	–72.9	0.71
				149.9	–73.7	0.70
C5[b]	115.2	–60.5	0.38	116.2	–59.3	0.12
	115.7	–57.9	0.36	116.8	–56.9	0.17
C6	157.6	70.7	0.96	153.6	73.8	0.74
				153.9	69.9	0.84
C8[b]	137.1	–62.0	0.98	136.2	65.7	0.91
	137.9	–64.9	1.00	136.7	–70.7	0.86
C1’	85.2	–27.2	0.90	87.2	–29.9	0.66
				87.5	–32.1	0.57
C2’[b]	75.4	–28.1	0.81	76.8	30.8	0.93
	78.7	–27.1	0.89	80.7	23.4	0.91
C3’[b]	72.1	–18.1	0.73	73.5	–20.0	0.84
	76.1	–15.8	0.97	78.2	–15.1	0.64
C4’	86.4	–25.3	0.75	87.2	–29.9	0.46
				89.6	–24.4	0.42
C5’	62.7	–21.9	0.95	62.1	–25.8	0.75
				62.9	–21.4	0.84

[a] δ_{iso} and ζ in ppm.
[b] assignment of resonances to the two distinct molecules per asymmetric unit cell.
[c] anisotropy scaling factor = 0.87.
[d] σ_{ref} = 169.0 ppm.

of 71.1 ppm and 74.9 ppm to sites C2’ and C3’ respectively. In comparing both the isotropic shift and the asymmetry our calculations suggest a reversed assignment in

Table 5.11: Comparison experimental and calculated principal components[a] of CSA tensors for uridine

Carbon site	Experiment			Calculation		
	δ_{iso}	ζ	η	δ_{iso}[b]	ζ[c]	η
C2	150.2	69.6	0.56	145.4	63.7	0.35
	150.7	68.8	0.57	148.7	64.1	0.46
C4	164.0	–68.9	0.87	159.4	69.2	0.92
	166.4	–71.0	0.76	164.2	–68.0	0.95
C5	98.4	–69.1	0.87	97.9	–72.0	0.83
	99.3	–62.5	0.91	98.5	–65.7	0.99
C6	139.4	–99.2	1.00	138.8	–96.3	0.88
	141.5	–99.3	1.00	140.9	–102.4	0.76
C1’	89.4	16.1	0.80	91.6	–17.7	0.39
	89.9	18.2	0.83	92.8	–17.9	0.69
C2’	73.1	15.5	0.85	75.1	19.7	0.56
	73.3	–15.1	0.94	75.2	–15.5	0.88
C3’	64.5	–30.9	0.86	64.4	–35.5	0.86
	66.8	–32.1	0.73	68.7	–37.4	0.71
C4’	80.3	–34.8	0.47	82.6	–37.4	0.38
	80.7	–37.9	0.44	83.0	–38.1	0.31
C5’	56.6	–30.5	0.59	56.8	–33.4	0.52
	59.7	–30.2	0.57	60.2	–34.3	0.46

[a] in ppm, except η.
[b] σ_{ref} = 168.5 ppm.
[c] anisotropy scaling factor = 0.84.

which the resonance at 71.1 ppm is assigned to C3’ and that at 74.9 ppm to site C2’. One exception is C1’ which has the opposite sign for the anisotropy in the CSA amplification and calculated values.

For cytidine, scaling the calculated width by 0.90 resulted in a rmsd of 2.7 ppm from the anisotropies measured by this work, whereas a scaling factor of 0.95 gave a rmsd of 5.8 ppm from the data from Stueber *et al*. The anisotropy of carbon atom C4 from Stueber *et al*. were found to be 9.1 ppm less than the non-scaled calculated data, suggesting that this anisotropy has been considerably over-estimated by Stueber *et al*. Apart from the C4 site, CSA parameters of all other carbons agree well with calculated data. The very good agreement between the experimental data and scaled calculations is shown in Figure 5.13 (c). Exceptions are the carbon sites C5 and C1' for which the calculated anisotropy is of opposite sign to the experimental value.

For guanosine, scaling factors of 0.87 and 0.98 were required for experimental results from CSA amplification experiments and those from Stueber *et al*., giving an rmsd of 2.3 ppm from the CSA amplification measurements and an rmsd 4.3 ppm from those reported by the latter. Stueber *et al*. assigned the resonance 152.1 ppm to C2 and 151.4 ppm to C4. These assignments were based on a comparison of their calculated results [90]. However, our calculations predict a reversed order for these two carbon atoms. The CSA parameters in Table 5.10 suggest a revised assignment: the resonance at 149.7 ppm was assigned to C2 and the resonance at 151.4 ppm was assigned to C4. With the new assignment the experimental anisotropy of both sites is a much better match to the calculated values.

Figure 5.14 (a) shows plots of the anisotropy of guanosine from the scaled calculated values against the calculated isotropic shift, superimposed on a similar plot of experimental values. The agreement is very good. Exceptions are the carbon atoms C1' and C8 have experimental and calculated anisotropies of opposite sign.

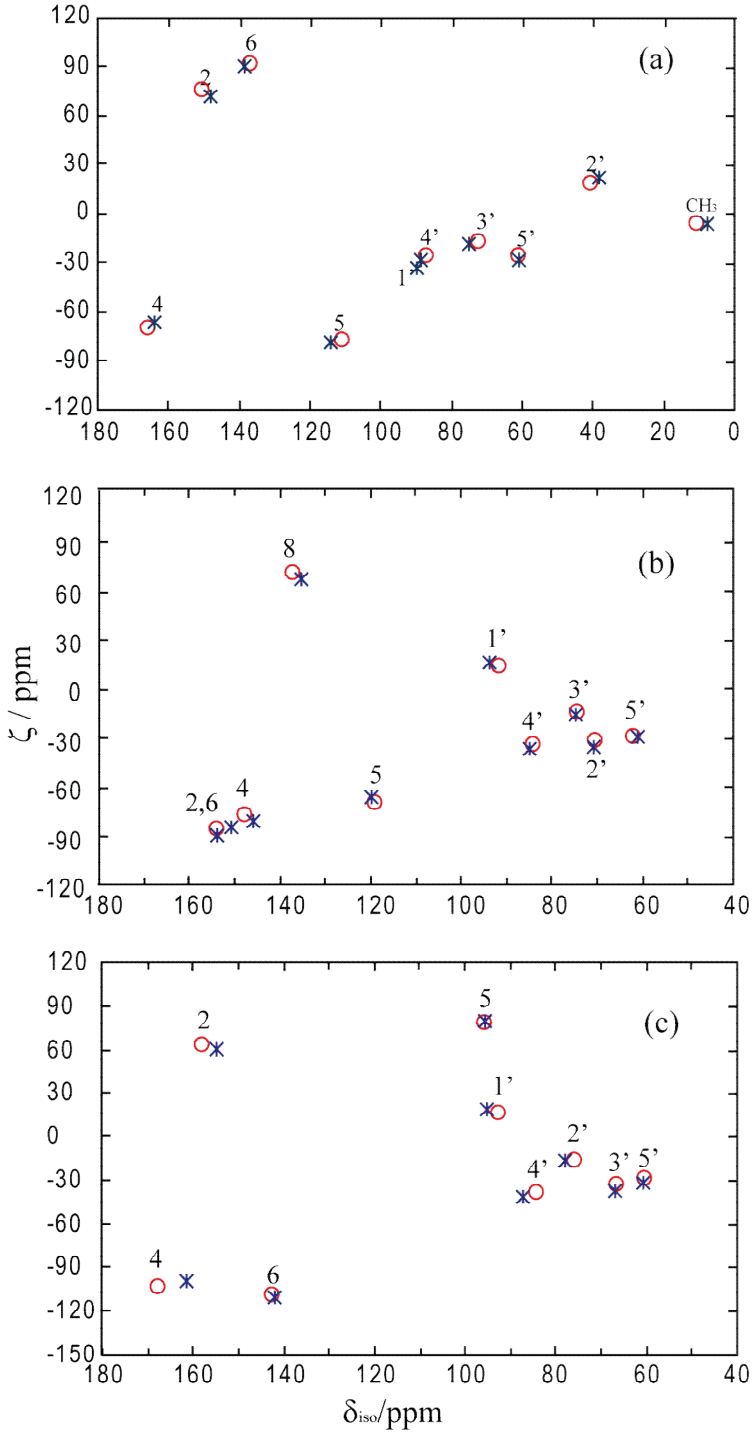

Figure 5.13: Plots of the shift anisotropy, ζ, against the isotropic shift (circles) measured using CSA amplification and (asterisks) calculated and scaled for (a) 2'-deoxythymidine, (b) adenosine and (c) cytidine. The experimental points are labeled according to the carbon sites.

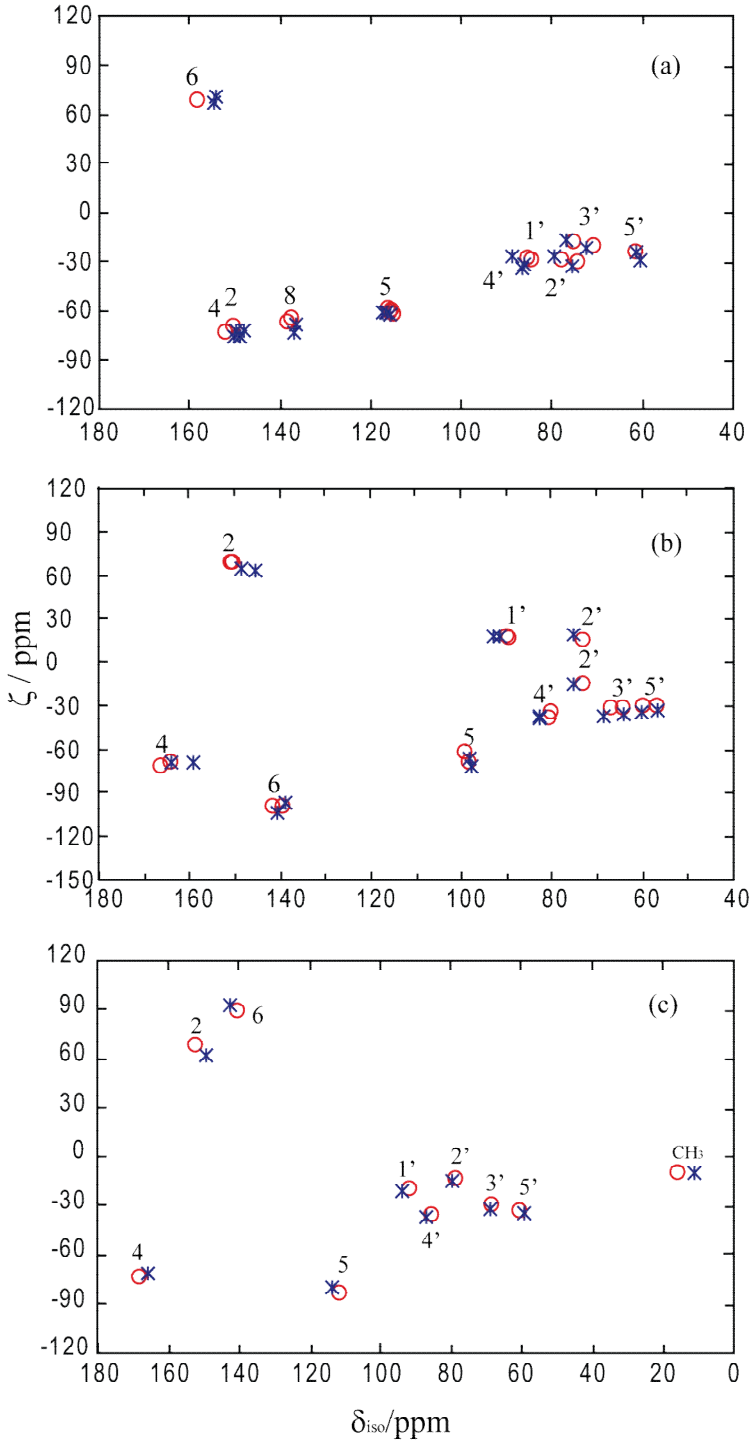

Figure 5.14: Plots of the shift anisotropy, ζ, against the isotropic shift (circles) measured using CSA amplification and (asterisks) calculated and scaled for (a) guanosine; (b) uridine and (c) 5-methyluridine. The experimental points are labeled according to the carbon sites.

Table 5.12: Comparison experimental and calculated principal components[a] of CSA tensors for 5-methyluridine**.**

Carbon site	Experiment			Calculation		
	δ_{iso}	ζ	η	δ_{iso}[b]	ζ[c]	η
C2	152.1	67.1	0.65	149.6	61.4	0.45
C4	168.0	–74.9	0.94	166.1	72.9	0.83
C5	111.5	–84.5	0.68	113.8	–81.9	0.56
C6	140.3	88.0	0.70	142.2	–92.1	0.94
C1’	91.4	19.6	0.86	93.6	–22.2	0.43
C2’	78.4	–15.1	0.69	79.7	–15.9	0.97
C3’	68.4	–30.4	0.51	68.5	–33.8	0.77
C4’	85.0	–37.0	0.45	86.7	–38.0	0.40
C5’	60.1	–34.6	0.72	59.1	–35.8	0.67
CH_3	15.1	–10.8	0.86	11.0	–10.8	0.62

[a] in ppm, except η.
[b] σ_{ref} = 169.1 ppm.
[c] anisotropy scaling factor = 0.86.

For uridine and 5-methyluridine, there is no previous report about chemical shift tensors so far. Tables 5.5-5.6 and 5.11-5.12 show the experimental CSA principal values and the scaled calculated results. Scaling factors of, respectively, 0.84 and 0.86 were required for uridine and 5-methyluridine, giving a rmsd from the CSA amplification measurements of 3.3 ppm and 2.9 ppm, respectively. A very good correlation between experimental and scaled calculated results is shown in Fig. 5.14 (b-c). For uridine, there are twice as many isotropic shifts as expected, indicating that there are two molecules in the unit cell. Exceptions are carbon C4 and C1' for which the calculated anisotropy is of opposite sign to the CSA amplification value. Carbon

atom C4, C6 and C1' in 5-methyluridine have the opposite sign between the experimental and calculated values.

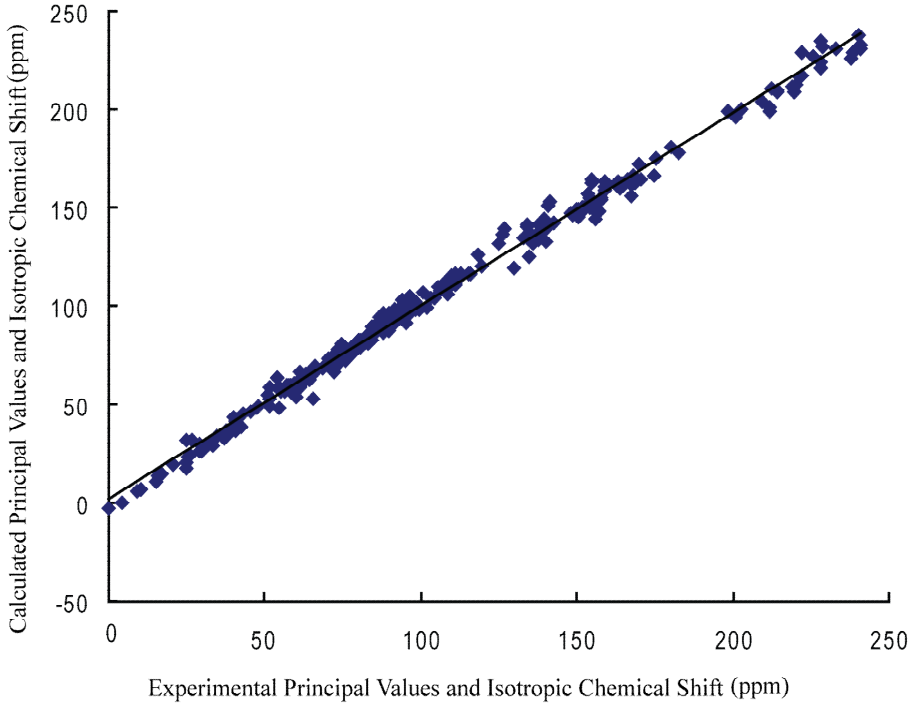

Figure 5.15: Plot showing the correlation between calculated and experimental principal values and isotropic carbon-13 chemical shifts of 2'-deoxythymidine, adenosine, cytidine, guanosine, uridine and 5-methyluridine. The calculated data incorporates scaling by a factor 0.84 to 0.90 for the different molecules.

Figure 5.15 shows the correlation between all calculated and experimental principal values and isotropic carbon-13 chemical shifts. A linear regression equation is obtained as: y $(^{13}C)_{calc}$ = 0.97*x$(^{13}C)_{exp}$ + 2.22 with R^2 = 0.994, indicating a very good correlation. The rmsd value of the isotropic chemical shift correlation is 2.2 ppm and 4.86 ppm for the principal values correlation.

5.4 Conclusions

The chemical shift tensors of 2'-deoxythymidine, adenosine, cytidine, guanosine, uridine and 5-methyluridine have been determined using chemical shift anisotropy amplification experiment. To our knowledge, this is the first report about CSA values of uridine and 5-methyluridine. The first-principles calculations using density functional theory within the planewave-pseudopotential approach reproduce the experimental chemical shift anisotropy parameters accurately. The CSA values suggest a revised assignment of C2 and C4 in the case of guanosine. Larger deviations were obtained for the base carbon sites due to the ^{13}C-^{14}N dipolar decoupling.

Chapter 6

Solid-State NMR studies of vinylphosphonate-linked nucleotides

6.1 Introduction

In the first part of this chapter, the experiment termed MAS-J-HMQC [115] was used to study the vinylphosphonate-linked nucleotides (sample **1** and **4**). In analogy to liquid-state HMQC experiments, the sequence uses heteronuclear multiple quantum coherences to provide isotropic chemical shift correlation between proton and carbons which are directly bonded. In the second part, high-resolution Phosphorus-31 NMR was used to extract isotropic and anisotropic chemical shift parameters as well as a sensitive monitor of the progress of solid-phase synthesis of oligonucleotides.

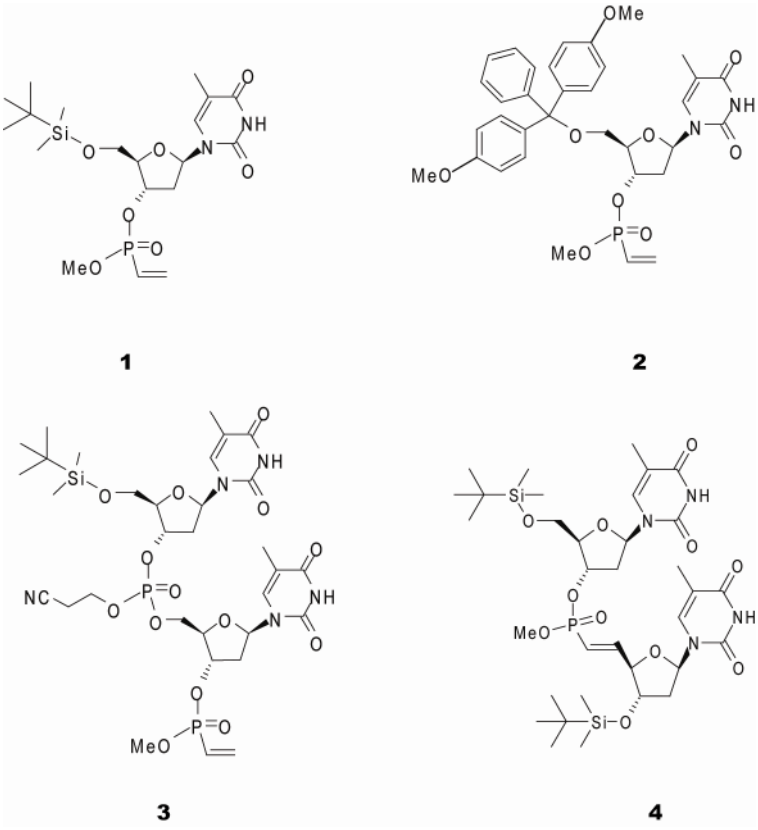

Figure 6.1: Structures of the vinylphosphonate-linked nucleotides.

6.2 Experimental

^{1}H- ^{13}C MAS-J-HMQC spectra were recorded at a Larmor frequency of 75.46 MHz on samples **1** and **4** packed into 4 mm rotors spinning in a double-resonance MAS probe. The MAS rate was 12 kHz. Proton decoupling at a field strength of 100 kHz was used. Phosphorus-31 NMR spectra were recorded at a Larmor frequency of 121.47 MHz packed into 4 mm or 3 mm rotors.

6.3 High-Resolution Proton-Carbon Correlation Experiment using DUMBO-1

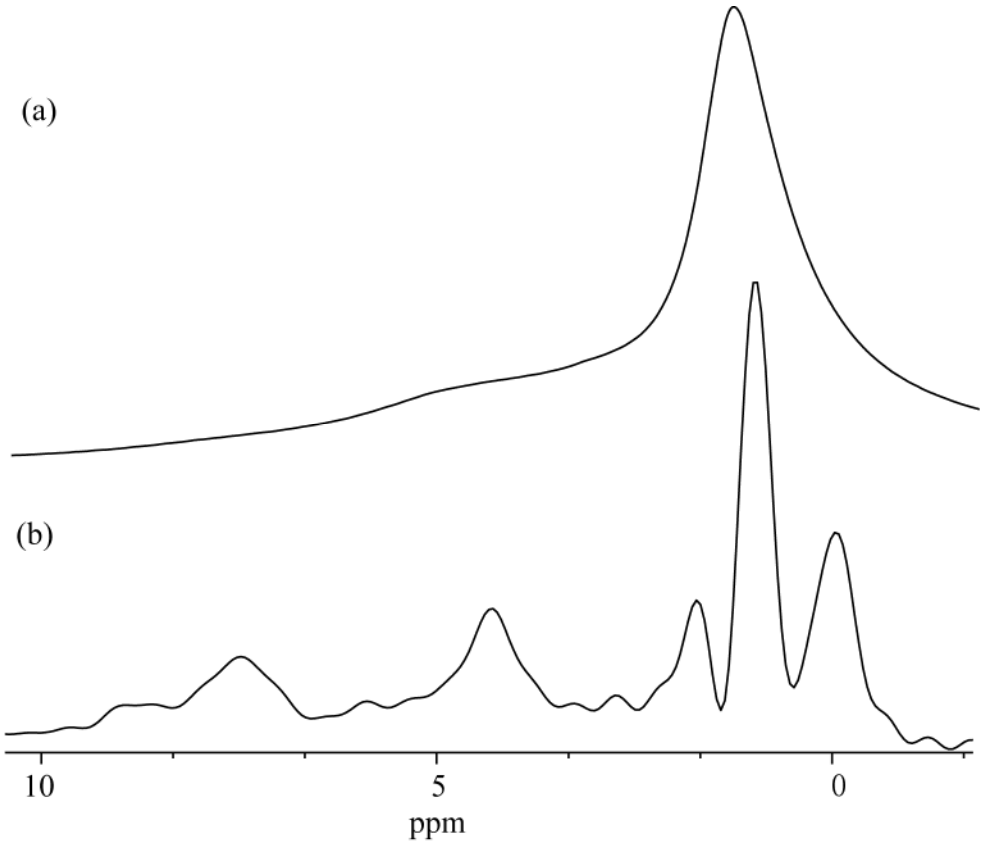

Figure 6.2: One-dimensional proton spectra of sample **1**. The spinning frequency was set to 12 kHz for experiments (a, b). The high-resolution spectrum (b) was acquired using DUMBO-1 homonuclear decoupling. An experimentally determined scaling factor of 0.5 was used to measure chemical shifts.

Results and Discussion

The proton MAS spectrum (upper) and high resolution proton spectrum (bottom) using DUMBO-1 decoupling [116] are shown in Figure 6.2. A 4 mm CPMAS probe was used. The proton decoupling field strength was set 100 kHz. It is obvious that the DUMBO-1 sequence yields well resolved proton spectra. The spectrum contains sharp

strong peaks at δ 0.1, 0.9 and 1.9 which can be assigned to the Si-methyl, *tert*butyl and methyl of base respectively. The resonances at δ 1.9-6.7 can possibly be assigned to the protons of sugar ring and the peaks at δ 6.8-10.0 can be assigned to unsaturated resonances. To get further structural information, a two dimensional HMQC experiment was recorded.

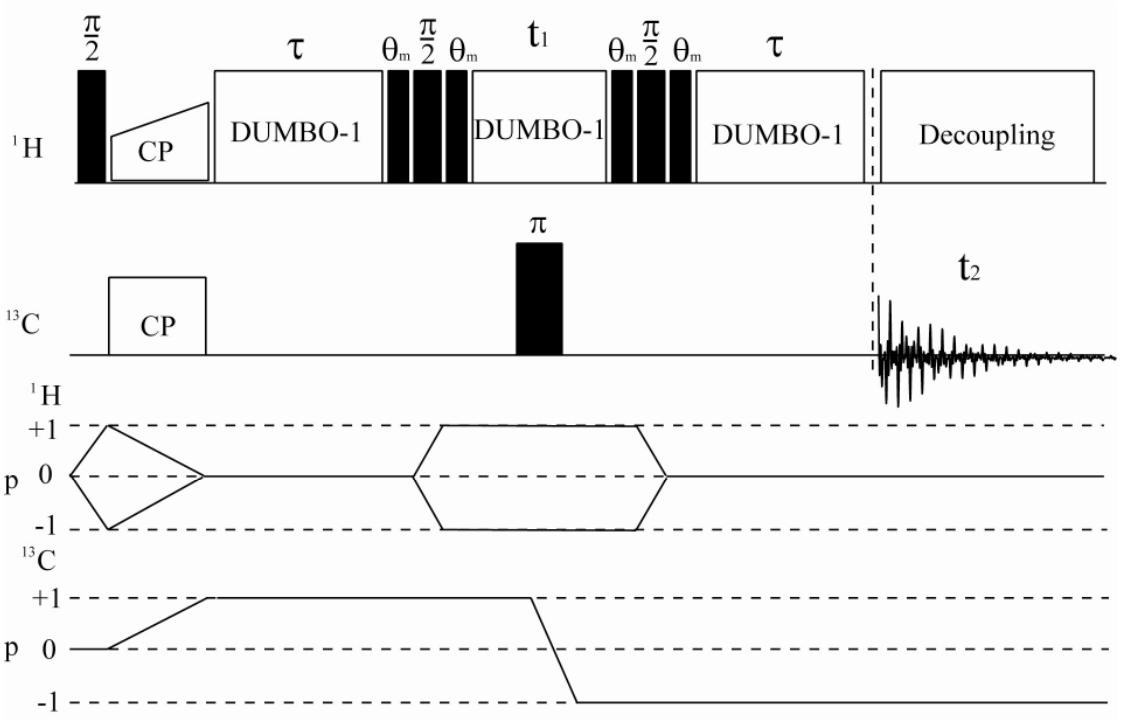

Figure 6.3: Pulse sequence and coherence transfer pathway for the MAS-*J*-HMQC experiment.

The pulse sequence for a MAS-*J*-HMQC [115] experiment is shown in Figure 6.3. After cross-polarization from ^{1}H, the magnetization of carbon evolves during the delay τ. DUMBO-1 was used to remove the proton-proton dipolar decoupling during this period. Figure 6.4 shows the MAS-*J*-HMQC spectrum recorded on sample **1**. The spinning rate is 12 kHz. The proton rf field strength was set to 100 kHz during both

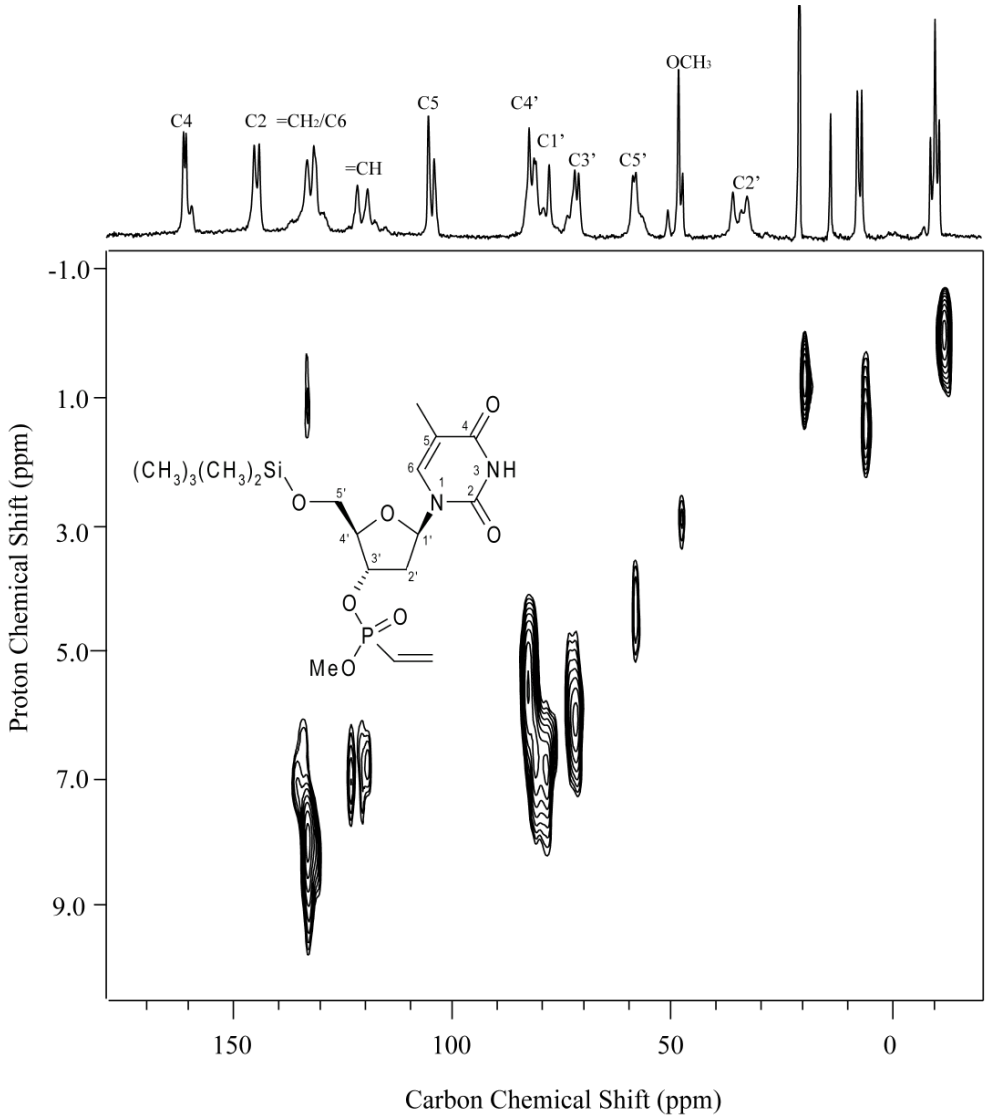

Figure 6.4: Carbon–proton two-dimensional MAS-*J*-HMQC spectrum of a natural abundance sample **1**. The spinning frequency was 12 kHz and τ was 1.5 ms. A total of 128 t_1 increments with 608 scans each were collected. The proton rf. field strength was set to 100 kHz during both the delays τ (DUMBO-1 decoupling) and acquisition (TPPM decoupling). The contact time in the cross-polarization step was 3 ms. The 1D CP-MAS ^{13}C spectrum is shown above the 2D spectrum. In the proton dimension, the Si-methyl resonance of the TBS (*t*-butyldimethylsilyl) group is referred to 0 ppm with respect to TMS by analogy with a solution state spectrum From Ref. [87].

the τ delays (DUMBO-1 decoupling) and during acquisition (TPPM decoupling). The value of τ was set to 1.5 ms to ensure only one-bond chemical shift correlations are presented. Other experimental parameters are given in figure caption. The assignment of the one-dimensional carbon spectrum has been discussed in Chapter 4. Clearly the MAS-*J*-HMQC experiment may lead to the unambiguous assignment of the proton spectrum and also can further confirm the assignment of carbon spectrum. Three carbon resonances at low field as well as the one around 20 ppm, which are not correlated to any proton chemical shift, can be assigned to quaternary carbons. From carbon chemical shift considerations [117], the carbon resonance at 19 ppm can be assigned to the quaternary carbon of the *t*-butyl group, and that around at 110 ppm to the quaternary carbon C5; the remaining two quaternary resonances must therefore correspond to the two carbonyl groups (C2 and C4). All the protonated carbons are correlated with their attached protons except for C2'. This can be possibly attributed to the low signal-to-noise. In the low-field part of the spectrum two correlation peaks can be clearly distinguished, the carbon resonance which correlates with proton around 7.0 ppm can be assigned to terminal double bond, and the other carbon resonance correspond to C6. In the high-field part of the spectrum eight correlation peaks can be clearly distinguished. The three carbon resonances which correlate with protons around 1.0 ppm (carbon chemical shifts of –4.9, 11.8 and 26.1 ppm) can be assigned to methyl groups. Again from carbon chemical shifts, the peak at 26.1 ppm can be assigned to the *t*-butyl methyl groups, the carbon at 11.8 ppm to the base methyl group and the carbon at –4.9 ppm to the methyl group which directly bonded to Si. The OCH_3 can be assigned to the peak at 53.4 ppm which has a proton correlation at 3.0

ppm. The remaining four peaks between 60 and 90 ppm, therefore, correspond to the carbons of sugar ring. Note that, for the =CH group, there are two distinct correlation peaks because of phosphorus-carbon coupling.

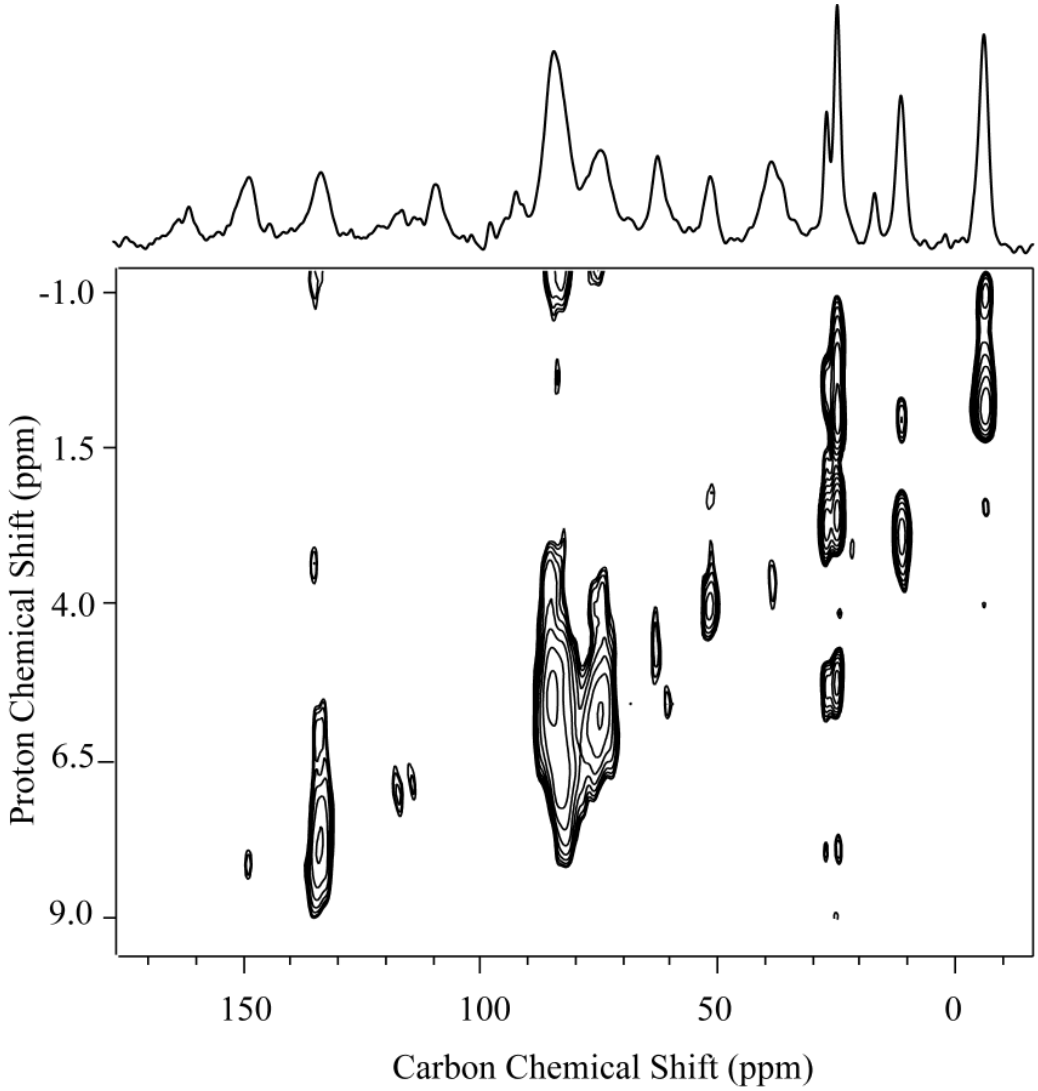

Figure 6.5: Two-dimensional MAS-*J*-HMQC spectrum of a natural abundance sample **4**. The spinning frequency was 12 kHz and τ was 1.5 ms. A total of 128 t_1 increments with 2368 scans each were collected. In the proton dimension, the Si-methyl resonance of the TBS group is referred to 0 ppm with respect to TMS by analogy with a solution state spectrum from Ref. [87].

From the above comments, we can see that a MAS-*J*-HMQC experiment leads to unambiguous assignment of proton spectrum if the carbon spectrum is assigned. In this case, we can go towards assignment without the information of assignments of carbon spectrum, simply by analysing the one bond ^{1}H-^{13}C correlations which combine carbon proton chemical shift information.

Figure 6.5 shows the MAS-*J*-HMQC spectrum recorded on sample **4**, a methyl phosphonate T*T dimer which was prepared from sample **1**. The experimental parameters are same as Figure 6.4 except that 2368 scans were acquired. In the high-field part of the spectrum, 9 correlation peaks can be clearly distinguished. The four carbon resonances which correlated with protons around 1.5 ppm (carbon chemical shifts of –4.5, 13.1, 27.4 and 28.0 ppm) can be assigned to methyl groups. Compare to the spectrum of sample **1**, there is some t_1 noise. The C2' of sugar ring can be assigned to the peak at 40.5 ppm, which has a correlation at 3.8 ppm. The peaks of carbons at 53.4 and 64.7 ppm correlate with protons at around 4 ppm and can be assigned to the OCH_3 and C5' of sugar ring, respectively. The remaining two carbons at 76.8 and 86.2 ppm therefore correspond to the C3', C1' and C4' of sugar ring carbons. In the low-field part of spectrum, the carbons which are not correlated to any proton chemical shifts correspond to quaternary carbons. Comparing with the spectrum of sample **1**, the carbon resonance at 164.5 ppm can be assigned to the C4 of base groups, and that at 111.8 pm, to the C5 of the base groups. Considering Ref. [87], the carbon C2 and one of the C6 of base groups may not be resolved in this work, and therefore a peak of carbon resonance at 151.6 ppm which correlated with proton at around 8 ppm can be assigned C6 of one of base groups. The peak of carbon at 136.1 ppm therefore corresponds to the C6 of the other base group. The =CH can be assigned to the peak at

around 119.3 ppm, which has two correlation peaks due to the phosphorus-carbon coupling.

Comparing spectrum of sample **1** to spectrum of sample **4**, we can see that the correlation peak of the terminal double bond has disappeared; therefore, MAS-*J*-HMQC can be used as a sensitive monitor of the progress of synthesis of oligonucleotides in this case.

6.4 Phosphorus-31 Solid State NMR of Vinylphosphonate-linked Nucleotide

Solid-phase synthesis of oligonucleotides has greatly increased our understanding of DNA and RNA. Site-specific introduction of modified nucleotides at any position in a given oligonucleotide has now become routine, allowing easy chemical probe of define functionalities [118]. Solid-state NMR can be used to study chemical structure, conformation and dynamics in solid-phase supported syntheses. Phosphorus-31 studies of DNA and RNA benefit from the 100% abundance of the isotope which leads to good sensitivity and the restriction of one site per nucleotide. As demonstrated below, the incorporation of modified phosphonate linkages allows problems with lack of shift resolution in the spectrum to be overcome. This allows the use of solid-state phosphorus-31 NMR as a sensitive monitor of the progress of solid-phase synthesis of oligonucleotides. In this section we also describe measurements of the phosphorus-31 CSA parameters of the modified synthetic nucleotides **1**-**3**.

Results and discussion

Solid-state phosphorus-31 NMR of free oligonucleotides 1-3

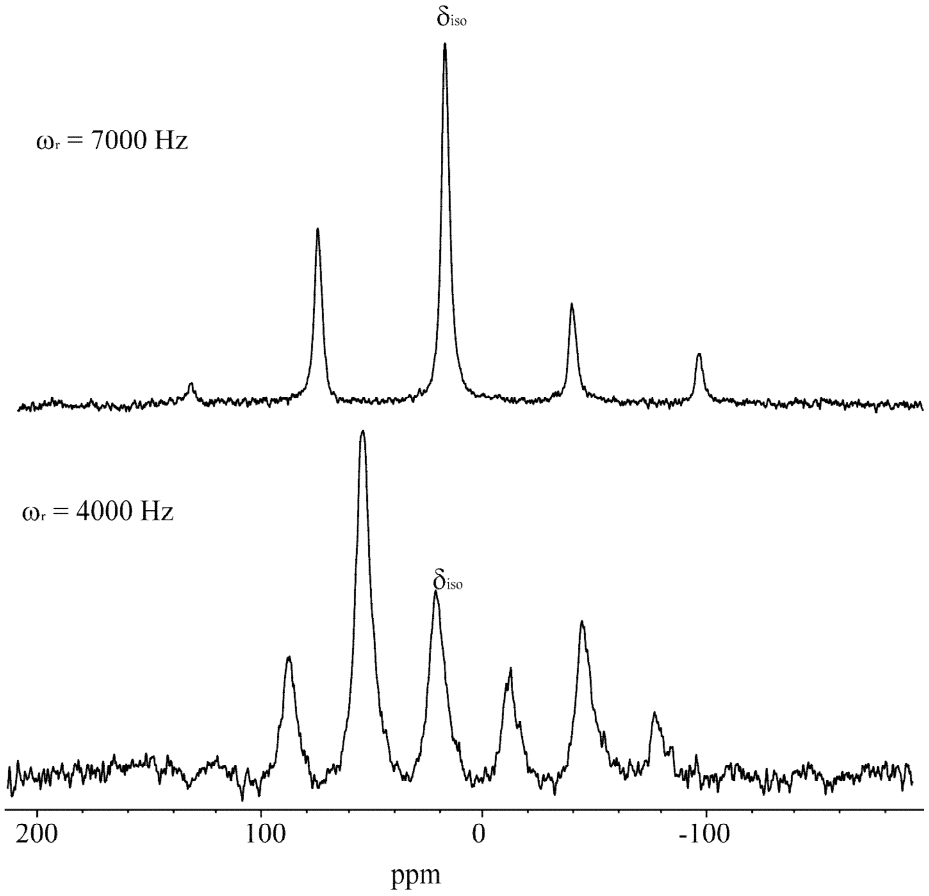

Figure 6.6: Phosphorus-31 MAS spectrum of sample **1** recorded at a rate of 4 and 7 kHz using a 4 mm MAS probe and a pulse delay of 25 s. The full spectral width was 50 kHz and 64 scans were acquired. The isotropic resonances are indicated as δ_{iso} and other peaks are spinning sidebands.

Figure 6.6 and 6.7 show the phosphorus-31 MAS spectra at two MAS rates (7 kHz and 4 kHz) of samples **1** and **2** respectively. In both cases the isotropic resonance is flanked by a series of spinning sidebands. Figure 6.8 shows similar phosphorus-31 MAS spectrum and CSA amplification spectrum for the dimer **3**. For the CSA amplification experiment the MAS rate was 16 kHz and the reduction factor was 8,

resulting in an apparent MAS rate in the ω_1 dimension of 2 kHz. Other experimental parameters are given in figure caption. Hence, the high resolution of the isotropic sites in the ω_2 dimension is combined with a large number of spinning sidebands in ω_1 which can be accurately analyzed to give the CSA parameters. Figure 6.8 (b) demonstrates the utility of CSA amplification in studies of vinylphosphonate-linked nucleotides.

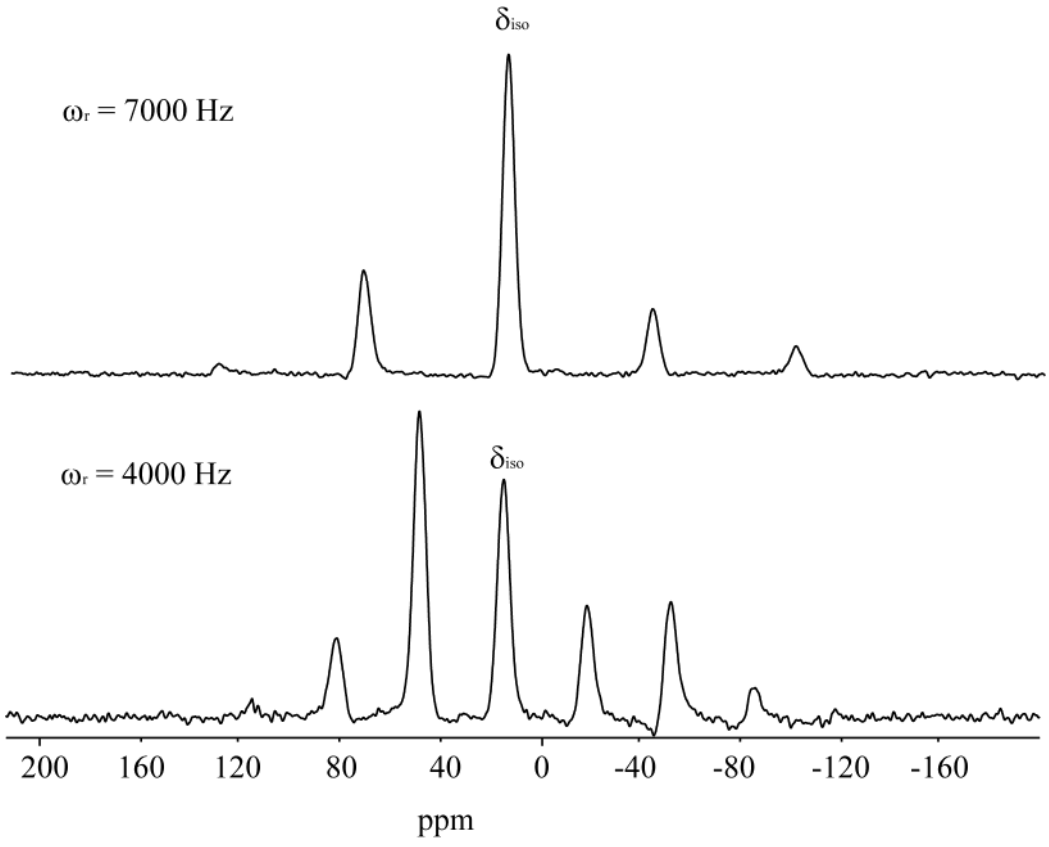

Figure 6.7: Phosphorus-31 MAS spectrum of sample **2** recorded at a rate of 4 and 7 kHz using a 4 mm MAS probe and the pulse delay is 20 s. The full spectral width was 50 kHz and 64 scans were acquired. The isotropic resonances are indicated as δ_{iso} and other peaks are spinning sidebands.

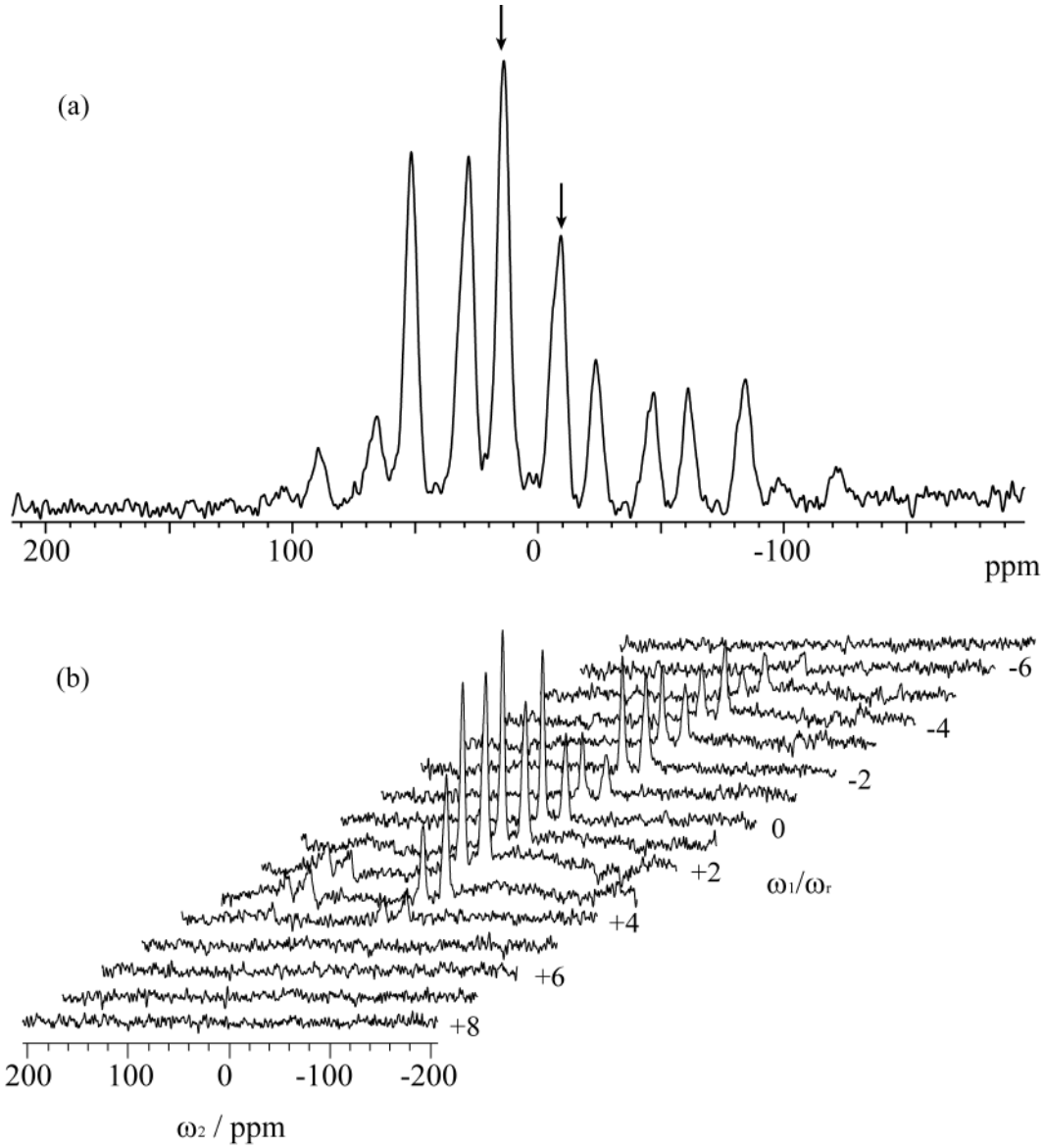

Figure 6.8: (a) Phosphorus-31 MAS spectrum of sample **3** recorded at a rate of 4.5 kHz using a 3mm MAS probe and the pulse delay is 15 s. The full spectral width was 50 kHz and 2048 scans were acquired. The isotropic resonances are indicated by arrows and other peaks are spinning sidebands. (b) Phosphorus-31 CSA amplification spectrum of **3** recorded at a MAS rate of 16 kHz. The amplification factor was 8, resulting in an effective MAS rate of 2 kHz. There are 16 t_1 values in total with an increment of 3.91 μs, corresponding to 1/16 of the MAS period. The acquisition time was 40.96 ms and 1024 scans were acquired.

Table 6.1 Phosphorus-31 chemical shift tensors of sample **1**-**3**

Sample 1			
Spinning rate (kHz)	δ^{a}_{iso}（ppm）	ζ_{aniso}(ppm)	η
4	21.1	–117.4	0
7	21.3	–118.1	0.01
11	21.1	–117.8	0
Sample 2			
Spinning rate (kHz)	δ^{a}_{iso}(ppm)	ζ_{aniso}(ppm)	η
4	17.2	–99.4	0
7	17.0	–99.5	0.03
11	17.4	–97.2	0.01
Sample 3			
Spinning rate (kHz)	δ^{a}_{iso}(ppm)	ζ_{aniso}(ppm)	η
4.5	15.1	–92.1	0
	-8.0	–103.2	0
8.0	15.1	–91.2	0
	-8.0	–104.8	0.12
CSA amplification (16 kHz)	15.1	–89.9	0
	-8.0	–102.6	0.17

[a]. All chemical shifts were referenced to ATP.

Table 6.1 lists the phosphorus-31 CSA parameters extracted from an analysis of the spinning sideband intensities of the three samples. This analysis was carried out using a least-squares fitting procedure. This involves comparing the experimental sideband intensities to those simulated for a standard MAS spectrum using SIMPSON. The variation of the extracted ζ and η obtained by employing an increasing number of crystallite orientations for powder averaging was investigated to ensure convergence to within an acceptable margin of error. The powder averaging was achieved using 20 (α, β) crystallite angles distributed according to the REPULSION scheme[79]. 40 γ angles were used according to the gcompute method in SIMPSON. Essentially identical values of the CSA parameters were obtained from one-dimensional MAS spectra and the CSA amplification experiments.

Solid-state phosphorus NMR of oligonucleotides bound to CPG

Figure 6.9 shows phosphorus-31 MAS spectra recorded in a solid-phase oligomer synthesis. The solid-phase support used here is controlled-pore glass (CPG). In the second spectrum the vinyl phosphonate nucleotide has a resolved phosphorus-31 chemical shift and integration of the two peaks reveals that they are in the expected ratio of 1:3, indicating a largely successful conversion of (**a**) to (**b**). In the last spectrum the vinyl phosphonate nucleotide has a resolved phosphorus-31 chemical shift and integration of the two peaks reveals that they are in the expected ratio of 1:4, indicating that phosphorus-31 MAS NMR can be used to follow the reactions involved in oligonucleotide elongation synthesis. Hence, it seems likely that individual steps during a solid-phase oligonucleotides synthesis can be monitored conveniently using a combination of phosphorus-31 MAS NMR and synthetic

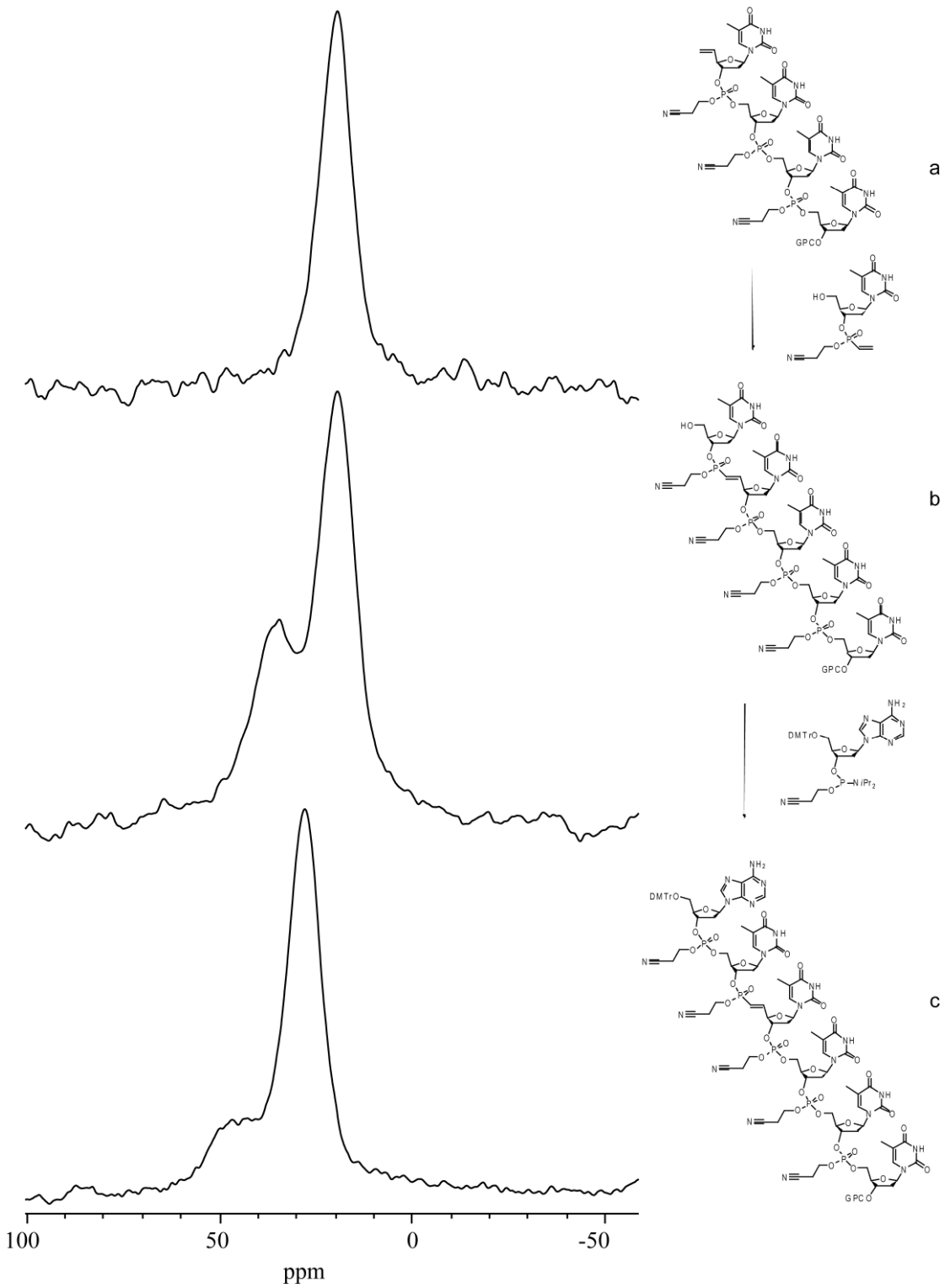

Figure 6.9: Phosphorus-31 CPMAS NMR spectra of oliginucleotides attached to a CPG solid-phase support. The spinning rate was 11 kHz for those experiments.

Vinyl phosphonate nucleotides without the need to remove the oligomer from the solid-support.

Chapter 7

Summary and Outlook

This thesis describes a modified CSA amplification experiment which correlates the standard magic angle spinning (MAS) spectrum in the ω_2 dimension with a sideband pattern in ω_1 in which the intensities are identical to those expected for a sample spinning at some fraction $1/x_a$ of the actual rate ω_r. This experiment is a PASS-type experiment with the advantage that only a few t_1 increments are required without losing the resolution of different chemical sites. The need to store the magnetization along the z-axis for t_1 which was a feature of our original CSA amplification experiment is eliminated. This version has π-pulse sequences with different timings to generate a series of Ξ values varying from 0 to 2π in the evolution dimension. Double Fourier transform of the two-dimensional FID produces the required the CSA amplification spectrum. The sideband patterns in the ω_1 dimension can be used to measure the principal components of CSA tensors by conventional methods. The CSA amplification experiment is suitable for measuring very small anisotropies without the need for very slow MAS rates which lead to rotor instability. An amplification factor x_a of up to 48 has been demonstrated by experiment using a

sequence of 47 π pulses. With large x_a the experiment can operate at higher MAS rates which allows the incorporation of state-of-art heteronuclear XiX decoupling schemes.

By comparison of chemical shift tensors from experiments and those from the first-principles calculations, conformational information can be elucidated. This comparison can also be used to assign NMR spectra where resolution of isotropic chemical shifts is poor.

In Chapter 6, we demonstrated that solid-state NMR can be a very useful tool to study vinylphosphonate-linked nucleotides as well as a sensitive monitor of the progress of solid-phase synthesis of oligonucleotides.

In future, the CSA amplification methodology will be extended to measurements of heteronuclear dipolar couplings since the heteronuclear dipolar Hamiltonian similar to CSA, can be manipulated by π-pulse sequences applied to one of the coupled nuclei [119].

Appendix

A.I Analytical Timing Solutions for the CSA Amplification

Sequences of Five π Pulses

Sequence which contain five pulses disposed symmetrically about their midpoint *T*/2 with a total duration equal to an integer number of rotor periods were found by Crockford *et al*. [57], i.e.

$$T = n\tau_r \qquad t^{(3)} = T/2 \qquad t^{(4)} = T - t^{(2)} \qquad t^{(5)} = T - t^{(1)} \tag{A.1}$$

Therefore, the imaginary part of Eq.2.4.38 is zero and the equation system becomes

$$\begin{aligned} 4\cos\left(\omega_r t^{(1)}\right) - 4\cos\left(\omega_r t^{(2)}\right) + x_a + 2(-1)^n - 2 = 0 \\ 4\cos\left(2\omega_r t^{(1)}\right) - 4\cos\left(2\omega_r t^{(2)}\right) + x_a = 0 \end{aligned} \tag{A.2}$$

Solutions for timings in sequences with *n* even and odd are given by

$$\begin{aligned} \omega_r t^{(1)} &= \pi - (-1)^{k_1} \cos^{-1}\left(\frac{x_a - 2}{8}\right) + 2\pi k_3 \\ \omega_r t^{(2)} &= (-1)^{k_2} \cos^{-1}\left(\frac{x_a + 2}{8}\right) + 2\pi k_4 \end{aligned} \tag{A.3}$$

and

$$\begin{aligned} \omega_r t^{(1)} &= \pi - (-1)^{k_1} \cos^{-1}\left(\frac{16 + x_a^2 - 10x_a}{8(x_a - 4)}\right) + 2\pi k_3 \\ \omega_r t^{(2)} &= (-1)^{k_2} \cos^{-1}\left(\frac{16 + x_a^2 - 6x_a}{8(x_a - 4)}\right) + 2\pi k_4 \end{aligned} \tag{A.4}$$

Respectively, where k_1 to k_4 are integers. The maximum amplification factor which can be achieved using five π pulses is $x_a = 8$. The shortest realizable sequences with

$t_1 < t_2 < t_3 < t_4 < t_5 < T$ can be found in Table A.1 with amplification factors x_a ranging from 2 to 8. It should be noted that the timings in Table A.1 are well spaced, so that there are no problems of overlap with finite lengths.

Table A.1: Examples of the shortest realizable pulse timings t^p for five-pulse sequences

x_a	$t^{(1)}/\tau_r$	$t^{(2)}/\tau_r$	t^3/τ_r	$t^{(4)}/\tau_r$	$t^{(5)}/\tau_r$	T/τ_r
2	0.25000	0.33333	0.50000	0.66667	0.75000	1
3	0.35745	0.41957	0.50000	0.58043	0.64255	1
4	0.29022	0.88497	1.00000	1.11502	1.70978	2
5	0.31118	0.91957	1.00000	1.08040	1.68882	2
6	0.16667	1.00000	1.50000	2.00000	2.83333	3
7	0.21656	1.04611	1.50000	1.95390	2.78340	3
8	0.25000	1.00000	1.50000	2.00000	2.75000	3

A.II The X-Ray Report of 5-methyluridine

Table 1. Crystal data and structure refinement for 5-methyluridine at 296(2)K.

Empirical formula	C10 H15 N2 O6.50
Formula weight	267.24
Crystal description	colourless tablet
Crystal size	0.31 x 0.26 x 0.17 mm
Crystal system	Orthorhombic
Space group	P 21 21 2
Unit cell dimensions	a = 14.0399(11) A alpha = 90 deg. b = 17.3222(14) A beta = 90 deg.

c = 4.8633(4) A gamma = 90 deg.

Volume	1182.76(16) A^3
Reflections for cell refinement	1553
Range in theta	2.25 to 21.65 deg.
Z	4
Density (calculated)	1.501 Mg/m^3
Absorption coefficient	0.127 mm^-1
F(000)	564
Diffractometer type	Bruker SMART1000 CCD area detector
Wavelength	0.71073 A
Scan type	omega
Reflections collected	7469
Theta range for data collection	2.25 to 27.47 deg.
Index ranges	-17<=h<=17, -22<=k<=22, -6<=l<=6
Independent reflections	1600 [R(int) = 0.037]
Observed reflections	1334 [I>2sigma(I)]
Absorption correction	None
Decay correction	None
Structure solution by	direct methods
Hydrogen atom location	difmap
Hydrogen atom treatment	refall
Data / restraints / parameters	1600/0/229 (least-squares on F^2)
Final R indices [I>2sigma(I)]	R1 = 0.0290, wR2 = 0.0702
Final R indices (all data)	R1 = 0.0372, wR2 = 0.0741
Goodness-of-fit on F^2	1.02
Absolute structure parameter	not reliably determined
Extinction coefficient	0.019(3)
Final maximum delta/sigma	0.001

Weighting scheme
calc w=1/[\s^2^(Fo^2^)+(0.047P)^2^] where P=(Fo^2^+2Fc^2^)/3

Largest diff. peak and hole 0.143 and -0.142 e.A^-3

Table 2. Atomic coordinates (x 10^4) and equivalent isotropic displacement parameters (A^2 x 10^3) for 5-methyluridine. U(eq) is defined as one third of the trace of the orthogonalized Uij tensor.

	x	y	z	U(eq)
C1	11256(1)	3096(1)	9179(4)	32(1)
C2	10863(1)	1904(1)	11602(4)	34(1)
C3	10752(1)	3762(1)	10637(4)	33(1)
C4	11581(1)	4312(1)	11190(4)	29(1)
C5	11998(1)	1318(1)	14868(4)	36(1)
C6	12173(1)	4217(1)	8601(4)	31(1)
C7	12671(1)	1916(1)	14207(4)	32(1)
C8	13209(2)	4438(1)	8783(5)	42(1)
C9	12406(1)	2456(1)	12385(4)	32(1)
C10	13627(2)	1926(1)	15594(5)	45(1)
N1	11534(1)	2464(1)	11089(3)	32(1)
N2	11134(1)	1361(1)	13502(4)	38(1)
O2	12092(1)	3401(1)	7964(3)	36(1)
O3	10083(1)	1901(1)	10490(3)	49(1)
O4	10098(1)	4070(1)	8730(4)	48(1)
O5	11258(1)	5074(1)	11631(3)	44(1)
O6	12129(1)	791(1)	16528(4)	57(1)
O7	13685(1)	4102(1)	11081(3)	43(1)
O1W	10000	0	5576(5)	43(1)

Table 3. Bond lengths [A], angles and torsions [deg] for 5-methyluridine.

C1-O2	1.416(2)	N1-C1-C3	112.83(15)
C1-N1	1.489(2)	O3-C2-N2	122.96(16)
C1-C3	1.528(3)	O3-C2-N1	122.48(18)
C2-O3	1.221(2)	N2-C2-N1	114.54(16)
C2-N2	1.373(2)	O4-C3-C1	106.39(16)
C2-N1	1.375(2)	O4-C3-C4	112.06(16)
C3-O4	1.409(2)	C1-C3-C4	101.49(14)
C3-C4	1.528(2)	O5-C4-C6	113.78(16)
C4-O5	1.412(2)	O5-C4-C3	111.42(14)
C4-C6	1.518(3)	C6-C4-C3	101.74(16)
C5-O6	1.233(2)	O6-C5-N2	118.93(18)
C5-N2	1.385(2)	O6-C5-C7	125.59(19)
C5-C7	1.437(3)	N2-C5-C7	115.48(16)

C6-O2	1.451(2)	O2-C6-C8	109.60(15)
C6-C8	1.507(3)	O2-C6-C4	103.86(14)
C7-C9	1.341(3)	C8-C6-C4	116.91(18)
C7-C10	1.502(3)	C9-C7-C5	117.88(17)
C8-O7	1.426(3)	C9-C7-C10	122.44(17)
C9-N1	1.377(2)	C5-C7-C10	119.67(17)
O2-C1-N1	108.50(14)	O7-C8-C6	113.27(18)
O2-C1-C3	107.23(14)	C7-C9-N1	123.81(16)
C2-N1-C9	121.28(15)	C2-N1-C1	116.89(14)
C9-N1-C1	121.77(14)	C2-N2-C5	127.00(16)
C1-O2-C6	109.84(13)		

Table 4. Anisotropic displacement parameters (A^2 x 10^3) for 5-methyluridine.
The anisotropic displacement factor exponent takes the form:
-2 pi^2 [h^2 a*^2 U11 + ... + 2 h k a* b* U12]

	U11	U22	U33	U23	U13	U12
C1	33(1)	27(1)	36(1)	-1(1)	-5(1)	-2(1)
C2	30(1)	25(1)	47(1)	-4(1)	-2(1)	1(1)
C3	26(1)	33(1)	41(1)	-3(1)	-1(1)	2(1)
C4	27(1)	28(1)	32(1)	-3(1)	0(1)	4(1)
C5	36(1)	30(1)	42(1)	2(1)	0(1)	5(1)
C6	38(1)	25(1)	31(1)	1(1)	2(1)	1(1)
C7	29(1)	28(1)	39(1)	-3(1)	-3(1)	3(1)
C8	39(1)	41(1)	46(1)	1(1)	12(1)	-3(1)
C9	26(1)	29(1)	40(1)	-2(1)	-2(1)	-3(1)
C10	36(1)	46(1)	52(1)	3(1)	-10(1)	1(1)
N1	30(1)	24(1)	41(1)	1(1)	-5(1)	-1(1)
N2	32(1)	28(1)	53(1)	5(1)	0(1)	-3(1)
O2	43(1)	29(1)	36(1)	-5(1)	8(1)	2(1)
O3	35(1)	40(1)	72(1)	6(1)	-15(1)	-7(1)
O4	38(1)	40(1)	67(1)	-8(1)	-22(1)	10(1)
O5	36(1)	32(1)	63(1)	-17(1)	-4(1)	6(1)
O6	52(1)	46(1)	72(1)	27(1)	-10(1)	-2(1)
O7	32(1)	44(1)	54(1)	-6(1)	2(1)	7(1)
O1W	32(1)	47(1)	50(1)	0	0	2(1)

Table 5. Hydrogen coordinates (x 10^4) and isotropic
displacement parameters (A^2 x 10^3) for 5-methyluridine.

	x	y	z	U(eq)
H3	10426(14)	3601(11)	12340(50)	36(5)
H4	11969(13)	4107(10)	12780(40)	24(4)
H6	11867(15)	4515(11)	7060(50)	38(6)
H8A	13512(17)	4326(13)	7020(60)	49(7)

H8B	13219(14)	5032(14)	8990(40)	51(6)
H9	12789(13)	2868(10)	11820(40)	27(5)
H10A	14018(18)	1469(14)	14980(60)	73(8)
H10B	13976(19)	2388(15)	15140(70)	77(8)
H10C	13540(20)	1877(15)	17570(70)	70(8)
H1	10845(15)	2861(12)	7750(50)	45(6)
H2N	10687(18)	983(14)	13810(60)	67(8)
H4O	9647(19)	4393(14)	9740(60)	74(9)
H5O	11722(17)	5340(13)	12220(50)	52(7)
H7O	14070(20)	3766(16)	10480(60)	77(9)
H1W	9563(16)	203(13)	6590(50)	58(8)

A.III Studies of Reliability of Chemical Shift Tensors Fitting

Recently, Hodgkinson and Emsley [120] investigated the reliability of the determination of CSA parameters by calculating variance bounds. In this section, the determination of CSA parameters has been investigated in three aspects:

- reliability of determination of tensor parameters using different fitting programs
- comparison of static and MAS
- comparison of CSA amplification and MAS

A series of carbon-13 CP/MAS spectra of singly labeled glycine-1-^{13}C recorded at different MAS rates. Also two carbon-13 CSA amplification spectra were recorded with an amplification factor 8 and MAS rates of 8 and 10 kHz, resulting in an effective MAS rate in the ω_1 dimension of 1 kHz and 1.25 kHz. Three different simulation methods (SIMPSON, DMFIT and matNMR) were used to study the anisotropic chemical shift. The good agreement shown in Table A.2 indicates that all simulation methods function correctly.

Table A.2 Comparison anisotropy (ζ) and asymmetry (η) for glycine-1-^{13}C

	SIMPSON	
	ζ(ppm)	η
CP-1kHz	-67.4	1
CP-1.25kHz	-68.0	1
CP-1.5kHz	-68.7	1
CP-2kHz	-68.5	1
static	-68.5	1
CSA amplification-8kHz	-66.5	1
CSA-amplification-10kHz	-68.3	1
Average	-68.0	1
	DMFIT	
	ζ(ppm)	η
CP-1kHz	-68.7	1
CP-1.25kHz	-67.9	1
CP-1.5kHz	-67.6	1
CP-2kHz	-69.0	0.95
static	-68.8	1
CSA amplification-8kHz	-67.6	1
CSA-amplification-10kHz	-67.9	1
Average	-68.2	0.99
	matNMR	
	ζ(ppm)	η
CP-1kHz	-67.3	1
CP-1.25kHz	-67.8	1
CP-1.5kHz	-68.2	1
CP-2kHz	-68.1	1
static	-69.0	1
CSA amplification-8kHz	-66.6	1
CSA-amplification-10kHz	-68.1	1
Average	-67.9	1
Ref. [121]	71.0	

References

[1] A. Pines, M. G. Gibby and J. S. Waugh, Proton-Enhanced NMR of Dilute Spins in Solids, **1973**, *59*, 569-590.

[2] S. R. Hartmann and E. L. Hahn, Nuclear Double Resonance in Rotating Frame, **1962**, *128*, 2042-2053.

[3] A. Schuhl, S. Maegawa, M. W. Meisel and M. Chapellier, Production of Enhanced Liquid-He-4 Magnetization by Dynamic Nuclear-Polarization, *Phys. Rev. Lett.* **1985**, *54*, 1952-1955.

[4] T. R. Carver and C. P. Slichter, Experimental Verification of the Overhauser Nuclear Polarization Effect, *Phys. Rev.* **1956**, *102*, 975-980.

[5] C. P. Slichter, Concept of Temperature and the Overhauser Nuclear Polarization Effect, *Phys. Rev.* **1955**, *99*, 1822-1823.

[6] J. P. Wolfe and A. R. King, Optically-Pumped Proton Maser, *Chem. Phys. Lett.* **1976**, *40*, 451-455.

[7] J. P. Wolfe, Optical-Pumping by Excitation of Molecular Vibrations, *Chem. Phys. Lett.* **1976**, *37*, 256-259.

[8] J. Jeener, Ampere International Summer School, Basko Polje, Jugoslavia, *Unpublished* **1971**.

[9] T. Tanaka and M. Ikura, Structural-Analysis of Proteins by Multidimensional NMR, *J. Synth. Org. Chem. Jpn.* **1993**, *51*, 491-501.

[10] M. A. Bernstein, L. D. Hall and S. Sukumar, Assignment of Proton NMR-Spectra of Carbohydrates, Using Two-Dimensional Techniques - COSY and SECSY, *Carbohydr. Res.* **1982**, *103*, C1-C16.

[11] W. P. Aue, E. Bartholdi and R. R. Ernst, 2-Dimensional Spectroscopy Application to Nuclear Magnetic Resonance, *J. Chem. Phys.* **1976**, *64*, 2229-2246.

[12] R. Bruschweiler, B. Roux, M. Blackledge, C. Griesinger, M. Karplus and R. R. Ernst, Influence of Rapid Intramolecular Motion on NMR Cross-Relaxation Rates. A Molecular Dynamics Study of Antamanide in Solution, *J. Am. Chem. Soc.* **1992**, *114*, 2289-2302.

[13] Z. L. Madi, C. Griesinger and R. R. Ernst, Conformational Dynamics of Proline Residues in Antamanide. J Coupling Analysis of Strongly Coupled Spin Systems Based on E. COSY Spectra, *J. Am. Chem. Soc.* **1990**, *112*, 2908-2914.

[14] E. R. Andrew, A. Bradbury and R. G. Eades, Removal of Dipolar Broadening of Nuclear Magnetic Resonance Spectra of Solids by Specimen Rotation, *Nature* **1959**, *183*, 1802-1803.

[15] I. J. Lowe, Free Induction Decays of Rotating Solids, *Phys. Rev. Lett.* **1959**, *2*, 285-287.

[16] J. S. Waugh, L. M. Huber and U. Haeberle, Approach to High-Resolution NMR in Solids, *Phys. Rev. Lett.* **1968**, *20*, 180-182.

[17] B. C. Gerstein, R. G. Pembleton, R. C. Wilson and L. M. Ryan, High Resolution NMR in Randomly Oriented Solids with Homonuclear Dipolar Broadening: Combined Multiple Pulse NMR and Magic Angle Spinning, *J. Chem. Phys.* **1977**, *66*, 361-362.

[18] A. C. deDios and E. Oldfield, Recent Progress in Understanding Chemical Shifts, *Solid State Nucl. Magn. Reson.* **1996**, *6*, 101-125.

[19] J. Heller, D. D. Laws, M. Tomaselli, D. S. King, D. E. Wemmer, A. Pines, R. H. Havlin and E. Oldfield, Determination of Dihedral Angles in Peptides through Experimental and Theoretical Studies of alpha-Carbon Chemical Shielding Tensors, *J. Am. Chem. Soc.* **1997**, *119*, 7827-7831.

[20] C. J. Pickard and F. Mauri, All-electron Magnetic Response with Pseudopotentials: NMR Chemical Shifts, *Phys. Rev. B.* ARTN *245101* **2001**, *63*.

[21] M. M. Maricq and J. S. Waugh, NMR in Rotating Solids, *J. Chem. Phys.* **1979**, *70*, 3300-3316.

[22] J. Herzfeld and A. E. Berger, Sideband Intensities in NMR Spectra of Samples Spinning at the Magic Angle, *J. Chem. Phys.* **1980**, *73*, 6021-6030.

[23] A. Bax, N. M. Szeverenyi and G. E. Maciel, Chemical Shift Anisotropy in Powdered Solids Studied by 2D FT NMR with Flipping of the Spinning Axis, *J. Magn. Reson.* **1983**, *55*, 494-497.

[24] T. Terao, T. Fujii, T. Onodera and A. Saika, Switching-Angle Sample-Spinning NMR-Spectroscopy for Obtaining Powder-Pattern-Resolved 2D Spectra: Measurements of ^{13}C Chemical-Shift Anisotropies in Powdered 3,4-Dimethoxybenzaldehyde, *Chem. Phys. Lett.* **1984**, *107*, 145-148.

[25] G. E. Maciel, N. M. Szeverenyi and M. Sardashti, Chemical-Shift-Anisotropy Powder Patterns by the Two-Dimensional Angle-Flipping Approach. Effects of Crystallite Packing, *J. Magn. Reson.* **1985**, *64*, 365-374.

[26] T. Nakai and C. A. McDowell, A Fast Two-Dimensional Switching-Angle Sample-Spinning Method for Separating Chemical-Shift Powder Patterns, *J. Magn. Reson.* **1991**, *93*, 618-623.

[27] R. C. Zeigler, R. A. Wind and G. E. Maciel, The Stop-and-Go Spinning Technique in MAS Experiments, *J. Magn. Reson.* **1988**, *79*, 299-306.

[28] A. Bax, N. M. Szeverenyi and G. E. Maciel, Correlation of Isotropic Shifts and Chemical Shift Anisotropies by Two-Dimensional Fourier-Transform Magic-Angle Hopping NMR Spectroscopy, *J. Magn. Reson.* **1983**, *52*, 147-152.

[29] J. Z. Hu, A. M. Orendt, D. W. Alderman, C. H. Ye, R. J. Pugmire and D. M. Grant, Improvements to the Magic-Angle Hopping Experiment, *Solid State Nucl. Magn. Reson.* **1993**, *2*, 235-243.

[30] J. Z. Hu, W. Wang, F. Liu, M. S. Solum, D. W. Alderman, R. J. Pugmire and D. M. Grant, Magic-Angle-Turning Experiments for Measuring Chemical-Shift-Tensor Principal Values in Powdered Solids, *J. Magn. Reson. Ser. A* **1995**, *113*, 210-222.

[31] J. Z. Hu, D. W. Alderman, C. H. Ye, R. J. Pugmire and D. M. Grant, An Isotropic Chemical Shift-Chemical Shift Anisotropy Magic-Angle Slow-Spinning 2D NMR Experiment, *J. Magn. Reson. Ser. A* **1993**, *105*, 82-87.

[32] Z. H. Gan, High-Resolution Chemical-Shift and Chemical-Shift Anisotropy Correlation in Solids Using Slow Magic Angle Spinning, *J. Am. Chem. Soc.* **1992**, *114*, 8307-8309.

[33] L. Frydman, G. C. Chingas, Y. K. Lee, P. J. Grandinetti, M. A. Eastman, G. A. Barrall and A. Pines, Variable-Angle Correlation Spectroscopy in Solid-State Nuclear Magnetic Resonance, *J. Chem. Phys.* **1992**, *97*, 4800-4808.

[34] M. A. Alla, E. I. Kundla and E. T. Lippmaa, Selective Determination of Anisotropic Magnetic-Interactions from High-Resolution NMR-Spectra of Powdered Samples, *Jept. Lett.* **1978**, *27*, 194-197.

[35] Y. Yarimagaev, P. N. Tutunjian and J. S. Waugh, Sample Spinning at the Magic Angle with Rotation-Synchronized Rf Pulses, *J. Magn. Reson.* **1982**, *47*, 51-60.

[36] A. Bax, N. M. Szeverenyi and G. E. Maciel, Chemical-Shift Anisotropy in Powdered Solids Studied by 2D FT CP MAS NMR, *J. Magn. Reson.* **1983**, *51*, 400-408.

[37] R. Tycko, G. Dabbagh and P. A. Mirau, Determination of Chemical-Shift-Anisotropy Lineshapes in a Two-Dimensional Magic-Angle-Spinning NMR Experiment, *J. Magn. Reson.* **1989**, *85*, 265-274.

[38] S. F. Liu, J. D. Mao and K. Schmidt-Rohr, A Robust Technique for Two-Dimensional Separation of Undistorted Chemical Shift Anisotropy Powder Patterns in Magic-Angle-Spinning NMR, *J. Magn. Reson.* **2002**, *155*, 15-28.

[39] Z. H. Gan, D. M. Grant and R. R. Ernst, NMR Chemical Shift Anisotropy Measurements by RF Driven Rotary Resonance, *Chem. Phys. Lett.* **1996**, *254*, 349-357.

[40] J. D. Gross, P. R. Costa and R. G. Griffin, Tilted N-Fold Symmetric Radio Frequency Pulse Sequences: Applications to CSA and Heteronuclear Dipolar Recoupling in Homonuclear Dipolar Coupled Spin Networks, *J. Chem. Phys.* **1998**, *108*, 7286-7293.

[41] Y. Ishii and T. Terao, Manipulation of Nuclear Spin Hamiltonians by RF-Field Modulations and its Applications to Observation of Powder Patterns under Magic-Angle Spinning, *J. Chem. Phys.* **1998**, *109*, 1366-1374.

[42] W. P. Aue, D. J. Ruben and R. G. Griffin, Two-Dimensional Rotational Spin-Echo NMR in Solids - Resolution of Isotropic and Anisotropic Chemical Shifts, *J. Magn. Reson.* **1981**, *43*, 472-477.

[43] P. Blumler, J. Jansen and B. Blumich, 2-Dimensional One-Pulse Rotational Echo Spectra, *Solid State Nucl. Magn. Reson.* **1994**, *3*, 237-240.

[44] W. P. Aue, D. J. Ruben and R. G. Griffin, Uniform Chemical-Shift Scaling - Application to 2D Resolved NMR Spectra of Rotating Powdered Samples, *J. Chem. Phys.* **1984**, *80*, 1729-1738.

[45] A. C. Kolbert, H. J. M. Degroot and R. G. Griffin, Two-Dimensional Switched-Speed Spinning NMR, *J. Magn. Reson.* **1989**, *85*, 60-68.

[46] A. C. Kolbert and R. G. Griffin, Two-Dimensional Resolution of Isotropic and Anisotropic Chemical Shifts in Magic Angle Spinning NMR, *Chem. Phys. Lett.* **1990**, *166*, 87-91.

[47] W. T. Dixon, J. Schaefer, M. D. Sefcik, E. O. Stejskal and R. A. McKay, Total Suppression of Sidebands in CPMAS C-13 NMR, *J. Magn. Reson.* **1982**, *49*, 341-345.

[48] D. W. Alderman, G. McGeorge, J. Z. Hu, R. J. Pugmire and D. M. Grant, A Sensitive, High Resolution Magic Angle Turning Experiment for Measuring Chemical Shift Tensor Principal Values, *Mol. Phys.* **1998**, *95*, 1113-1126.

[49] W. T. Dixon, Spinning-Sideband-Free NMR Spectra, *J. Magn. Reson.* **1981**, *44*, 220-223.

[50] W. T. Dixon, Spinning-Sideband-Free and Spinning-Sideband-Only NMR Spectra in Spinning Samples, *J. Chem. Phys.* **1982**, *77*, 1800-1809.

[51] S. F. Delacroix, J. J. Titman, A. Hagemeyer and H. W. Spiess, Increased Resolution in MAS NMR Spectra by Two-Dimensional Separation of Sideband by Order, *J. Magn. Reson.* **1992**, *97*, 435-443.

[52] O. N. Antzutkin, S. C. Shekar and M. H. Levitt, 2-Dimensional Sideband Separation in Magic-Angle-Spinning NMR, *J. Magn. Reson. Ser. A* **1995**, *115*, 7-19.

[53] A. C. Kolbert, D. P. Raleigh, M. H. Levitt and R. G. Griffin, Two-Dimensional Spin-Echo Nuclear Magnetic Resonance in Rotating Solids, *J. Chem. Phys.* **1989**, *90*, 679-689.

[54] T. Gullion, Extended Chemical-Shift Modulation, *J. Magn. Reson.* **1989**, *85*, 614-619.

[55] M. Strohmeier and D. M. Grant, A New Sensitive Isotropic-Anisotropic Separation Experiment - SPEED MAS, *J. Magn. Reson.* **2004**, *168*, 296-306.

[56] B. Elena, S. Hediger and L. Emsley, Correlation of Fast and Slow Chemical Shift Spinning Sideband Patterns Under Fast Magic-Angle Spinning, *J. Magn. Reson.* **2003**, *160*, 40-46.

[57] C. Crockford, H. Geen and J. J. Titman, Two-Dimensional MAS-NMR Spectra Which Correlate Fast and Slow Magic Angle Spinning Sideband Patterns, *Chem. Phys. Lett.* **2001**, *344*, 367-373.

[58] L. M. Shao, C. Crockford, H. Geen, G. Grasso and J. J. Titman, Chemical Shift Anisotropy Amplification, *J. Magn. Reson.* **2004**, *167*, 75-86.

[59] L. M. Shao, C. Crockford and J. J. Titman, Chemical Shift Anisotropy Amplification with High Amplification Factor and Improved Sensitivity, *J. Magn. Reson.* **2006**, *178*, 155-161.

[60] C. Crockford, H. Geen and J. J. Titman, Measurement of Orientation Distributions using Chemical Shift Amplification, *Solid State Nucl. Magn. Reson.* **2002**, *22*, 298-310.

[61] L. Shao and J. J. Titman, CAESURA: Measurement of Slow Molecular Dynamics by Solid-State Nuclear Magnetic Resonance Chemical Shift Anisotropy Modulation Amplification, *J. Chem. Phys.* 064507 **2006**, *125*.

[62] R. M. Orr, M. J. Duer and S. E. Ashbrook, Correlating Fast and Slow Chemical Shift Spinning Sideband Patterns in Solid-State NMR, *J. Magn. Reson.* **2005**, *174*, 301-309.

[63] A. Detken, E. H. Hardy, M. Ernst and B. H. Meier, Simple and Efficient Decoupling in Magic-Angle Spinning Solid-State NMR: the XiX Scheme, *Chem. Phys. Lett.* **2002**, *356*, 298-304.

[64] F. J. Dyson, The Radiation Theories of Tomonaga, Schwinger, and Feynman, *Phys. Rev.* **1949**, *75*, 486-502.

[65] U. Haeberle, *In Advances in Magnetic Resonance* **1976**, J. S. Waugh, Ed.; Academic Press: New York.

[66] D. A. Varshalovich, A. N. Moskalev and V. K. Khersonskii, *Quantum Theory of Angular Momentum* **1988**.

[67] M. E. Rose, *Elementary Theory of Angular Momentum* **1967**.

[68] M. Mehring, *Principles of High Resolution NMR in Solids* **1983**, Springer, Berlin.

[69] O. N. Antzutkin, Z. Y. Song, X. L. Feng and M. H. Levitt, Suppression of Sidebands in Magic Angle Spinning Nuclear Magnetic Resonance: General Principles and Analytical Solutions, *J. Chem. Phys.* **1994**, *100*, 130-140.

[70] O. N. Antzutkin, Y. K. Lee and M. H. Levitt, C-13 and N-15 Chemical Shift Anisotropy of Ampicillin and Penicillin-V Studied by 2D-PASS and CP/MAS NMR, *J. Magn. Reson.* **1998**, *135*, 144-155.

[71] A. E. Bennett, C. M. Rienstra, M. Auger, K. V. Lakshmi and R. G. Griffin, Heteronuclear Decoupling in Rotating Solids, *J. Chem. Phys.* **1995**, *103*, 6951-6958.

[72] M. H. Leviti and R. Freeman, NMR Population-Inversion Using a Composite Pulse, *J. Magn. Reson.* **1979**, *33*, 473-476.

[73] N. Ivchenko, C. E. Hughes and M. H. Levitt, Application of Cogwheel Phase Cycling to Sideband Manipulation Experiments in Solid-State NMR, *J. Magn. Reson.* **2003**, *164*, 286-293.

[74] M. H. Levitt, P. K. Maduh and C. E. Hughes, Cogwheel Phase Cycling, *J. Magn. Reson.* **2002**, *155*, 300-306.

[75] G. Bodenhausen, R. Freeman, R. Niedermeyer and D. L. Turner, Double Fourier Transformation in High-Resolution NMR, *J. Magn. Reson.* **1977**, *26*, 133-164.

[76] L. S. Blackford, J. Demmel, J. Dongarra, I. Duff, S. Hammarling, G. Henry, M. Heroux, L. Kaufman, A. Lumsdaine, A. Petitet, R. Pozo, K. Remington and R. C. Whaley, *ACM Trans. Math. Soft.*, **2002**, *28*, 135.

[77] M. Eden and M. H. Levitt, Computation of Orientational Averages in Solid-State NMR by Gaussian Spherical Quadrature, *J. Magn. Reson.* **1998**, *132*, 220-239.

[78] M. Bak, J. T. Rasmussen and N. C. Nielsen, SIMPSON: A General Simulation Program for Solid-State NMR Spectroscopy, *J. Magn. Reson.* **2000**, *147*, 296-330.

[79] M. Bak and N. C. Nielsen, REPULSION, A Novel Approach to Efficient Powder Averaging in Solid-State NMR, *J. Magn. Reson.* **1997**, *125*, 132-139.

[80] F. James, MINUIT Minimisation Package: Reference Manual,, *CERN Program Library, Geneva*, **1994**.

[81] R. R. Ketchem, W. Hu and T. A. Cross, High-Resolution Conformation of Gramicidin A in a Lipid Bilayer by Solid-State NMR, *Science* **1993**, *261*, 1457-1460.

[82] S. J. Opella, Y. Kim and P Mcdonnell, Experimental Nuclear Magnetic Resonance Studies of Membrane Proteins, *Methods Enzymol.* **1994**, *239*, 536-560.

[83] D. R. Studelska, C. A. Klug, D. D. Beusen, L. M. McDowell and J. Schaefer, Long-Range Distance Measurements of Protein Binding Sites by Rotational-Echo Double Resonance NMR, *J. Am. Chem. Soc.* **1996**, *118*, 5476-5477.

[84] M. E. Merritt, A. M. Christensen, K. Kramer, T. Hopkins and J. Schaefer, Detection of Intercatechol Cross-Links in Insect Cuticle by Solidstate Carbon-13 and Nitrogen-15 NMR, *J. Am. Chem. Soc.* **1996**, *118*, 11278-11282.

[85] J. Wang, Y. S. Balazs and L. K. Thompson, Solid-state REDOR NMR Distance Measurements at the Ligand Site of a Bacterial Chemotaxis Membrane Receptor, *Biochemistry* **1997**, *36*, 1699-1703.

[86] J. R. Long, J. L. Dindot, H. Zebroski, S. Kiihne, R. H. Clark, A. A. Campbell, P. S. Stayton and G. P. Drobny, A Peptide that Inhibits Hydroxyapatite Growth is In an Extended Conformation On the Crystal Surface, *Proc. Natl Acad. Sci. USA* **1998**, *95*, 12083-12087.

[87] M. Lera and C. J. Hayes, An Olefin Cross-Metathesis Approach to Vinylphosphonate-linked Nucleic Acids, *Org. Lett.* **2001**, *3*, 2765-2768.

[88] J. D. van Beek, matNMR: A Flexible Toolbox for Processing, Analyzing and Visualizing Magnetic Resonance Data in Matlab((R)), *J. Magn. Reson.* **2007**, *187*, 19-26.

[89] J Ying, A. Grishaev, D. L. Bryce and A. Bax, Chemical Shift Tensors of Protonated Base Carbons in Helical RNA and DNA from NMR Relaxation and Liquid Crystal Measurements., *J. Am. Chem. Soc* **2006**, *128*, 11443-11454.

[90] D. Stueber and D. M. Grant, ^{13}C and ^{15}N Chemical Shift Tensors in Adenosine, Guanosine Dihydrate, 2'-Deoxythymidine, and Cytidine, *J. Am. Chem. Soc.* **2002**, *124*, 10539-10551.

[91] D. J. Hunt and E. Subramanian, The Crystal Structure of 5-Methyluridine, *Acta Crystallogr.* **1969**, *B25*, 2144-2152.

[92] W. T. Klooster, J. R. Ruble, B. M. Craven and P. K. McMullan, Structure and Thermal Vibrations of Adenosine From Neutron Diffraction Data at 123 K., *Acta Crystallogr., B* **1991**, *47*, 376-383.

[93] U. Thewalt, C. E. Bugg and R. E. Marsh, The Crystal Structure of Guanosine Dihydrate and Inosine Dihydrate, *Acta Crystallogr.* **1970**, *B26*, 1089-1101.

[94] S. Sato, T. Yoshida and T. Hori, Determination of Absolute Configurations of Light-Atom Molecules by Means of Direct Detection of Bijvoet Differences., *Enantiomer: J. Sterochemistry* **2002**, *7*, 271-281.

[95] M. Lutz, A. Spek and J. Raap, a-Thymidine at 105 K, *Private Communication* **2001**.

[96] E. A. Green, R. D. Rosenstein, R. Shiono, D. J. Abraham, B. L. Trus and R. E. Marsh, The Crystal Structure of Uridine, *Acta Crystallogr.* **1975**, *B31*, 102-107.

[97] S. J. Clark, M. D. Segall, C. J. Pickard, P. J. Hasnip, M. J. Probert, K. Refson and M. C. Payne, First Principles Methods Using CASTEP, *Z Kristallogr:* **2005,** *220,* 567-570.

[98] C. J. Pickard and F. Mauri, All-Electron Magnetic Response with Pseudopotentials: NMR Chemical Shifts, *Phys. Rev. B* 245101. **2001,** *63,* 1-13.

[99] D. Vanderbilt, Soft Self-Consistent Pseudopotentials In a Generalized Eigenvalue Formalism, *Phys. Rev. B* **1990,** *41,* 7892-7895.

[100] H. J. Monkhorst and J. D. pack, Special Points for Brillouin-Zone Integrations, *Phys. Rev. B* **1976,** *13,* 5188-5192.

[101] J. P. Perdew, K. Burke and M. Ernzerhof, Generalized Gradient Approximation Made Simple, *Phys. Rev. Lett.* **1996,** *77,* 3865-3868.

[102] D. Fletcher, R. McMeeking and D. parkin, The United Kingdom Cemical Database Service, *J. Chem. Inf. Comput. Sci.* **1996,** *36,* 746-749.

[103] C*ambridge Structural Database Refcode: ADENOS01.*

[104] C*ambridge Structural Database Refcode: THYDIN02.*

[105] C*ambridge Structural Database Refcode: BEURID10.*

[106] C*ambridge Structural Database Refcode: CYTIDI11.*

[107] C*ambridge Structural Database Refcode: GUANSH10.*

[108] C*ambridge Structural Database Refcode: MEURID.*

[109] Y. Sugawara, Y. Iimura, H. Iwasaki, H. Urabe and H. Saito, Reversible Crystal Transition of Guanosine between the Dihydrate and Anhydrous States Coupled

with Adsorption-Desorption Process, *J. Biomol. Struct. & Dynam.* **1994,** *11,* 721-729.

[110] V. Capriati, S. Florio, R. Luisi, B. Musio, I. Alkorta, F. Blanco and J. Elguero, A Computational Study of the Effect of C-lithiation on the NMR Properties (chemical shifts and coupling constants) of Aziridines *Struct. Chem.* **2008,** *19,* 785-792.

[111] I. Alkorta and J. Elguero, A GIAO/DFT study of ^{1}H, ^{13}C and ^{15}N Shieldings in Amines and its Relevance in Conformational Analysis, *Magn. Reson. Chem.* **2004,** *42,* 955-961.

[112] J. E. Del Bene, J. Elguero, M. Y. I. Alkorta and O. M. , An ab Initio Study of 15N-11B Spin-Spin Coupling Constants for Borazine and Selected Derivatives, *J. Phys. Chem. A* **2006,** *110,* 9959-9966.

[113] J. R. Yates, T. N. Pham, C. J. Pickard, F. Mauri, A. M. Amado, A. M. Gil and S. P. Brown, An Investigation of Weak CH···O Hydrogen Bonds in Maltose Anomers by a Combination of Calculation and Experimental Solid-State NMR Spectroscopy, *J. Am. Chem. Soc.* **2005,** *127,* 10216-10220.

[114] P. Ciuffreda, S. Casatii and A. Manzocchi, Complete ^{1}H and ^{13}C NMR Spectral Assignment of alpha- and beta-adenosine, 2'-deoxyadenosine and their Acetate Derivatives, *Magn. Reson. Chem.* **2007,** *45,* 781-784.

[115] A. Lesage, D. Sakellariou, S. Steuernagel and L. Emsley, Carbon-Proton Chemical Shift Correlation in Solid-State NMR by Through-Bond Multiple-Quantum Spectroscopy, *J. Am. Chem. Soc.* **1998,** *120,* 13194-13201.

[116] D. Sakellariou, A. Lesage, P. Hodgkinson and L. Emsley, Homonuclear Dipolar Decoupling in Solid-State NMR using Continuous Phase Modulation, *Chem. Phys. Lett.* **2000,** *319*, 253-260.

[117] H. O. Kalinowski, S. Berger and S. Braun, C*arbon-13 NMR Spectroscopy (J.Wiley & Sons, Chichester, 1988).*

[118] S. A. Kates and F. Albericio, Solid-Phase Synthesis. A Practical Guide, **2000,** *New York.*

[119] V. Bork, T. Gullion, A. Hing and J. Schaefer, Measurement of ^{13}C-^{15}N Coupling by Dipolar-Rotational Spin-Echo NMR, *J. Magn. Reson.* **1990,** *88*, 523-532.

[120] P. Hodgkinson and L. Emsley, The Reliability of the Determination of Tensor Parameters by Solid-State Nuclear Magnetic Resonance, *J. Chem. Phys.* **1997,** *107*, 4808-4816.

[121] C. H. Ye, R. Q. Fu, J. Z. Hu, L. Hou and S. W. Ding, C-13 Chemical-Shift Anisotropies of Solid Amino-Acids, *Magn. Reson. Chem.* **1993,** *31*, 699-704.